Study of conventional and advanced imaging techniques for mammography

By

REENA SHARMA

PHYS01201304010

Bhabha Atomic Research Centre, Mumbai

A thesis submitted to the

Board of Studies in Physical Sciences

In partial fulfillment of requirements

For the Degree of

DOCTOR OF PHILOSOPHY

Of

HOMI BHABHA NATIONAL INSTITUTE

December, 2018

Homi Bhabha National Institute

Recommendations of the Viva Voce Committee

As members of the Viva Voce Committee, we certify that we have read the dissertation prepared by Smt. Reena Sharma entitled "**Study of conventional and advanced imaging techniques for mammography**" and recommend that it may be accepted as fulfilling the thesis requirement for the award of Degree of Doctor of Philosophy.

Chairman: Prof. Amar Sinha	Amar Sinha	Date: 10th April 2019
Guide / Convener: Prof. S. D. Sharma	S D Sharma	Date: 10th April 2019
External Examiner: Prof. S. P. Mishra	S P Mishra	Date: 10th April 2019
Member 1: Prof. D. D. Deshpande		Date: 10th April 2019
Member 3: Prof. B. K. Sapra	B K Sapra	Date: 10th April 2019
Member 3: Prof. B. N. Pandey	B. N. Pandey	Date: 10th April 2019

Final approval and acceptance of this thesis is contingent upon the candidate's submission of the final copies of the thesis to HBNI.

I/We hereby certify that I/we have read this thesis prepared under my/our direction and recommend that it may be accepted as fulfilling the thesis requirement.

S D Sharma 10/4/19

Date: 10th April 2019
Place: Mumbai

Dr. S. D. Sharma
Guide/Convener

STATEMENT BY AUTHOR

This dissertation has been submitted in partial fulfillment of requirements for an advanced degree at Homi Bhabha National Institute (HBNI) and is deposited in the Library to be made available to borrowers under rules of the HBNI.

Brief quotations from this dissertation are allowable without special permission, provided that accurate acknowledgement of source is made. Requests for permission for extended quotation from or reproduction of this manuscript in whole or in part may be granted by the Competent Authority of HBNI when in his or her judgment the proposed use of the material is in the interests of scholarship. In all other instances, however, permission must be obtained from the author.

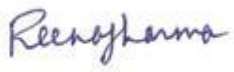

(Smt. Reena Sharma)

DECLARATION

I, hereby declare that the investigation presented in the thesis has been carried out by me. The work is original and has not been submitted earlier as a whole or in part for a degree / diploma at this or any other Institution / University.

(Smt. Reena Sharma)

==========

List of journal publications arising from the thesis

==========

1. Sharma R, Sharma SD, Sarkar PS, Singh B, Agrawal AK and Datta D **2019** Phantom based feasibility studies on phase-contrast mammography at Indian synchrotron facility Indus-2 *J. Med. Phys.* 44 39 – 48.
2. Sharma R, Sharma SD, Sarkar PS and Datta D **2018** Imaging and dosemetric study on direct flat panel detector based digital mammography system *J. Med. Phys.* **43** 255-263.
3. Sharma R, Sharma SD, Mayya YS and Chaurasiya G **2012** Mammography dosimetry using an in-house developed PMMA phantom *Radiat. Prot. Dosim*. **151** 379 - 385.
4. Sharma R, Sharma SD and Mayya YS **2012** Light sensitometry of mammography films at varying development temperatures and times *J. Med. Phys.* **37** 40 - 45.
5. Sharma R, Sharma SD and Mayya YS **2012** A survey on performance status of mammography machines: image quality and dosimetry studies using a standard mammography imaging phantom *Radiat. Prot. Dosim*. **150** 325 - 333.

==========

List of conference publications arising from the thesis

==========

1. Sharma R, Jambhale S, Sharma SD and Datta D **2017** Mammography imaging study using synchrotron radiation *J. Med. Phys.* **42** S69 - S70.
2. Sharma R, Sharma SD, Sarkar PS, Sinha A and Babu DAR **2014** Phase contrast x-ray imaging using a mammography phantom *J. Med. Phys.* **39** 308-309.

3. Sharma R, Sharma SD, Pawar S, Babu DAR and Chaubey A **2014** Dose measurements in CR mammography using different breast simulating phantoms *J. Med. Phys.* **39** 367-368.

==========

List of publications of the candidate from other than thesis work

==========

1. Sharma R, Sharma SD, Pawar S. Chaubey A, Kantharia S and Babu DAR **2015** Radiation dose to patients from X-ray radiographic examinations using computed radiography imaging system *J. Med. Phys*. **40** 29-37.
2. Sharma SD, Sharma R, Mulchandani U, Chaubey A, Chourasia G and Mayya YS **2012** Measurement of entrance skin dose for diagnostic x-ray radiographic examinations and establishment of local diagnostic reference levels *Proc. IFMBE* **39** 860-863.
3. Sharma R, Pawar S, Sharma SD, Tripathi SM, Chourasia G and Babu DAR **2014** Film and Personnel Safety Evaluation of X-ray Baggage Scanners Abstract book 31st IARP National Conference on "Advances in Radiation Measurement Systems and Techniques" (IARPNC-2014) March 19-21, BARC, Mumbai.
4. Sharma R, Sharma SD, Pawar S and Babu DAR **2015** Testing of radiation shielding materials used in diagnostic X-ray departments, Abstract book of International Conference on Medical Physics, Radiation Protection and Radiobiology (ICMPRPR 2k15), February 20-22, SMS Medical College, Jaipur.

(Smt. Reena Sharma)

DEDICATED TO

MY FAMILY,

(Especially my elder brother Shri M B Bohra)

RESPECTED TEACHERS &

ALMIGHTY

ACKNOWLEDGEMENTS

I express my deepest sense of gratitude to my guide and mentor, Dr. S. D. Sharma, RP&AD, BARC for his valuable guidance, scientific expertise, constant encouragement and motivation. I am greatly indebted to my doctoral committee chairman Prof. Amar Sinha, DAE-RRF, BARC who has guided me to finish the work related to x-ray phase contrast imaging using synchrotron facility of RRCAT, Indore. I convey my heartfelt gratitude to Dr. P.S Sarkar, TPD, BARC for constantly sharing his technical expertise in medical x-ray imaging. I would take this opportunity to thank the respected members of my doctoral committee, Prof. D.D Deshpande (member), Prof. B.K. Sapra (member), and Prof. B.N. Pandey (member) for their critical and valuable scientific suggestions during the annual progress reviews and pre-synopsis presentation. I would like to express my sincere gratitude to Dr. Y. S. Mayya, Former Head, RP&AD, for his scientific help, inspiration and encouragement during my thesis work. Also i want to express my sincere thanks to Dr. D. A. R. Babu, Ex-Head, RP&AD for providing his guidance in the course of this research work. I would like to thank Dr. D. Datta, Head RP&AD and Prof. B. K. Nayak (Dean Academic, PMS) for the valuable suggestions and motivations. It gives me a great pleasure to acknowledge my colleague Smt. Philomina A and Smt. Shramika J. for their continuous support and motivation. Also it gives me immense pleasure to acknowledge my collaborators from RRCAT, Indore, Dr. Ashish K. Agrawal and Shri Balwant Singh, Officers in charge of imaging beam line (BL- 4) for providing their all kind of support administrative as well as technical for finishing my thesis work related to use of synchrotron.

I thank all those who have helped in providing scientific and administrative support during various stages of executing the work reported in this thesis. I am thankful to my family,

friends for their unconditional love and support. Most importantly, I owe a lot to my elder brother Shri M B Bohra who always encouraged and helped me at every stage of my life. I would like to express my endless thanks and appreciation to my husband Dr. Manoj K Sharma for his kind support in this journey. Finally, I want to thank Almighty for blessing me Aayushi, my adorable daughter who has completed my life with her beautiful and priceless smile.

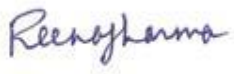

(Smt. Reena Sharma)

CONTENTS

SYNOPSIS

Mammography is one of the leading imaging modality for detecting breast cancer among women. Over the past two decades, the Asia-Pacific region has experienced a rapid rise in the annual incidence and mortality from breast cancer than the western countries. Rise in breast cancer incidences has introduced many new technologies based mammography systems into the country including refurbished and phased out machines imported from the developed countries like USA, UK and Japan. However, the imaging and dosimetric studies on such systems are neither conducted by the supplier nor by the user which is a gap area required to be attended. Hence, it is essential to study the imaging capabilities of both conventional and advanced mammography systems. In addition, it is also important to estimate the radiation dose delivered during mammography procedures and optimize the technique so that the radiation risk can be minimized without affecting the image quality. Thus, the main objectives of the thesis work were: (i) to evaluate the sensitometric characteristics of commonly used mammography film with varying temperature and time and optimize the processing conditions, (ii) thoroughly analyze the image quality of digital mammography systems and establish the relation between image quality and mean glandular dose simulating the clinical situations, and (iii) to conduct a detailed study on the upcoming phase contrast imaging modality using synchrotron radiation source and compare its performance with absorption contrast imaging modalities. The additional objective of the thesis work was to develop a mammography imaging and dosimetry phantom as import substitute and demonstrate its suitability in the quality assurance (QA)/quality control (QC) of mammography systems.

A variety of image receptors are used in mammography with the progressive advent of imaging technologies. In the early days, mammography was performed with non-screen, direct exposure film which has produced low contrast images at higher radiation dose to patients. Also, it is reported that mammography screening examinations in the 1950s and 1960s, did not provide any useful benefits in the early detection of breast cancer because of the poor image quality. In the 1970s and 1980s, mammography using Xeroradiographic process became very popular as it was capable of producing breast images of good spatial resolution and edge-enhancement. However, this technique was also producing images with relatively poor contrast sensitivity coupled with higher radiation dose in comparison to the technologically advanced screen-film mammography (SFM) system which led to the demise of the Xeroxmammography in the late 1980s. Continuous developments in imaging technology have vastly improved mammography over last 35 years starting form screen-film to digital images.

Digital mammography technology offers simplified archival, retrieval and transmission of images, reduction in mean glandular dose (MGD), higher patient workflow and improved diagnostic accuracy (Skaane 2010, Tabar 2012). Computed radiography (CR) and direct radiography (DR) have many similarities as both technologies produce digital images within seconds of exposure that can be enhanced for soft copy diagnosis or further review. CR generally involves the use of a cassette that houses the imaging plate, similar to traditional film-screen systems, to record the image whereas DR typically captures the image directly onto a flat panel detector without the use of a cassette. Digital detectors with lower spatial resolution than film also appear to improve lesion conspicuity through their improved efficiency of absorption of x-ray photons, a linear response over a wide range of radiation

intensities and low system noise (Tabar 2012). In addition, post-processing software can be utilized to assist the radiologist in evaluating the images for suspicious findings by altering contrast and brightness automatically or manually. Also in digital mammography system, the images can be displayed in hard and softcopy formats.

Although conventional mammography systems, which are based on absorption imaging, can produce good contrast for the samples having high subject contrast. But the same is not true when the absorption imaging is used for the samples having low subject contrast which is the case of soft tissues found within the breast. Hence, the concept of phase based imaging was brought forth. In this method of imaging, changes in phase of x-rays passing through the samples are measured when spatially coherent sources (e.g. microfocus and synchrotron radiation) are used. The phase change process of the x-ray beam passing through the samples can be described using a complex index of refraction, n=1- δ- iß, where ß describes the absorption of x rays and δ is associated with the phase-shift due to refractive effects.

At typical mammography x-ray energies, the phase-shift term can be up to1000 times greater than the absorption term which is of the order of 10^{-7}, compared to 10^{-10} (Fitzgerald 2000). Thus, it may be possible to observe phase contrast when absorption contrast is undetectable. Different relative phases are produced when x-rays pass through regions of differing δ. These phase differences are detected by the various x-ray phase contrast techniques. In recent years, use of synchrotron radiation (SR) is increasing globally in the medical imaging due to the advent of x-ray phase contrast imaging (XPCI) technology (Fitousi et al 2012, Bradley et al 2007, Munro et al 2010). XPCI has shown the great potential with respect to improved visibility contrast while examining the soft tissues of the breast (Miao et al

2005). XPCI can be realized by three methods namely, propagation, interference and analyzer based and present study employs the propagation method for producing phase contrast. Under XPCI technique, an air gap between the object and the detector is established to transform the phase gradients generated by the interference of x-rays having different phase shifts into intensity gradient on the image (Dreossi et al 2008, Matsuo et al 2005, Weon et al 2006). However, various types of detectors employed in mammography require specific amount of radiation for good quality images to be produced. Hence, proper evaluation of mammography equipment is necessary to maintain a balance between image quality and patient dose. ***Therefore, this thesis aims at evaluating the various image quality and dosimetry parameters responsible for reducing the radiation risk to patients when examined with low energy x-ray based conventional and advanced mammography imaging system.***

Under this thesis work, mammography film commonly used in India has been evaluated for its sensitometric characteristics (Hurter and Driefield (H&D) curve) at different processing temperature and time. As sensitometric characteristics of the film affects the image quality and patient doses in SFM. To evaluate the actual clinical patient doses, it is highly recommended that phantoms made up of breast tissue equivalent material are to be used (Craig et al 2001, ACR 1999, NCS 6 1993). Hence, a polymethyl methacrylate (PMMA) phantom was developed and characterized for its use in mammography system. In India, screen-film mammography is gradually being replaced by digital mammography systems mainly in urban areas of the country due to its several advantages over SFM. It was required to conduct a systematic study on digital mammography system to evaluate its performance from the image quality and dosimetry point of view. Also in this thesis work in-phantom imaging studies were carried out at Indian synchrotron facility RRCAT, Indore to compare

the x-ray phase contrast and absorption contrast to explore the feasibility of using synchrotron radiation in mammography. The thesis comprises six chapters including introductory details and summary of the work.

Chapter 1 provides details about various breast imaging modalities including mammography for breast cancer detection. Among all imaging modalities, technical features of the mammography system with its component are discussed in detail. Breast anatomy and physiology is explained as this is required for accurate diagnosis and selection of effective mode of treatment for breast disease including cancer. Types of breast cancers are explained considering their origin within the various breast tissues. Review on breast cancer incidences in India is discussed in some detail. Historical development of mammography system is summarized keeping focus on various image receptors e.g. screen-film, computed radiography (CR) and flat panel based digital detectors. Imaging methodologies applied in x-ray absorption and phase imaging is given in this chapter. Also types of x-ray interaction with matter are explained in some detail as these interactions are responsible for producing a mammogram and the radiation dose to patients in mammography. Additionally, various image quality parameters used in mammography have been provided in this chapter. Finally, quantities and units applied in mammography dosimetry are explained.

Chapter 2 describes the detailed study performed on a Kodak MinR-2000 mammography film to evaluate its sensitometric parameters and their influence on image quality and patient doses. This film was selected based on its vast use in most of the mammography centers located in Mumbai area (Sharma et al 2012). The sensitometric parameters like base plus fog level (B+F), maximum optical density (OD_{max}), average gradient (AG) and speed of the film at varying development temperature and time were

evaluated using a calibrated light sensitometer (X-Rite, Michigan, USA). Total 33 film strips were cut from a single Kodak MinR-2000 mammography film box, and exposed using a light sensitometer operated in the green light spectrum to produce 21-step sensitometric strips. These exposed film strips were processed at 32 to 37^0 C in the step of 1^0 C temperature and processing time was also varied from1 to 6 minutes in the step of 1 minute. This study shows that the measured base plus fog level of the mammography film was not affected appreciably whereas significant changes were seen in the OD_{max}, AG and speed with varying development temperature and time. The OD_{max} values of the studied film were found in the range of 3.67 - 3.76, AG in the range of 2.48 - 3.4 and speed in the range of 0.015 - 0.0236 when processing temperature was varied from 32 to 37^0C. With processing time variation from 1 to 6 minutes, the observed changes in OD_{max} values were in the range of 3.54 - 3.71, AG in the range of 2.66 - 3.27 and speed in the range of 0.011 - 0.025. Recommendations were provided for optimum processing conditions to be used for the studied mammography film on the basis of our work. Similar studies for various types of mammography films will be helpful in deciding the onset processing conditions to be used by the automatic film processors.

Chapter 3 deals with the development of a mammography imaging and dosimetry phantom as import substitute to demonstrate its suitability in the quality assurance (QA)/quality control (QC) of mammography systems. Phantom based measurements in mammography are well established for QA and QC procedures involving equipment performance and comparisons of x-ray machines of different models. Polymethyl methacrylate (PMMA) is among the best suitable materials for simulation of the breast (Dance et al 1999, Thilander-Klang1997). Hence for carrying out QA/QC exercises in various mammography centers of India, a mammographic PMMA phantom with engraved slots for

keeping thermoluminiscence dosimeters (TLD) has been developed. The radiation transmission property of this phantom was compared with commercially available similar phantoms for verifying its suitability for mammography dosimetry. The breast entrance exposure (BEE), mean glandular dose (MGD), percentage depth dose (PDD), percentage surface dose distribution (PSDD), calibration testing of automatic exposure control (AEC) and density control function of a mammography machine were measured using this phantom. MGD was derived from the measured BEE following two different methodologies and the results were compared. The PDD and PSDD measurements were carried out using LiF: Mg, Cu, P chips. The difference in the MGD values derived using two different methods were found in the range of 17.5 to 32.6%. Measured depth ranges in the phantom lies between 0.32-0.40 cm for 75% depth dose, 0.73-0.92cm for 50% depth dose and1.54-1.78 cm for 25% depth dose. Higher PSDD value was observed towards chest wall edge side of the phantom which is due to the orientation of cathode-anode axis along chest wall to nipple direction. Results obtained for AEC configuration testing shows that the observed mean optical density (OD) of the phantom image was 1.59 and O.D difference for every successive increase in thickness of the phantom was within ±0.15 O.D. Under density control function testing, at -2 and -1 density settings, the variation in O.D was within ±0.15 O.D of the normal density setting '0'. And at +2 and +1 density setting the measured O.D was within ±0.30.The in-house developed phantom was found comparable with the commercially available phantoms and the outcome of the study indicates that the locally made PMMA TLD slot phantom can be used to measure various QC parameter of different mammography systems.

Chapter 4 provides details of imaging and dosemetric studies carried out for a direct flat panel detector based digital mammography system. Image quality characterization of any

x-ray based imaging system is evaluated by measuring three primary physical parameters: contrast, resolution and noise (Andrew and Srinivasan 2012). Various imaging metrics such as CNR, contrast detail resolution, MTF and NPS were evaluated following the European guidelines. Also, system performance relating to both image quality and doses were evaluated using figure of merit (FOM) in terms of CNR^2/MGD under automatic exposure control (AEC) and clinically used OPDOSE operating mode. Under AEC mode, FOM values for the 4.5 cm thick BARC PMMA phantom were found to be 15.02, 15.88 and 19.82 at Mo/Mo, Mo/Rh and W/Rh target/filter (T/F) of respectively. Under OPDOSE mode, FOM values were found to 65.32, 11.80 and 1.14 for the BARC PMMA phantom thickness of 2, 4.5 and 8 cm respectively. Under OPDOSE mode, the calculated MGD values for three CIRS slab phantoms having total thickness of 7.0 cm were observed to be 3.03, 2.32 and 1.75 mGy with glandular/adipose tissue compositions of 70/30, 50/50 and 30/70 respectively. Whereas for 2 to 8 cm thick BARC PMMA phantom, calculated MGDs were found to be in the range of 0.57 to 3.32 mGy. Detailed dosemetric studies were also performed on the digital mammography system by evaluating mean glandular doses (MGDs) using several mammography phantoms made up of breast tissue equivalent materials. All the calculated MGDs values were found to be lower than the acceptable level of dose limits provided in European guidelines.

Chapter 5 contains details about the feasibility studies of using synchrotron radiation in mammography imaging. The use of synchrotron radiation in medical imaging has shown great potential for improving soft tissue image contrast especially in case of breast. Advanced imaging technique using SR have been explored by carrying out x-ray phase contrast imaging studies in mammography at Indian synchrotron facility Indus-2. Under this study quantitative

evaluation of XPCI technique for the various breast tissue equivalent test materials and mammography phantoms are reported. Different phantoms and samples including locally fabricated samples were used to perform absorption and phase mode imaging at 12 and 16 keV SR beams. Edge enhancement index (EEI) and edge enhancement to noise ratio (EE/N) were measured for all the phantom and sample images. Absorbed dose values to air were calculated for 12 and 16 keV SR beams using the measured SR flux at the object plane and by applying the standard radiation dosimetry formalism. For the first time in India, XPCI studies were carried out in mammography using low energy synchrotron beams of 12 and 16 keV. Outcome of the study suggests good contrast improvement under phase mode than the absorption mode for the various test objects and phantoms giving future scope for imaging the breast tissue specimens.

Chapter 6 presents summary and important conclusions of the thesis work. It also includes the future scope in the area of study. Followings are the summary of the work conducted:

- Sensitometric evaluation of a Kodak Min R-2000 mammography film with varying processing temperature and time for the optimization of image quality and doses in SFM.
- Fabrication and testing of a PMMA mammography phantom for dosimetry and image quality studies which has been developed as import substitute for quality assurance/quality control in mammography.
- Detailed image analysis and quantification of contrast, spatial resolution and noise of the direct flat panel detector based digital mammography system. CNR, MTF, NPS and FOM were evaluated following the European guidelines.

- Dosimetry of digital mammography system using different tissue equivalent phantoms to establish the relation between image quality and mean glandular dose simulating the clinical operation conditions of the machine.
- Study related to feasibility of using SR in mammography where various test objects and phantoms were employed to analyze the x-ray phase contrast over absorption contrast.

References

American College of Radiology (ACR) *Mammography quality control manual-Mammography* (Reston, VA: American College of Radiology)

Andrew K and Srinivasan V 2012 Detectors for digital mammography *(Digital Mammography: A Practical Approach)* (New York: Cambridge University Press)

Bradley D, Gundogdu O, Jenneson P, Eleftheria N and Ismail E H C 2007 Review of x-ray phase contrast imaging techniques and propagation based imaging using a benchtop microfocal source *Jurnal Sains Kesihatan Malaysia* **5** 1-16

Craig A R, Heggie J C P, McLean I D, Coakley K S and Nicoll J J 2001 Recommendations for a mammography quality assurance programme ACPSEM position paper *Australas. Phys. Eng. Sci. Med.* **24** 107-130

Dance D R, Skinner C L and Carlsson G A 1999 Breast Dosimetry *Appl. Radiat. Isot*. **50** 185-203

Dreossi D, Abrami A, Arfelli F, Bregant P, Casarin K, Chenda V, Cova M A, Longo R, Menk R H, Quai E, Quaia E, Rigon L, Rokvik T, Sanabor D, Tonutti M, Tromba G, Vascotto A, Zanconato E and Castelli E 2008 The mammography project at the SYRMEP beamline *Eur. J. Radiol.* **68S** S58-S62

Fitousi N T, Delis H and Panayiotakis G 2012 Monte Carlo simulation of breast imaging using synchrotron radiation *Med. Phys.* **39** 2069

Fitzgerald R 2000 Phase-sensitive x-ray imaging *Phys. Today* 5323–26

Matsuo S, Katafuchi T, Tohyama K, Morishita J, Yamada K and Fujita H 2005 Evaluation of edge effect due to phase contrast imaging for mammography Med. *Phys.* **32** 2690-97

Miao H, Gomella AA, Harmon K J, Bennett EE, Chedid N, Znati S, Panna A, Foster B A, Bhandarkar P and Wen H 2015 Enhancing tabletop x-ray phase contrast imaging with nanofabrication *Sci. Rep.* **5** 13581

Munro P R T, Konstantin I, Robert D S and Alessandro O 2010 Design of a novel phase contrast x-ray imaging system for mammography *Phys. Med. Biol.* **55** 4169-85

NCS 6 1993 Netherlands commission on radiation dosimetry task group mammography *Dosemetric aspects of mammography* (The Netherlands)

Sharma R, Sharma S D and Mayya Y S 2012 A survey on performance status of mammography machines: image quality and dosimetry studies using a standard mammography imaging phantom *Radiat. Prot. Dosim.* **150** 325-333.

Skaane P 2010 *Digital Mammography* (Berlin: Springer) pp 155-173

Tabar L 2012 *Imaging of the breast: Technical aspects and clinical implication* (available at http://www.intechopen.com)

Thilander-Klang A 1997 Diagnostic quality and absorbed doses in mammography: Influence of X-ray spectra and breast anatomy *PhD Thesis* University of Goteborg

Weon B M, Je J H, Hwu Y and Margaritondo G 2006 Phase contrast x-ray imaging *Int. J. Nanotechnology* **3** 280-297.

LIST OF FIGURES

LIST OF TABLES

Chapter 1

Introduction

1.1 Motivation

Mammography imaging technique uses low energy x-rays for diagnosis and screening of female breast for the early detection of cancer and other breast diseases. In India, breast cancer has ranked topmost cancer among females with age adjusted rate as high as 25.8 per 100,000 women and mortality 12.7 per 100,000 women (Shreshtha et al 2017). Rise in breast cancer incidences has introduced many new technologies based mammography systems into the country including refurbished and phased out machines imported from the developed countries like USA, UK and Japan. However, the imaging and dosimetric studies on such systems are neither conducted by the supplier nor by the user which is a gap area required to be attended. Hence, it is essential to study the imaging capabilities of both conventional and advanced mammography systems. In addition, it is also important to estimate the radiation dose delivered during mammography procedures and optimize the technique so that the radiation risk can be minimized without affecting the image quality. In India, use of mammography systems are found to be increasing due to increasing trend seen in the incidences of breast cancers among female in past few years. At present about 2200 mammography machines are registered with Atomic Energy Regulatory Board (AERB), India. Out of these machines about 30 % are of screen-film mammography and rest are digital technology based. Considering the use of both SFM and digital mammography systems in the country, systematic image quality and dosimetry studies are carried out on SFM and digital mammography machine in the thesis work. Also knowing the importance of phantom based imaging and dosimetry under QC and QA programme for mammography systems, a PMMA based mammography phantom was developed as import substitute. As most of the conventional mammography systems are based on absorption imaging which can produce

good contrast for the samples having high subject contrast. But the same is not true when the absorption imaging is used for the samples having low subject contrast which is the case of soft tissues found within the breast. Considering this fact, the concept of x-ray phase based imaging was brought forth in the thesis by performing feasibility studies in mammography using synchrotron at Indian synchrotron facility RRCAT, Indore.

1.2 Overview of breast anatomy and physiology

The accurate diagnosis and effective mode of treatment for any breast disease including cancer requires a clear understanding of breast anatomy and physiology. Breast undergoes through many changes than any other part of the human body from birth, puberty, pregnancy and breastfeeding, right through to menopause. The fully developed female breast is a well-differentiated apocrine sweat gland originating in the ectoderm that secretes milk during lactation and is of the same type found in the axilla and elsewhere in the body. Anatomically, the adult breast sits atop the pectoralis muscle which is atop the ribcage. The epithelial component of the tissue consists of lobules, where milk is made, which connect to ducts that lead out to the nipple. Most cancers of the breast arise within the cells which form the lobules and terminal ducts. These lobules and ducts are spread throughout the background fibrous tissue and adipose tissues that makes up the majority of the breast. The breast tissue extends horizontally (side-to-side) from the edge of the sternum (the firm flat bone in the middle of the chest) out to the midaxillary line (the center of the axilla, or underarm) (Johns Hopkins University 2018). A tail of breast tissue called the "axillary tail of Spence" extends into the underarm area and a breast cancer can develop in this axillary tail, even though it might not seem to be located within the actual breast. Anatomic dissection of breast show that the glandular tissue consists of 15-20 glands called lobes or segments containing ducts that

branch and subdivided into smaller ducts as they extend into the deeper glandular tissue. The end units of the smallest ducts are composed of milk-forming lobules that drain radially through the ducts toward the nipple. The two breast lie anterior to the right and left pectoral muscles, extending from the sternum laterally to the mid axillary line. The breast and armpit contain lymph nodes and vessels carrying lymph fluid and white blood cells as shown in figure 1.1 (NBCF 2018). The breast tissue is encircled by a thin layer of connective tissue called fascia. The deep layer of this fascia sits immediately atop the pectoralis muscle, and the superficial layer sits just under the skin. The skin covering the breast is similar to skin elsewhere on the body and has similar sweat glands, hair follicles, and other features. A clinician examines the skin in addition to the breast tissue itself when performing a breast.

The blood supply to the breast comes primarily from the internal mammary artery, which runs underneath the main breast tissue. The blood supply provides nutrients, such as oxygen, to the breast tissue (Johns Hopkins University 2018). The lymphatic vessels of the breast flow in the opposite direction of the blood supply and drain into lymph nodes. It is through these lymphatic vessels that breast cancers metastasize or spread to lymph nodes. Most lymphatic vessels flow to the axillary (underarm) lymph nodes, while a smaller number of lymphatic vessels flow to internal mammary lymph nodes located deep to the breast. The proper knowledge of lymphatic drainage is important, because when a breast cancer metastasizes, it usually involves the first lymph node in the chain of lymph nodes. This is called the "sentinel lymph node," and a surgeon may remove this lymph node to check for metastases in a patient with breast cancer. Many additional changes are seen in the breast tissue during pregnancy and lactation due to the changes in hormones during those times. In the adult woman, the breast is made up of glandular tissue, connective tissue, and adipose

tissue that determine the size, shape and texture of the organ. At the apex of the breast is the mammary areola, a pigmented skin area whose surface is characterized by the presence of modified sebaceous glands that, with their secretion, have the function of making the nipple soft and elastic (Cirolla V 2017). Estrogen and progesterone induce changes in the glandular tissue depending on the period of the menstrual cycle, with sometimes painful swelling and nodular formations reaching the maximum size towards the end of the menstrual cycle and then regressing again. Thus it is important to examine the breast in the 7-10 days following the onset of menstruation as it is only during this time interval that breasts are easily examined and tumours can be easily differentiated from physiological nodularity.

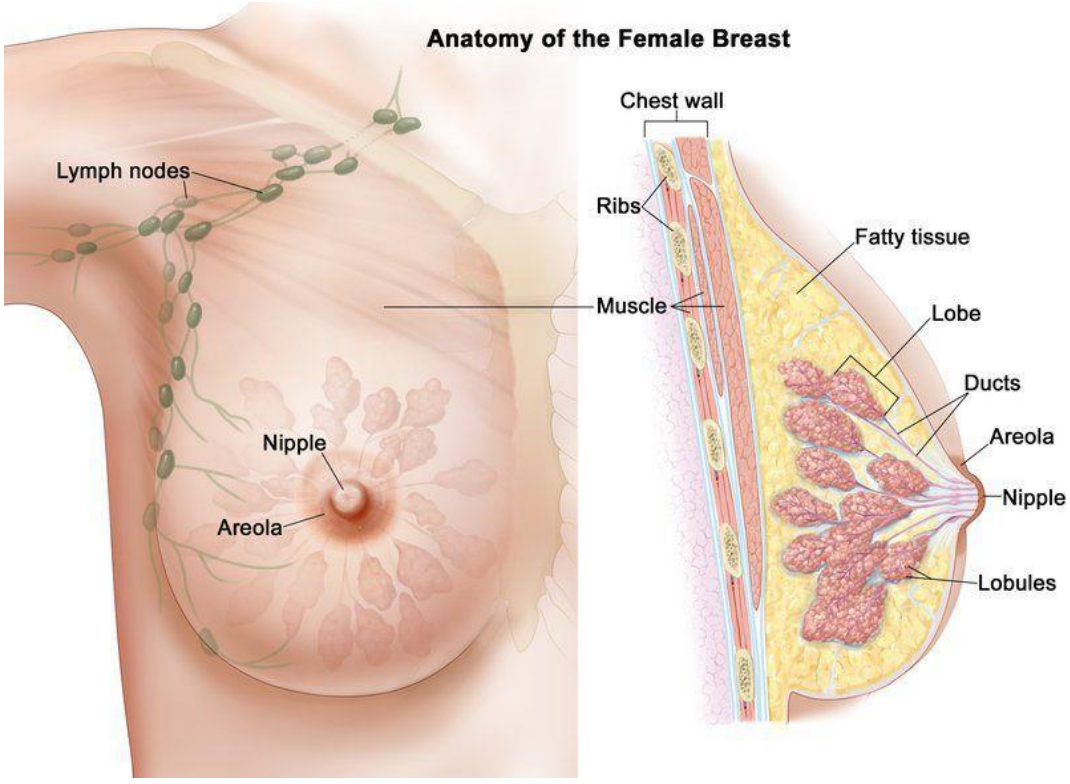

Figure 1.1 Schematic of female breast anatomy showing the lymph nodes, nipple, areola, chest wall, ribs, muscle, fatty tissue, lobe, ducts, and lobules [Taken from nbcf.org.au]

The lactating breast will have acini formed at the end of ducts during pregnancy for secretion of milk which will regress after lactation. The postmenopausal breast will have increased adipose tissue and decreased fibro glandular tissue. Most tumors develop at the terminal end of lobular units of the breast parenchyma. Glandular tissue is more abundant in the super-external portion of the breast; therefore about half of the tumors affect this area of the gland. Although hormones cause the glandular tissue to become denser, a woman's genetic predisposition and her ratio of total body adipose tissue to total body weight also influence her ratio of glandular tissue to adipose tissue in her breast. For this reason, some young women have breasts consisting primarily of adipose tissue, while some elderly women have breasts with exceedingly dense glandular tissue (NCRP 149 2004).

Breast cancer arises in the glandular tissue and the distribution of breast cancer is approximately proportional to the amount of glandular tissue. Hence in mammography emphasis is given to image the glandular tissue with as much as contrast and detail as possible with in the limitations of acceptable low radiation exposure. Distribution of glandular tissues within the breast can be divided into four quadrants as shown in figure 1.2. Glandular tissue can extend throughout the entire breast; only a thin layer of retromammary adipose tissue separates it from the pectoral muscle. The upper outer quadrant, which extends towards the axilla, is the thickest portion of the glandular tissue. Nearly half of the breasts' total glandular tissue is found in the upper outer quadrant and 45 percent of all breast cancers develop in the same upper outer quadrant (NCRP 149 2004).

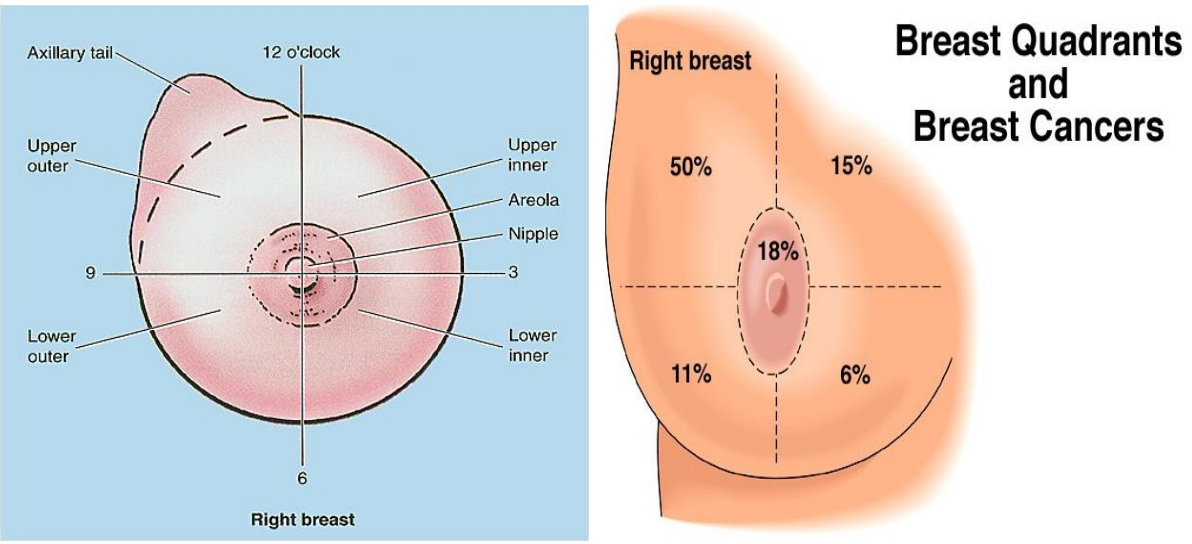

Figure 1.2 Anatomy of breast with four quadrants [Taken from https://people.ohio.edu and https://community.breastcancer.org]

1.2.1 Breast cancer types

Ninety percent of breast cancers are adenocarcinomas, which arise from glandular tissue (NIH 2018). Within this broad category, there is a great degree of variation. The earliest form of the disease, ductal carcinoma in situ, comprises about 15-20% of all breast cancers and develops solely in the milk ducts. The most common type of breast cancer, invasive ductal carcinoma, develops from ductal carcinoma in situ, spreads through the duct walls, and invades the breast tissue. Cancer that begins in the lobes or lobules is called lobular (small cell) carcinoma and is more likely to be found in both breasts. Invasive lobular carcinoma originates in the milk glands and accounts for 10-15% of invasive breast cancers. Both ductal and lobular carcinomas can be either in situ, or self-contained; or infiltrating, meaning penetrating the wall of the duct or lobe and spreading to adjacent tissue.

1.2.2 Breast cancer incidences in India

Literature review of published data and several reports on breast cancer incidences have suggested that there is a significant increase in breast cancer incidence rate in India and

breast cancer is the most common cause of death among woman in developed and developing countries (Ferlay et al 2015, Ferlay et al 2008, NCRP 2016). National Cancer Registry Programme (NCRP) which was commenced by the Indian Council of Medical Research (ICMR) with a network of Population Based Cancer Registries (PBCR) and Hospital Based Cancer Registries (HBCR) across the country shows that there is a significant increase in breast cancer incidence when compared with previously published data (NCRP 2016). Also data from these registries indicate that prevalence of breast cancer in different parts of the country is highest when compared with other cancer. Over the past two decades, the Asia-Pacific region, including India, has experienced a more rapid rise in the annual incidence and mortality from breast cancer than the western countries, such as the US & Canada and the countries of the European Union (Green et al 2008, Parkin et al 2005, Porter 2008). The incidence of breast cancer rises after age 40. The highest incidence (approximately 80% of invasive cases) occurs in women over age 50. In India, the age of the women when highest incidence of breast cancer can be seen is > 45 year (Masakazu et al 2010).

1.3 Breast imaging modalities

Early detection of breast cancer is considered to be the key factor for reducing mortality among women. As an early detection of breast cancer, primarily used technique is breast self examination (BSE) which allows a female to examine her breasts physically for any physical or visual changes. Under this particular examination both the breasts are examined in lying and standing positions to feel for any breast lumps. It is recommended that BSE to be performed one week after menstruation and any lumps felt should be further examined clinically by a doctor. Similar kind of physical examination known as clinical breast examination (CBE) is carried out by a trained physician to evaluate the breasts for

evidence of palpable or visible changes due to breast diseases. CBE is an important component of the routine physical examination in medical practice as a screening tool for detection of breast cancer. CBE in conjunction with mammography has detected more breast cancers than either of them used alone. Other than physical examination there are different imaging techniques which allow early detection of cancer and localization of the suspicious lesion in the breast for the further course of treatment.

1.3.1 Ultrasound

Ultrasound (US) imaging provides the further assessment of both palpable and impalpable breast abnormalities adjunct to mammography and clinical breast examination. It is also performed to diagnose breast lumps or other abnormalities found during a clinical physical exam or breast MRI History of first use of US in breast structure imaging goes back to 1951 (Wild 1950). In breast ultrasound imaging sound waves of frequency range 2 to 15 MHz are used to produce images of the internal structures of the breast. It is primarily used for patients with dense breasts and breast implants. Ultrasound is the imaging method of choice for the majority of women aged below 40 years as it is noninvasive and does not use radiation. Over 40 years of age ultrasound is used as an adjunct to mammography when there are focal clinical or mammographic signs. Focal abnormalities identified on ultrasound are assessed for signs that favour malignancy (irregular shape, ill-defined margin, solid hypoechogenicity, posterior acoustic shadowing, tissue distortion) and for signs that favour benignity (smooth shape, well defined margin, hyperechogenicity, posterior acoustic enhancement (Youe et al 2015, Alan et al 2016).

1.3.2 Magnetic resonance imaging (MRI)

Magnetic resonance imaging (MRI) is a generally accepted diagnostic procedure for a number of breast related indications because of its higher sensitivity towards tumors (Smith et al 2004). MRI creates images of the breast by measuring changes in the movement of protons in fat and water with the application of changing magnetic fields. By utilizing the differences in tissue relaxation characteristics, an image is acquired by processing the signal changes that occur following application of pulses of energy. Breast MRI for the detection of breast cancer requires administration of the contrast agent gadolinium. The use of MRI for breast cancer detection is based on the concept of tumor angiogenesis or neovascularity. Tumor-associated blood vessels have increased permeability, which leads to prompt uptake and release of gadolinium within the first one to two minutes after administration, leading to a pattern of rapid enhancement and washout on MRI Breast. MRI is often used in women who already have been diagnosed with breast cancer, to help measure the size of the cancer, look for other tumors in the breast, and to check for tumors in the opposite breast (Shahid et al 2016, DeMartini et al 2008). Although MRI can find some cancers not seen on a mammogram, it's also more likely to find something that turns out not to be cancer (called a false positive). False-positive findings have to be checked out to know that cancer isn't present as this can results in more tests or biopsies. This is why MRI is not recommended as a screening test for women at average risk of breast cancer because it would result in unneeded biopsies and other tests for many of these women.

1.3.3 Radioisotope imaging

This particular imaging technique is also known as emission imaging or nuclear medicine imaging. Under this imaging two radiotracers have been used widely to depict

breast cancer: the γ-emitting 99mTc-sestamibi (99mTc-methoxyisobutylisonitrile), 140 keV, half-life of 6 hour, originally developed as a myocardial per-fusion agent; and the positron-emitting glucose analog 18F-FDG (Fluoro deoxyglucose), 511keV, half-life of 2 hour (Berg et al 2016). Nuclear medicine involving radiopharmaceuticals has been actively used for the detection of breast cancer. Currently, there are three radiotracers commonly used for breast imaging or scintimammography in either clinical practice or research: 99mTc-sestamibi and 99mTc-tetrofosmin (two agents used for myocardial perfusion imaging) and 99mTc-MDP (methylene diphosphonate, used for bone scintigraphy) (Taillefer 1999). Scintimammography is a relatively new, non-invasive diagnostic modality in the evaluation of breast cancer (Liberman et al 2003). Positron emission tomography (PET) with millimeter resolution can image the earliest in situ forms of breast cancer as well as putative cancer precursor lesions (e.g., atypical ductal hyperplasia) whose behavior is important for prevention studies (Weinberg 2006).

1.3.4 Thermography

In breast thermography which is also known as infrared imaging, a pictorial representation of the infrared energy or heat emission of the breasts is recorded. It is based on the observation that patients have an elevated breast skin temperature over breast cancer. Thermography/thermal imaging uses a special camera to measure the temperature of the skin on the breast's surface (Lahiri et al 2012, Ng and Kee 2008). It is non-invasive test that involves no radiation and is based on the fact that cancer cells are growing and multiplying very fast causing higher blood flow and metabolism in a cancer tumor as the blood flow and metabolism increases, skin temperature goes up which is then recorded as image in this technique Thermography has been available for several decades, but there is no evidence to

show that it's a good screening tool to detect breast cancer early, when the cancer is most treatable (Kennedy et al 2009, Macro et al 2017). Some women want thermography because it is painless and doesn't require exposure to radiation.

1.3.5 Optical imaging

Optical imaging (OI) refers to a variety of techniques using near infrared (NIR) light (700–1000 nm) and visible light (400–700 nm) to provide molecular, morphologic, and functional information, probing absorption, scattering, and fluorescence properties of cells or tissues. One of the most promising applications is to the breast, a superficial organ where the remodeled vasculature and changes in cellular and extracellular tissue structure caused by malignant lesions creates a contrast suitable for OI (Grosenick et al 2016, Di Leo et al 2017). The first attempts to use visible light to diagnose breast cancer were in the first half of the 20th century using a method called "transillumination" or "diaphonography" and resulted in the sensitivity as low as approximately 58% (Di Leo et al 2017).

1.3.6 Mammography imaging

Mammography remains the primary imaging tool for breast cancer despite the fact that there are supplemental modalities that appear to perform significantly better (Gotzsche et al 2000). It can identify small foci of cancer within the breast which otherwise cannot be diagnosed. Use of mammography technique has resulted in a 30% reduction in the mortality of breast cancer in women over 50 years of age (Sickles 2000, Khalkhali et al 1994). Following section provides the detail description of this mammography imaging technique.

1.4 Historical background of mammography

The use of x-rays in breast cancer can be traced back to 1913 when Salomon fist time used it for examining the spread of tumour giving base to the present imaging technology

called mammography (Collins et al 2015). Initially, breast imaging was done using film and then later screen-film combination. Concept of breast compression was introduced in 1951 and the dedicated mammography x-ray unit was used in 1965. Acceptance of the screen-film based mammography as a screening tool of breast cancer came in the year of 1970s (Collins et al 2015). Since then screen-film mammography was used extensively on a large female population detecting and diagnosing of breast cancer at its earliest stage globally. Screen-film based mammography has several limitations one is due to inherent characteristics shown by mammography film. Digital radiography detector systems were first implemented for medical applications in the mid 1980s, but the promise of digital imaging was not realized until the early 1990s, in conjunction with the establishment of first generation picture archiving and communication systems (PACS) (Lanca and Silva 2009, Siebert 2009). Digital mammography has additional advantages over conventional screen film mammography due to wider dynamic range, improved contrast between dense and non-dense breast tissue, faster image acquisition and easier image storage (Berns et al 2002, Huda et al 2003).

1.4.1 Mammography x-ray equipment

Mammography utilizes low energy x-rays for examining the female breast primarily with the aim of distinguishing the existence of tumours, cysts, calcifications, or any other abnormalities. Mammography equipment is specifically designed to demonstrate low subject contrast and fine detail of the breast tissues which are having small x-ray tissue attenuation differences. Due to involvement of radiation risks of ionizing radiation, optimization of techniques to achieve good image quality with minimum doses is very important in mammography. Hence continuous developments in mammography imaging techniques are going on. Mammography x-ray equipment comprise a high voltage generator, a tube with a

very small focus, a filter, a collimator, a compression system, the plate holder with the film or digital detector and an automatic exposure control (AEC) system as shown in figure 1.3 (Hendrick and Ikeda 2018). The mammographic unit consists of two basic components, an x-ray tube and an image receptor which are mounted on opposite sides of a mechanical assembly (Figure 1.3).

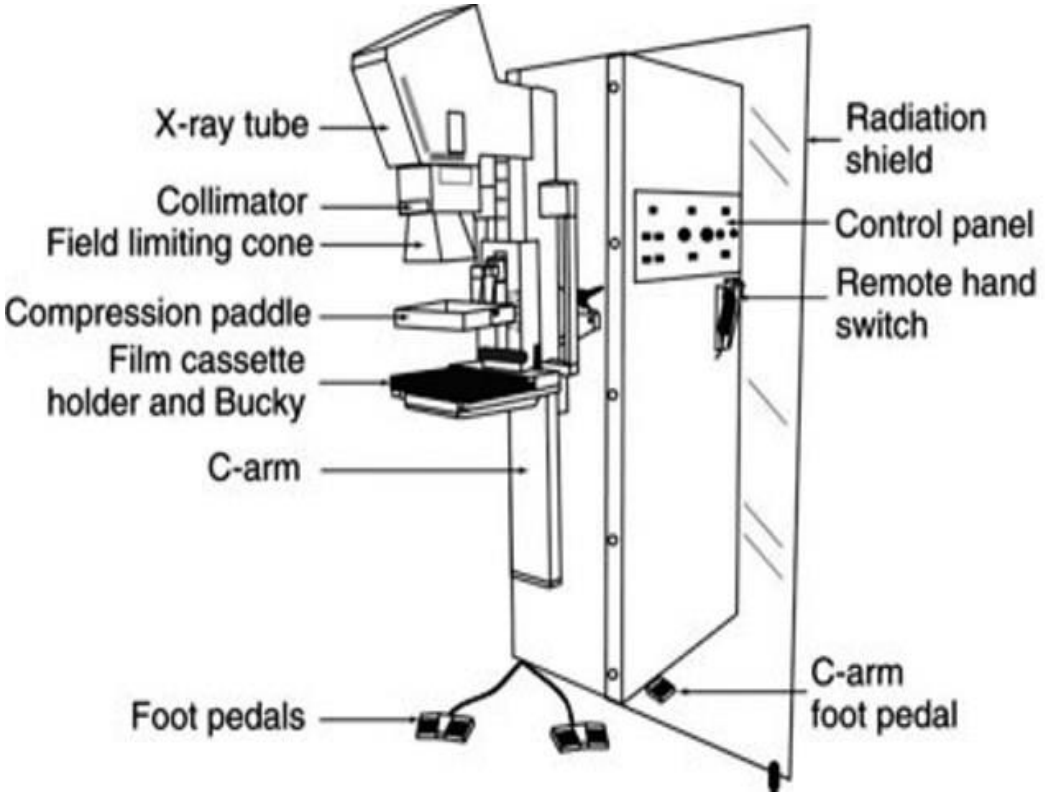

Figure 1.3 Components of an x-ray mammography unit [Taken from www.clinicalgate.com]

The mechanical assembly can be adjusted vertically and can rotate about a horizontal axis to accommodate patients of different height and due to the fact that the breast must be imaged from different aspects. X-ray photons generated from the x-ray tube assembly tube passes through a metallic spectral-shaping filter, a beam-defining aperture and the compression plate to reach upto the breast. Depending upon type of interaction these x-ray photons go through with breast tissues, the differentially attenuated x-ray intensity will be

recorded to form an image after passing through the antiscatter grid which is positioned between breast supporting system and image detector. In the following section brief description of mammography x-ray equipment in conjunction with mammographic image quality is given.

1.4.2 X-ray tube and generator

In mammography x-ray tubes, x-rays are produced when heated filament (cathode) due to thermionic emission emits electrons and these electrons are bombarded on the metal target (anode) inside a vacuum tube. The x-rays are emitted from the target over a spectrum of energies ranging up to the peak kilovoltage (kV_p) applied to the x-ray tube (typically 40 kV_p). A rotating anode design is used for modern mammographic x-ray tubes. To provide sufficient kinetic energy to the emitted electrons form the cathode, kilovolatge is applied using x-ray generators. The high-frequency generators offer more precise control of kilovolt (peak) (kVp), milliamperes (mA), and exposure time. The linearity and reproducibility of the radiographic exposures using high-frequency generators is uniformly excellent. High frequency generators are capable of generating efficient waveform output that produces a higher effective energy x-ray beam per set kVp and mA. High-frequency generators are compact in sizes and can be installed within the single-standing mammography unit operating on single-phase incoming line power, facilitating easy installation and creating a less intimidating appearance. In mammography x-ray tube, targets are used made up of molybdenum (Mo), rhodium (Rh) and tungsten (W) and spectral characteristics of produced x-rays are decided by the use of different target/filter (T/F) combinations. The anode has a beveled edge, which is at a steep angle to the direction of the electron beam. In mammography small focal spots ranging from 0.3 to 0.4 mm (contact imaging) and from 0.1

to 0.15 mm (magnification imaging) are used due to high spatial resolution and optimal image quality requirement. Window material used in mammography tube is beryllium (Be) which has low atomic number and high young modulus. Collimation of the x-ray beam is achieved using metal diaphragm collimators to provide predetermined field sizes matched to the image receptor's sizes (i.e. 18 x 24 cm^2 or 24 x 30 cm^2).

1.4.3 Mammography AEC system

Mammographic automatic exposure control (AEC) system is used to provide consistent signal values as breast thickness is varied over the range of x-ray tube potentials (NCRP 149 2004). In AEC system, a sensor in the form of an ionization chamber or solid state detector is located behind the image receptor. The sensor produces the current proportional to the exposure rate of the incident on it and the current charges a capacitor (Figure 1.4). The voltage across the capacitor is then proportional to the exposure to the sensor (and therefore to the patient). This voltage is compared to a reference voltage, and when the two voltages are equal, the exposure is terminated. Present day AEC appropriately compensates for variation in the selected operating potential and breast density and thickness. Compensation for operating potential can be accomplished by including the preset kilovolt peak as factor in the microprocessor controlled program of the AEC. This allows the variation of the AEC sensor sensitivity with operating potential to be taken into account in determining when the exposure should be terminated (Kimme-Smith et al 1992). Both the quality of the mammography image and the dose efficiency are critically dependent on the x-ray spectrum and shape of the it is determined by the anode material, applied potential to the tube, and the amount and type of added metallic filtration in the beam. Optimization of exposure can consider various statistics from a short test pulse made prior to the actual image acquisition.

These might include the minimum signal from the most attenuating region of the breast. The algorithm can require that in the actual exposure, this signal has to be greater than some preset value. Determination of the optimum x-ray spectrum for mammography involves a careful compromise between image contrast, radiation dose, and image statistical noise. Figure 1.4 gives the schematic for electronic circuit of mammography AEC system.

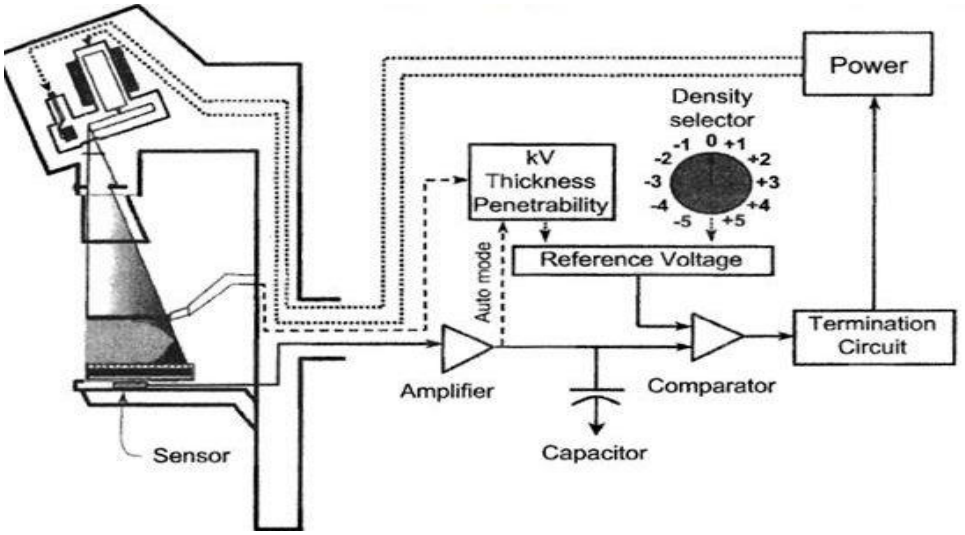

Figure 1.4 Schematic for electronic circuit of mammography AEC system [Taken from Bushberg et al 2002]

1.4.4 Compression device

The compression to the breast is achieved with a compression paddle, a flat plate attached to a mechanical compression device. Breast compression is required in mammography as it lowers down the patient dose by reducing the overall breast thickness. Reducing thickness produces lesser scatter components and hence improves the image quality parameter called contrast (Figure 1.5). It is essential that the compression plate allows the breast to be compressed parallel to the image receptor and that the edge of the plate at the chest wall be straight and aligned with both the focal spot and image receptor to maximize the amount of breast tissue being included in the image. Compression causes the different tissues

to be spread out, minimizing superposition from different planes and thereby improving conspicuity of structures. The use of compression decreases geometric blurring, the dose to the breast and the ratio of scattered to directly transmitted radiation that reaches the image receptor.

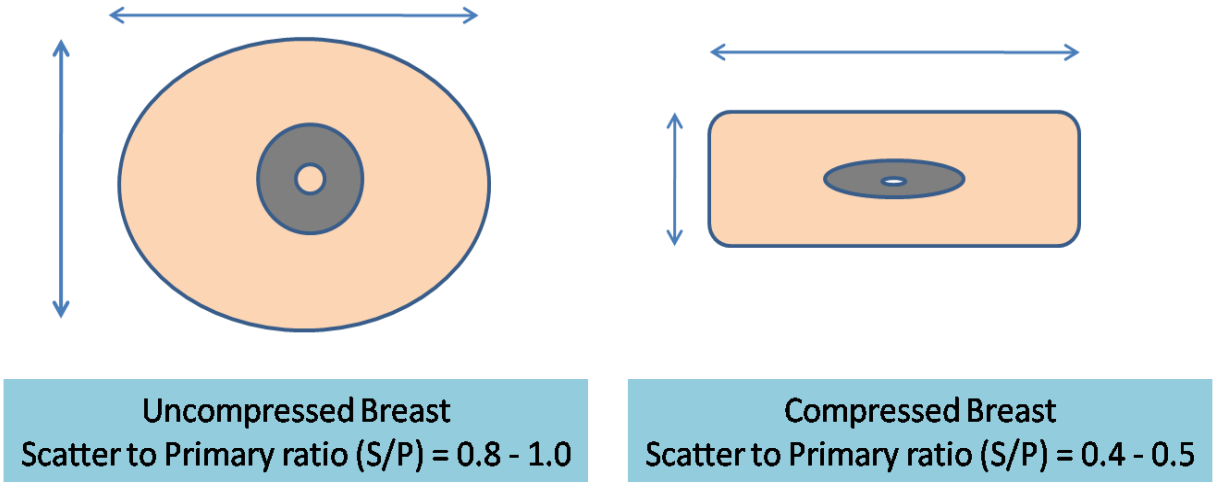

Figure 1.5 Schematic showing reductions in scatter to primary ratio for the noncompressed and compressed breast

1.4.5 Antiscatter grid

Specialized grids were developed for mammography during the 1980s to reduce scatter radiation and increase the image contrast in mammography. Scattered radiation comprises a considerable fraction of the radiation incident on the image receptor. In radiology, $C_s = C_0 [1 / (1+SPR)] = C_0 K$, where C_s is the subject contrast, C_o is the contrast in the absence of scattered radiation, SPR is the Scatter-to-Primary x-ray Ratio at the location of interest in the image and K is known as contrast reduction factor (Bushberg et al 2002). Figure 1.6 presents the geometrical characteristics of an antiscatter grid. The fraction of scattered radiation in the image can be reduced by the use of antiscatter grids or air gaps.

Scatter rejection is best accomplished with an antiscatter grid for contact film/screen breast imaging. Antiscatter grids are composed of linear lead (Pb) septa separated by a rigid interspace material. Generally, the grid septa are not strictly parallel but are focused toward the x-ray source. Due to the fact that the primary x-rays all travel along direct lines from the x-ray source to the image receptor while the scatter diverges from points within the breast, the grid presents a smaller acceptance aperture to scattered radiation than to primary and therefore discriminates against scattered radiation.

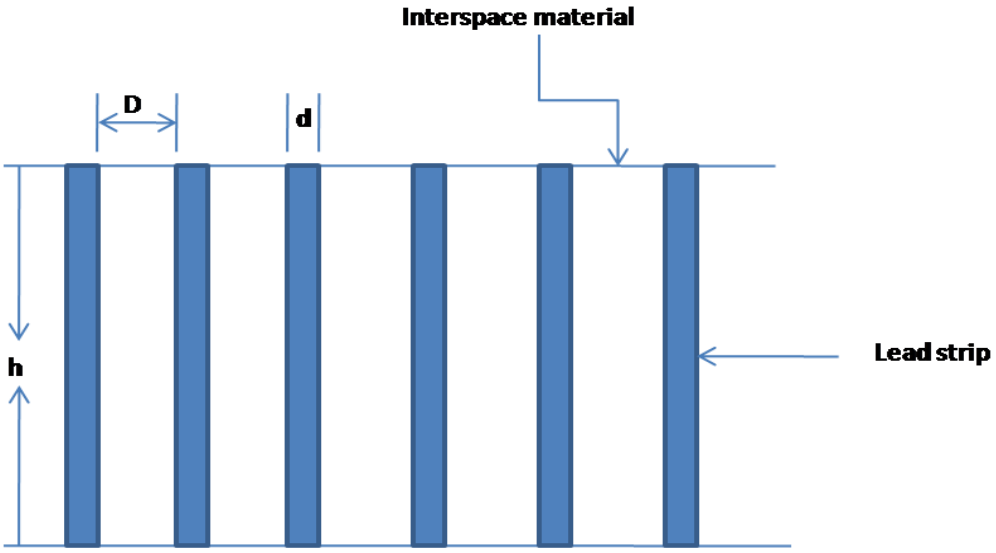

Figure 1.6 Schematic for the geometrical characteristics of an antiscatter grid: h the height of lead strips, d the thickness of lead strips, D the thickness of interspace material, 1/(D +d) the frequency and h/D is the grid ratio

Grids are characterized by their grid ratio (ratio of the path length through the interspace material to the interseptal width), which typically ranges from 3.5:1 to 5:1. When a grid is used, the SPR is reduced approximately by a factor of about 5, leading in the most cases to a significant improvement in image contrast. Nevertheless, the grid causes the overall radiation fluence to decrease.

1.4.6 Image receptors in mammography

Early mammography x-ray imaging was performed with non-screen, direct exposure film which has produced low contrast images at higher radiation dose to patients. It is reported that mammography screening exams in the 1950s and 1960s, did not provide any useful benefits for the early detection of breast cancer as outcome was poor diagnostic quality (Bushberg et al 2002). In the 1970s and 1980s, mammography using Xeroradiographic process was very popular due to good spatial resolution and edge-enhanced images; however, this technique was also producing images with relative poor contrast sensitivity coupled with a higher radiation dose in comparison to the technologic advances of screen-film mammography imaging led to the demise of the Xerox process in the late 1980s (Bushberg et al 2002). Continuous development in imaging technology have vastly improved mammography over last 35 years starting form screen-film to digital images (Bushberg et al 2002). Digital mammography technology offers simplified archival, retrieval and transmission of images, reduction in mean glandular dose (MGD), higher patient workflow and improved diagnostic accuracy (Skaane 2010, Tabar 2012). Computed radiography (CR) is often distinguished from direct radiography (DR). However, CR and DR have many similarities as both technologies produce a digital image that can be enhanced for soft copy diagnosis or further review. Both CR and DR can also present an image within seconds of exposure. CR generally involves the use of a cassette that houses the imaging plate, similar to traditional film-screen systems, to record the image whereas DR typically captures the image directly onto a flat panel detector without the use of a cassette. Image processing or enhancement can be applied on DR images as well as CR images due to the digital format of each. CR also considered as a part of part of digital image technology where image is displayed upon

computer. Digital detectors (even with a lower spatial resolution than film) also appear to improve lesion conspicuity through their improved efficiency of absorption of x-ray photons, a linear response over a wide range of radiation intensities and low system noise (Tabar 2012). In addition, post-processing software can be utilized to assist the radiologist in evaluating the images for suspicious findings by altering contrast and brightness automatically or manually. Also in digital mammography system, the images can be displayed in hard and softcopy formats. Other advantage of using digital mammography is that computer aided detection (CAD) software can be utilized to highlight the abnormal areas of density, mass or calcification on the mammogram image.

The image detector produces the images by the absorption of energy from the x-ray beam. Image detectors should provide adequate spatial resolution, radiographic speed and image contrast. The detectors are divided into two categories 1) analog detectors that "reconstruct" the distribution in a continuous manner in the intensity scale 2) digital detectors that sample the distribution in space and in intensity (Figure 1.7). The detectors used in present mammography work are discussed in detail in this section.

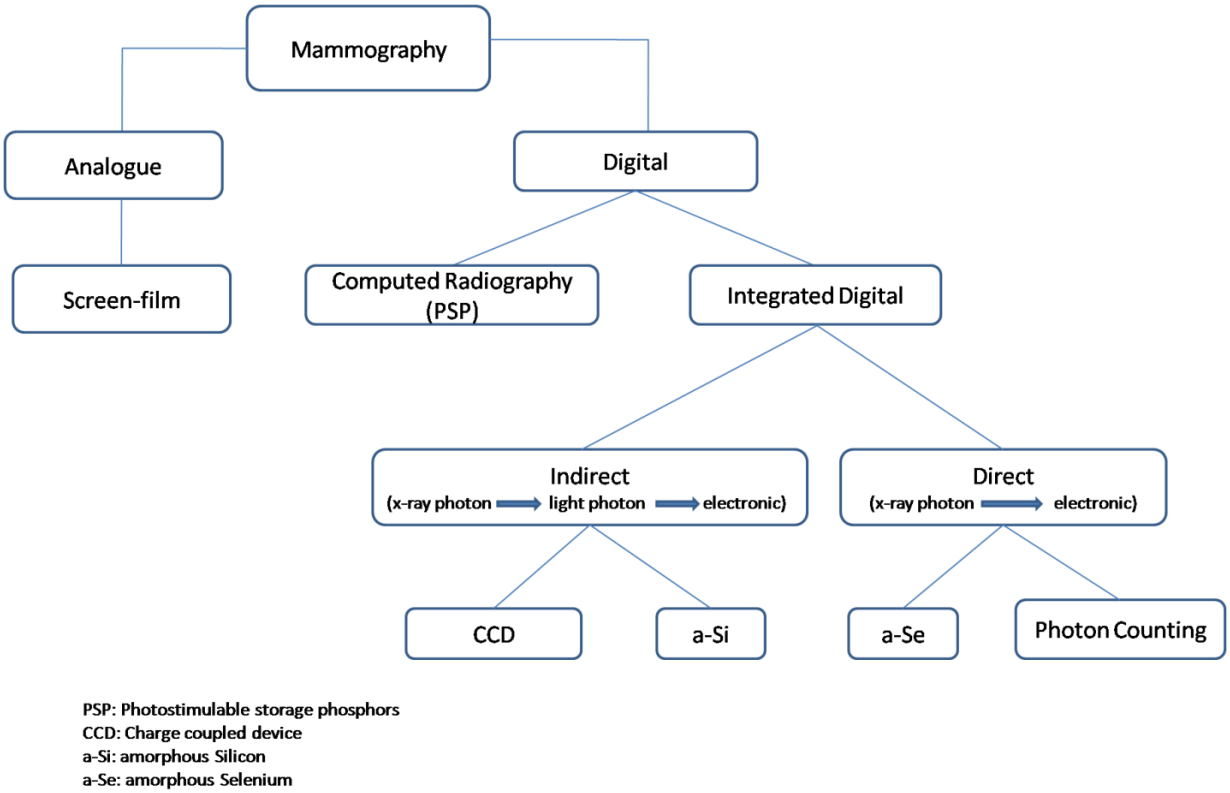

Figure 1.7 Various image recording detector technologies used in mammography

1.4.6.1 Screen film mammography (SFM)

Cassettes and screen-film combinations used in conventional mammography are designed such that the performance of the technique is enhanced. In screen film mammography, a high resolution fluorescent intensifying screen typically made up of the phosphor called gadolinium oxysulphide (Gd_2O_2S: Tb) is used. Purpose of using intensifying screen is to convert the x-ray energy into optical photon as the medical x-ray film is more sensitive towards optical light photon than x-rays. Mammography films are used in two sizes to match with the bucky size i.e 18 cm x 24 cm and 24 cm x 30 cm. Films used in SFM have higher film contrast and require significantly lower radiation exposure than the direct exposure films (approximately 50 to 100 times less) (Rothenberg et al 1995). A portion of the x-rays are absorbed or scattered by the internal structure and the remaining x-ray pattern is

transmitted to a photographic film (Silver Bromide (AgBr) emulsion) to record an image which can be viewed after its chemical processing for the evaluation. The emulsion comprises of a gelatin in which AgBr or AgI grains are embed.

In SFM, single side emulsion coated film mounted in contact with intensifying screen which is already fixed inside a mammography cassette as shown in figure 1.8. Intensifying screens are thin sheets, or layers, of fluorescent materials which are made of $CaWO_4$ or Gd_2O_2S: Tb. The transmitted x-ray energy from the patients' body is absorbed by the intensifying screen material, and a portion of it is converted into light depending upon conversion efficiency of the phosphor. The emitted light, in turn, exposes the film. Intensifying screens are used because film is much more sensitive to light than to direct x-radiation; approximately 100 times as much x-radiation would be required to expose a film without using intensifying screens.

Figure 1.8 Mammography cassette with single intensifying screen [Taken from konex.com.br]

Unfortunately, intensifying screens introduce blurring into the imaging process and places a limit on the visibility of detail that must be considered when selecting screens for specific clinical applications. In mammography exam, to attain the high image detail, single

screen and single emulsion coated mammography film is used to get rid of cross over effect as shown in figure 1.9.

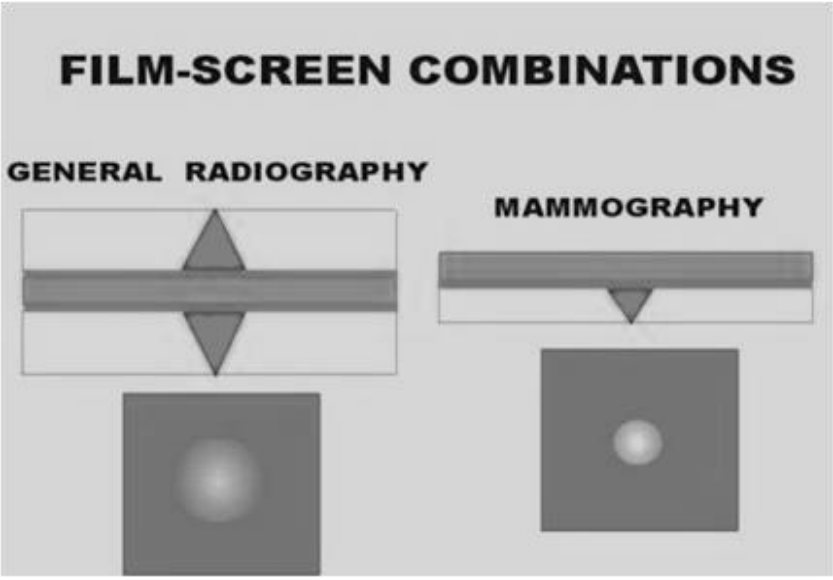

Figure 1.9 Single screen-film used in mammography exam to avoid cross over effect [Taken from www.sprawls.org]

1.4.6.2 Advantages/Disadvantages of screen-film mammography

SFM is considered to be the gold standard for the detection and diagnosis of breast cancer as it provides excellent detail resolution (image sharpness), which is very crucial for imaging microcalcifications and very small abnormalities that may indicate early breast cancer. The widespread popularity of the SFM system is due to its many inherent advantages, such as i) high spatial resolution (up to 20 line pairs per millimeter), which can demonstrate fine spiculations and microcalcification ii) high contrast, which allows visualization of subtle differences among soft-tissue densities (Mahadevappa 2004). SFM can provide spatial resolution of ~0.03 mm which is the highest among any other imaging modalities (Bushberg et al 2002). However, small deviations from optimal exposure and processing conditions can have profound effects in image quality (Andrew and Srinivasan 2012). Nevertheless, SFM

systems have certain limitations (Sabel et al 1996, Yaffe et al 1997). Drawback of using SFM is that sensitometric characteristics of the mammography film which is sigmoid in shape as shown in figure 1.10. This curve is also known as Hurter and Driffield (H&D) curve which results to the limited latitude i.e. the range of x-ray exposure over which the film display gradient is significant. If a tumour is located in a region of the breast that is either more lucent or more opaque, then the contrast displayed to the radiologist may be inadequate because of the limited gradient of the film. Hence women with dense breasts (breast containing large amounts of fibroglandular tissues) are of particular concern as the dense tissues with diffuse involvement of the breast with tumor tend to reduce the overall sensitivity of SFM (Yaffe et al 2009). Another limitation of SFM is the effect of fixed pattern noise due to the granularity of the phosphor screen and film emulsion. This impairs the detectability of microcalcifications and other fine structures within the breast. Also SFM suffers from compromises in spatial resolution versus quantum detection efficiency (QDE), which are inherent in the screen film image receptor (Yaffe et al 2009). As in SFM, film acts as the sole medium for acquisition, display, and storage of images and suboptimal conditions in any one step can affect the overall image quality. In addition, technical factors such as film processing, developing, and image artifacts can also limit the use of SFM. Development temperature, time and rate of replenishment of the developer chemistry has to be compatible with the type of film emulsion chemistry for maintain the sensitometric characteristics of film (Brink et al 1993). The inability to postprocess and optimize images often requires retakes, which can lead to multiple exposures, resulting in unnecessary radiation exposure to patients.

Approximately 10%–20% of breast cancers detected at breast self-examination or physical examination are not visible at SFM. Also, only 5%–40% of the lesions detected with

SFM and recommended for biopsy are found to be malignant (Laya et al 1996, Burrell et al 1996, Sickles 1991). This indicates a high level of false-positives, resulting in unnecessary biopsies and related psychological stress to patients.

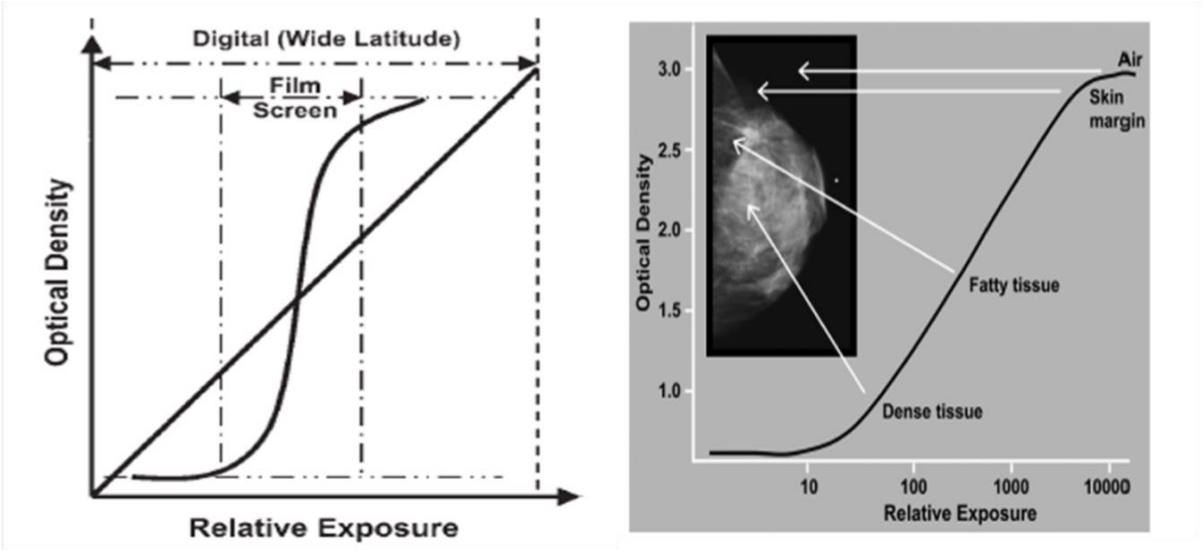

(a) (b)

Figure 1.10 Schematic of response curves for SFM and digital mammography (a) SFM has a limited dynamic range whereas digital mammography has a wider dynamic range (b) limitations of SFM showing different regions of the breast image according to the characteristic response of a typical mammographic film [Taken from Mahadevappa 2004]

1.4.6.3 Digital mammography

Digital mammography has the potential to overcome the limitations of SFM by improving breast cancer detection and lesion characterization at early stage (Feig and Yaffe 1998, Pisano 2000, Pisano et al 2000, Williams et al 1996). Commercial use of digital mammography (DM) started in year 2000 to overcome many technical the limitations of SFM. Digital mammography technology offers simplified archival, retrieval and transmission

of images, reduction in mean glandular dose (MGD), higher patient workflow and improved diagnostic accuracy (Skaane 2010, Tabar 2012). Acquisition is performed with low noise x-ray detectors having a wide dynamic range. DM images can be processed to enhance contrast and other features of the lesion. In digital mammography, differentially attenuated x-ray intensity is sampled in both the intensity and spatial domains to generate a digital x-ray image. In the intensity domain, the magnitude of the x-ray intensity is converted into a proportional electronic signal; this signal is then digitized so that it can be sent to a computer where the final image will be processed. In the spatial domain, the variation in the intensity signal over the area of the object represents the image information. Depending upon various detector technologies DM is explained in detail in the following section.

1.4.6.4 Photostimulable phosphor imaging plate

A technology used for digital mammography employs an image plate (IP) formed with a photostimulable phosphor (PSP) housed in lightproof cassette. PSP material is commonly barium fluorohalide doped with europium (BaFX: Eu), in which the halide (X) is a combination of bromide and iodide, typically 85% and 15%, respectively. The phosphor in a powdered form is mixed with a binder or adhesive material and laid down on a base with a thickness of about 0.3 mm. A surface coat protects the phosphor from physical damage. During mammographic exposure, transmitted x-rays from patient's body part gets absorbed into storage phosphor and generates electron-hole pairs and a fraction of generated charge is trapped in the crystal structure, creating a latent image proportional to the energy of the incident x-ray photon (Yaffe and Rowlands 1997). The number of trapped electrons is proportional to the amount of x-ray energy absorbed at a particular location in the detector. After exposure, the IP is placed in reader device and scanned with a red HeNe laser beam

(~620 nm). The energy of the laser light stimulates the traps to release the electrons. The transition of these electrons through energy levels in the phosphor crystals results in the formation of blue light photon. The emitted light is detected by a photomultiplier tube and converted to electric signals as shown in figure 1.11.

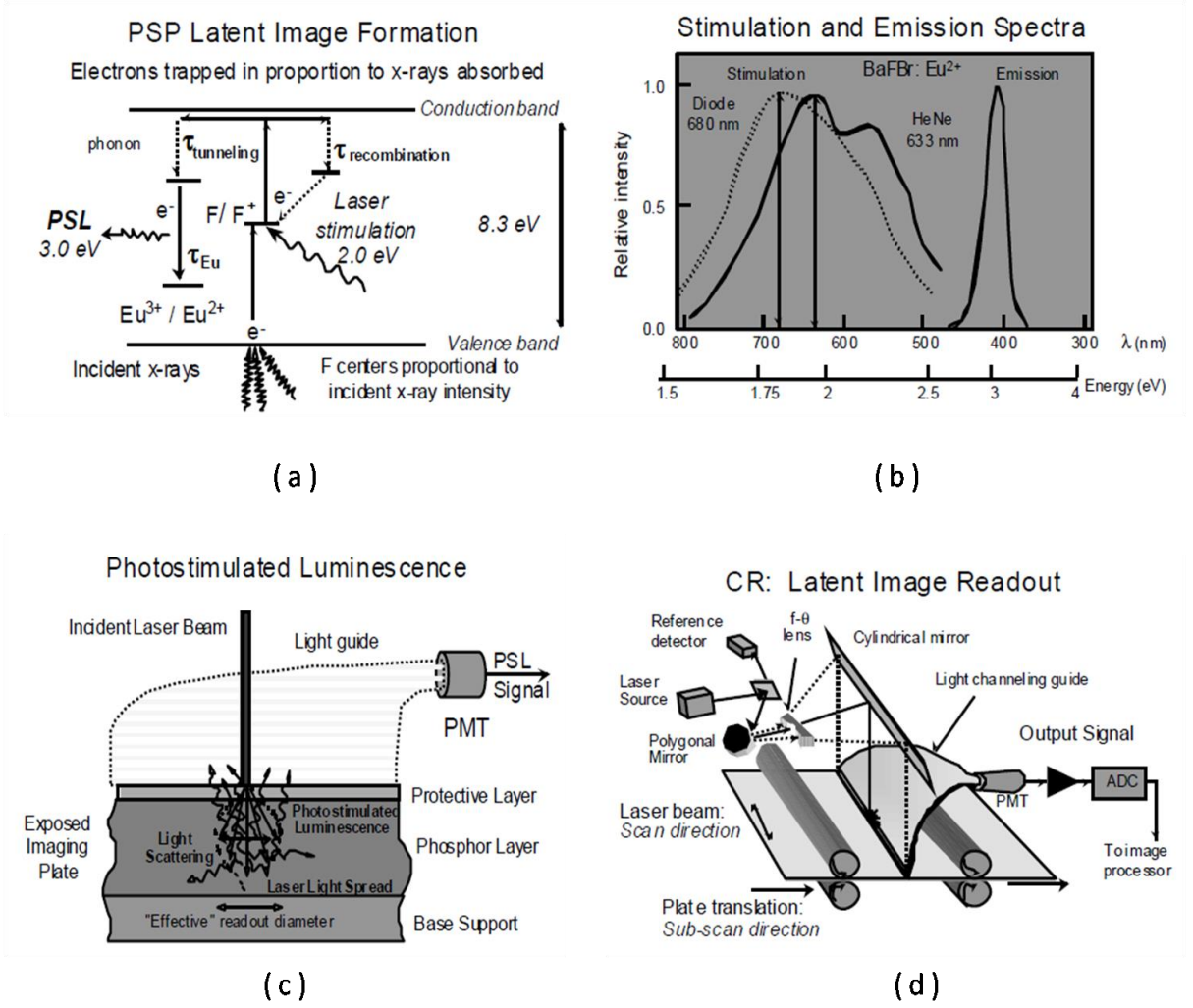

Figure 1.11 Schematic for CR imaging technique (a) latent image formation due to interaction of incident x-ray photon inside PSP (b) stimulation and emission spectra from phosphor (c) photostimulated luminescence and its collection by PMT (d) latent image read out process [Taken from AAPM 93 2006]

These electrical signals are processed and converted to a digital image Scanning is achieved using a rotating mirror. Above the plate, there is an array of optical fibers to direct the emitted light to one or more photomultiplier tubes to measure its intensity. Following the read cycle, the residual signal from the plate is erased by exposing it to a bright light source. The time for a CR reader to extract the image from the plate is generally between about 30 and 45 s, and the faster readers are capable of reading 100 or more plates per hour. The resolution of the image is determined by the size of scanning laser beam, the underlying scatter of the readout laser light in the phosphor and the distance between sample measurements.

There are several advantages of CR based mammography over SFM such as (i) the same plate can be used again and again; (ii) it does not require a dark room and developing chemicals; (iii) the produced image is digital and can be stored and manipulated electronically; (iv) these images have greater dynamic range, wider exposure latitude and reduced patient exposure. The digitized image can be viewed and enhanced using software that has functions similarly to other conventional digital image processing software, such as, for example, contrast, brightness, filtration and zoom.

1.4.6.5 Digital detectors

Digital detector based mammography can be categorized as indirect or direct. Indirect digital detectors utilize an indirect method of imaging x-rays, similar to screen-film. A scintillator absorbs the x-rays and generates a light scintillation that is then detected by an array of photodiodes. Indirect systems suffer from resolution degradation caused by light spread in the scintillator and poor quantum efficiency with thin scintillators. Direct digital detectors utilize a direct-conversion method of imaging, wherein the x-rays are absorbed and the electrical signals are created in one step. Systems using amorphous selenium represent a

direct technology for digital mammography. Selenium is an ideal material for a mammography detector because it has high x-ray absorption efficiency, extremely high intrinsic resolution, low noise, and a well-established manufacturing process.

In digital mammography images are formed directly onto a pixelized imaging device through the use of a scintillator or photoconductor, which captures the X-ray pattern (Yaffe 2010). Thin-film transistor (TFT) arrays commonly known as flat-panel arrays are composed of a matrix of discrete dels, each of which contains a transistor. TFTs are used as a read out system in flat panel detector technology. The transistors operate as gates, permitting an electric charge to flow through them only when they are turned on. During an x-ray exposure, the gates are turned off, and the image is built up in the dels in the form of an electric charge, with the amount of charge in each del proportional to the number of x-rays absorbed in that region of the detector (again, a linear relationship). There are two types of digital detector technology used in digital mammography i.e. indirect and direct. In an indirect device, an x-ray-to-light converter, similar to that used in SFM imaging, is placed in contact with the TFT array. Each del of the TFT array contains a light sensor (a photodiode) to convert the fluorescent light to a stored electric charge. In the indirect detection approach, a conventional x-ray absorbing phosphor, such as thallium-doped caesium iodide (CsI: Tl) or gadolinium oxysulphide (Gd_2O_2S) is grown onto the active matrix array. The detector pixels are configured as photodiodes made of amorphous silicon (a-Si) which converts the optical signal from the phosphor to charge and store that charge on the pixel capacitance. The advantage of utilizing CsI as the x-ray absorber is that it can be grown in columnar crystals shaped into 5–10 μm wide needles which act as fibre optics (Markus et al 2007). The advantage of CsI-based scintillators is that the crystals can be arranged perpendicular to the surface of the

detector and when coupled to the photodiode pixels, there is little lateral spread of light and, therefore high spatial resolution can be maintained. In addition, unlike conventional phosphors in which diffusion of light and loss of resolution become worse when the thickness is increased, CsI phosphors can be made thick enough to ensure high x-ray absorption while maintaining high spatial resolution (Yaffe et al 1997).

In a direct device, a layer of material is deposited directly onto the TFT array and when an x-ray photon is absorbed in this photoconductor material, an electric charge is generated and collected in the dels of the TFT array. In direct detector based digital mammography, a high atomic number photoconductor material called amorphous selenium (a-Se) is coated onto the active matrix area to form a photoconducting layer that directly converts the incident x-rays into charge carriers that drift towards the collecting electrodes under the influence of an applied electric field. The direct detection systems have advantages compared to the indirect systems. In the case of direct detection, since the produced charges are electrically driven towards the electrodes, their lateral spread, and hence the image blurring, is not significant (Yaffe and Rowlands 1997). Absorption efficiency of a direct detector can be maximized with the suitable choice of the photoconductor material, operating bias, and the thickness of the photoconductive layer (Kasap 2000). Finally, the direct systems are easier and cheaper to manufacture due to their simpler structure (Saunders et al 2004, Samei and Flynn 2003). However, the major disadvantages of direct detectors are the need for applying a high voltage to maintain electric field and the presence of dark current (Pisano and Yaffe 2005).

1.4.6.6 Digital breast tomosynthesis

Digital breast tomosynthesis (DBT) has rapidly emerged as an important new imaging tool that reduces the masking effect of overlapping fibroglandular tissue, thereby improving breast cancer detection (Hooley et al 2017). Under this technique, the compressed breast tissue is imaged in a quasi–three-dimensional manner by performing a series of low-dose radiographic exposures and using the resultant projection image dataset to reconstruct cross-sectional in-plane images in standard mammographic views (Peppard et al 2015).

1.5 Imaging methodologies

Medical x-ray images are produced based on different interaction mechanism such as attenuation, phase modulation, diffraction and scattering or their combination. All these interaction mechanism produce contrast in the image depending upon variety of object‘s physical properties such as absorption coefficient, refractive index, scattering coefficient, atomic number etc. In the thesis work imaging and dosimetric studies are carried out on the absorption and phase contrast based mammography x-ray imaging system. Hence the details of these two methodologies along with different interaction types are elaborated in the following section.

1.5.1 Interaction of x-rays with matter

Diagnostic x-ray images are formed when x-ray beam interacts with patient’s body and the differentially attenuated x-ray intensity is detected to produce a two dimensional image of the patients’ anatomy. In the diagnostic x-ray energy range, the main x-ray interactions with matter are photoelectric absorption, Thomson or Rayleigh (coherent/elastic) and Compton scattering (incoherent/inelastic. The probability of undergoing a particular interaction depends on the photon energy as well as on the density and atomic number of the

absorber, and is generally expressed in the form of an interaction cross section. X-ray interaction for energies, E< 511 keV is mainly due to photoelectric absorption, Compton scattering, and Rayleigh scattering (Cho et al 1975). X-ray attenuation is dominated by both Compton scattering and photoelectric absorption, while Rayleigh scattering photon interaction is negligible (Phillips and Lannutti 1997). In the following section, different x-ray interaction types are described which are responsible for producing the images in mammography.

1.5.1.1 Rayleigh (Coherent) scattering

This process is also known as coherent or elastic scattering in which an incident x-ray photon interact with an electron and gets deflected (scattered) without any loss of energy. This particular interaction raises the energy of the electron temporarily without removing it from an atom. The electron returns to its previous energy level by emitting an x-ray photon of equal energy but with a slightly different direction. According to theory of classical physics, the differential cross section of scattering of a photon from a free electron (Thomson scattering) can be derived by the following equation.

$$\frac{d\sigma_o}{d\Omega} = \frac{r_o^2}{2}(1+\cos^2\theta)$$

where r_0 is the classical radius of the electron, θ is the angle between the initial trajectory of the incident photon and the scattered photon, and $d\sigma_o/d\Omega$ is the differential cross section per electron of the classical scattering.

1.5.1.2 Photoelectric absorption

Photoelectric absorption involves the interaction of an incident x-ray photon with an inner shell electron in the absorbing atom that has a binding energy similar to but less than the energy of the incident photon. The incident x-ray photon transfers its energy to the electron and results in the ejection of the electron from its shell (usually the K shell) with a kinetic

energy equal to the difference of the incident photon energy E_i and the electron shell binding energy E_s. Energy of the ejected photoelectron, E_e is given as $E_e = E_i - E_s$

1.5.1.3 Compton (incoherent) scattering

In Compton scattering incident photon of energy E_i collides with an atomic electron, transfers some of its energy and momentum to the electron and is being deflected at an angle θ, with respect to its initial direction.

The energy of scattered photon E_c is given by:

$$E_c = \frac{E_i}{1 + \frac{E_i}{mc^2}(1 - \cos\theta)} = E_i \alpha$$

The differential cross section of incoherent scattering including electron binding effects can be given as the product of the Klein-Nishina differential cross section $d\sigma_{KN}/d\Omega$ and the incoherent scattering function of an atom $S(\tilde{p}, Z)$. Given equation provides the differential cross section of incoherent scattering.

$$\frac{d\sigma_{incoh}}{d\Omega} = \frac{1}{2} r_o^2 \alpha^2 \left(\frac{1}{\alpha} + \alpha - \sin^2\theta\right) S(\tilde{p}, Z)$$

1.5.2 X-ray absorption contrast imaging

In most of the conventional medical x-ray imaging this technique is used due to experimental ease and versatility. Under this imaging technique x-ray images are produced when differentially attenuated x-ray intensity transmitted from human body are recorded by an image detector placed next to the subject. In the conventional medical x-ray imaging with x-ray energy range (20-150 kVp), the main x-ray interactions with matter are photoelectric absorption,Thomson or Rayleigh (coherent/elastic) or Compton scattering incoherent/inelastic (Cho et al 1975, Phillips and Lannutti 1997). The probability of a particular interaction

depends on the photon energy as well as on the density and atomic number of the absorber, and is generally expressed in the form of an interaction cross section. Under x-ray absorption contrast imaging technique x-ray images are formed when incident x-ray intensity is attenuated inside human body following the Beer lamberts' law which is given by following equation (Jackson et al 1981).

$$I(x) = I_0 \exp^{-\mu(E)\,x}$$

I_0 = x-ray fluence in entrance

I(x) = x-ray fluence at position x =fluence in exit

μ (E) = x-ray linear attenuation coefficient (cm^{-1}), depends on x-ray photon energy,

The linear attenuation coefficient (μ) of a material responsible for the x-ray image contrast is dependent on the density of a material (Falcone et al 2005). In tissue, mass attenuation coefficient is expressed as μ /ρ (cm/gm), where ρ is the tissue density (gm/cm^3). Hence use of lower x-ray energy can produce good contrast images in mammography.

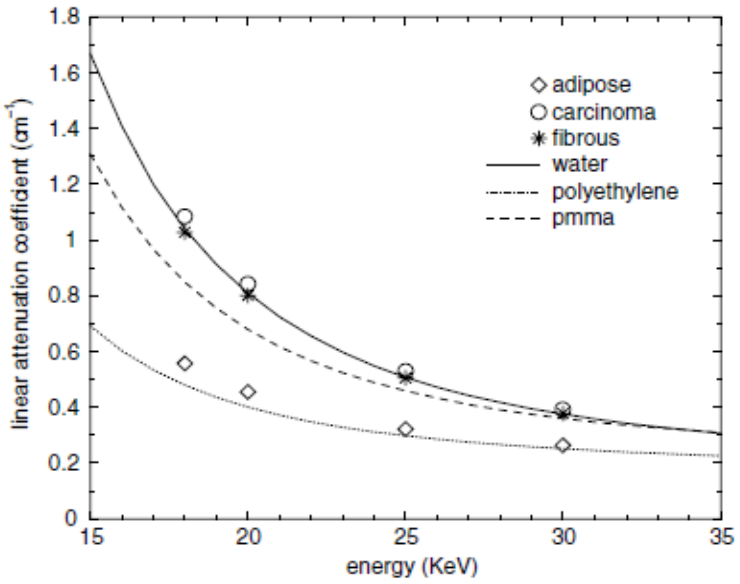

Figure1.12 Plot of linear attenuation coefficient for the normal, cancerous tissue and other soft tissue equivalent materials [Taken from Taibi et al 2003]

The Beer-Lambert's law is ideally valid for monochromatic x-ray source. In commercial x-ray devices where polychromatic x-ray sources are used, the additional filters are added to filter out low energy x-rays and also mathematical algorithms are applied to correct the artifacts such as distortion and false density gradients (Kelkar et al 2015).

1.5.3 X-ray phase contrast imaging (XPCI)

X-ray phase contrast imaging (XPCI) technique overcomes the limitation of absorption based x-ray imaging by providing improved visibility of structural features and small density variation in the material due to edge enhancement effect. Image produced under XPCI technique is based on physical effects that are different from absorption based conventional x-ray imaging, such as refraction, interference, scattering, etc. In medical imaging field, XPCI has been employed by three methods which are propagation, interference and analyzer based and present study employs the propagation based method for producing phase contrast. Propagation based XPCI technique relies on the principle of refraction of x-rays at the boundary defined by two different density regions. The refracted and direct wave propagates a finite distance and interferes due to a path difference to produce bright and dark fringes. Outcome of this interaction is manifested in terms of edge enhancement along the boundary of interest. Under XPCI technique, an air gap between the object and the detector is established to transform the phase gradients generated by the interference of x-rays having different phase shifts into intensity gradient on the image (Dreossi et al 2008, Matsuo et al 2005, Weon et al 2006). Use of a suitable imaging system with coherent source and high-resolution detector along with numerous optimized experimental parameters such as object to detector distance, beam energy and exposure time can produce projection images with optimum phase contrast and high resolution. When x-ray propagates through the matter, it is

described in terms of wave equation which considered to be the sum of incident and scattered radiation. Due to x-ray interaction with medium both of its amplitude & phase are modified which is described by the complex form of the refractive index 'n' of the medium, which for x-ray is very close to unity and is described as n=1- δ- iß, where δ is the index decrement that is responsible for the phase shift and ß is the absorption index ((Dreossi et al 2008, Matsuo et al 2005, Weon et al 2006).There are mainly two theoretical models to study mechanism of contrast formation in propagation based phase contrast imaging (PB-PCI) namely transport of intensity (TIE) equation and contrast transfer function (CTF). TIE and CTF, both explain the process of image contrast generation and give a quantitative relation between the image contrast and experimental parameters. TIE equation relate these variables with phase shift induced by a sample, through a differential equation while the CTF equation is based on solution of Fresnel propagation integral and relatively more complex (Langer et al 2007, Chukhovskii and Guigay 1993). Following section provides the detail of these two mechanisms of contrast formation in propagation based phase contrast image.

Transport of intensity equation (TIE)

The transport-of-intensity equation theory is proposed by T.E. Gureyev and K.A. Nugent in 1990s (Gureyev et al 1996). The TIE theory is mainly used to retrieve phase information from intensity distribution of a wave field. The TIE equation shows that phase shift introduced by a sample and the intensity recorded by the detector at sample-to-detector distance *z* are related by a second order differential equation as given below.

$$I(x, y, z = z) = I(x, y, 0)[1 - \frac{z\lambda}{2\pi} \nabla_{\perp}^{2} \phi(x, y, 0)]$$

The TIE equation shows that the phase contrast image intensity is decided by the second order derivative of phase. The TIE model uses a linear partial differential equation to approach to the non-linear procedures of x-ray transportation through samples and space under the under the short propagation distance approximation (Paganin 2006, Guigay et al 2007).

Contrast transfer function (CTF)

Another theory is proposed by S.W. Wilkins and the research group from CISRO called contrast transfer function (CTF). This theory is based on Fresnel diffraction model which explains that beam interaction with an object can be described by its optical transfer function and mathematically implemented by its multiplication to the wave function of incident wave (Paganin 2006, Guigay et al 2007). The CTF calculation is based on in-line approximation conditions. This is further propagated through free space in PCI and formulated by convolution of wave function with Fresnel propagator. Under this theory it is considered that the beam propagates in the z direction and r = (x, y) is a two dimensional vector in the direction transverse to propagation direction. Considering the transmission of a monochromatic, coherent, plane wave of unit intensity through an object described by the distribution of complex refractive index. Under small angle approximation, the equation

$$I_z(u) = I_0[\delta(u;\lambda) - 2\check{\mu}(u;\lambda)\cos(\pi\lambda z u^2) + 2\check{\varphi}(u;\lambda)\sin(\pi\lambda z u^2)]$$

called contrast transfer function relates the fourier transform of the image intensity to the experimental parameters such as wave length, propagation distance and detector resolution or object features though object frequency (u) under Born-type approximation i.e. weak absorption and phase in object $\mu(r) \ll 1$, $\varphi(r) \ll 1$.

There are various experimental parameters which affect image quality in XPCI such as source size and flux, coherence, parallel beam with divergence and polychromaticity. Hence optimization of all these parameters is required for achieving the good quality images.

1.6 Factors affecting image quality parameters

Image quality characterization is mainly based upon three primary physical parameters i.e contrast, resolution and noise (Andrew and Srinivasan 2012). Following section provides the detail description of these three image quality parameters.

1.6.1 Contrast

Contrast is defined as the difference in the image gray scale between closely adjacent regions on the image. In medical imaging contrast is the outcome of a number of different steps that occur during image acquisition, processing and display (Bushberg et al 2002). It depends upon many factors such as subject densities, atomic numbers and thicknesses. Sensitivity of an imaging system or technique to distinguish smallest object contrast is a measure of its merit and called contrast sensitivity.

1.6.2 Spatial resolution

Spatial resolution refers to the ability of an imaging system to record fine detail. Spatial resolution losses occur because of blurring caused by geometric factors (eg, the size of the x-ray tube focal spot, light diffusion in the receptor), detector element (del) effective aperture size, and motion of the patient relative to x-ray source and image receptor (Williams et al 2007). There are three types of radiographic blurring: (1) motion, (2) geometric and (3) image receptor. The reciprocal of it is called the Spatial Frequency, which is generally expressed in line pairs/mm (LP/mm) or cycles/mm. Spatial resolution of the image system can be assessed by imaging a pattern of evenly spaced x-ray opaque bars (100 percent contrast)

and determining the greatest number of cycles per millimeter (bars and spaces) that can be resolved. Unsharpness in the imaging process will eventually make the bars and spaces blur together. This defines the limiting spatial resolution (LSR) as the unsharpness causes the contrast between bars and spaces to become inadequate. A more sophisticated measure of resolution is MTF which describes the relationship between sharpness and contrast in imaging patterns whose x-ray transmission varies sinusoidally with position. Under MTF evaluation, Fourier methods are employed mathematically by measuring response of imaging system to a sharp edge input. Due to unsharpness created by factors in the imaging system, image of the sharp edge becomes spread out over a broader area than its ideal. The effect is seen in the plot profile, which consists of spread (tail) extending around the edge. This type of profile is called the Line Spread Function (LSF). The same type of effect can be seen in two dimensions using a pin hole and is called the Point Spread Function (PSF).When the Fourier Transform of an LSF is calculated, then the imaging system‘s response to sine waves of all spatial frequencies is obtained. This response is called the Modulation Transfer Function (MTF). It can be seen that the modulation falls off with increasing spatial frequency.

1.6.3 Noise

Radiographic noise or mottle is the unwanted variation in random optical density in a radiograph that has been given a uniform exposure. For screen film mammography, major sources of radiographic noise include: (i) quantum mottle, (ii) screen structure, (iii) film grain, (iv) film-processing artifacts, and (v) x-ray to light conversion noise (NCRP 149 2004). In digital mammography other than quantum noise, other form of noise is structural fluctuation in sensitivity over the area of the detector which is known as fixed pattern noise. Fixed pattern noise is defined as del to del sensitivity variation which remains constant over time. This

noise can be easily removed by applying a flat fielding or gain correction to each acquired image.

1.7 Mammography dosimetry

The estimation of the absorbed dose to the breast during mammography is a long-established part of quality control procedures for breast imaging systems and is also necessary for risk estimation (Dance and Sechopoulos 2016). Breast dosimetry is included in all national protocols for the quality assurance or quality control of mammography as well as in the international protocols of the European guidelines (EC 2013) and the IAEA 2007. It is evident from the various published studies that breast tissue is sensitive to radiation carcinogenesis, hence it is important to monitor the radiation dose delivered to the breast (NCRP 149 2004). In mammography, the potential carcinogenic radiation risk is more for the glandular tissues in the breast when compared to adipose, skin and areolar (nipple) tissues (NCRP 149 2004).

There are major variables that affect the breast dose per view delivered in a mammographic examination are: the choice of image receptor, the x-ray beam energy (HVL, and kilovolt peak), the degree of breast compression, and the breast size and adiposity. Female breasts vary greatly in size and adiposity resulting in significant range of dose values for a given technique. The compressed breast thickness affects dose to a great degree and hence must be specified to obtain accurate dose values. Both ionisation chamber and thermoluminescent dosimeters (TLD) have been used for MGD measurements. In mammography, the ionisation chamber response should be constant to ± 10 percent for beams of 0.3 to 1.5 mm Al HVL, and have a standard traceable calibration issued by the authorized national /international agencies (EC 1996). Most commonly used TLDs in mammography are LiF: Mg,Ti, LiF: Mg,Cu,P and Li_2B4O_7:Mn, because of their tissue equivalence.

1.7.1 Quantities and units used in mammography dosimetry

A wide range of x-ray spectra are used for mammography due to which it has been realised that the entrance exposure at the top of the breast is a poor measure of risk as the dose within the breast decreases rapidly with increasing depth. Evaluation of MGD for a given mammographic view requires knowledge of the x-ray exposure (free in air), the x-ray beam quality in terms of half value layer (HVL), operating potential and the compressed breast thickness.

****

Chapter 2

==========

Sensitometry of mammography film

==========

2.1 Introduction

In India screen-film mammography (SFM) systems are still in use at most of the rural areas and also at some of the areas in urban city. In SFM, the quality of the mammographic image depends upon the equipment and processing methods used for the films (Brink et al 1993). Light sensitometry is a suitable method to measure the performance of the processor and evaluation of the film performance (EC 2001, West et al 2000). Mammography technique requires high radiographic contrast that is influenced by subject contrast and film contrast. Film contrast depends upon the film type, film processor, processor chemicals/ processing cycles and fog. Different mammographic films present different sensitometric characteristics which can be altered by the processing conditions (EC 2001, Kimme-Smith et al 1989). Thus, in a mammography facility any change in film type, film processor, processor chemicals or processing cycles should be thoroughly investigated using standard techniques before mammograms of patients are acquired (AAPM 29 1990).

In mammography imaging, the film processor has been identified as the weakest link for production of the poor image quality. Several studies in this direction have reported that major cause for low contrast and high dose values observed in the mammography are due to poor film processing conditions (Murray et al 1992). The American College of Radiology (ACR, 1999) manual describes comprehensive procedure for processor quality control (QC) including processor operating levels, daily sensitometry and film crossover effects (ACR 1999). Also, according to the ACR mammography QC protocol, it has been recommended that for mammography film processing a dedicated processor unit should always be maintained as a typical single sided emulsion coated mammography films require more developing time for proper development since these are slow speed films (ACR 1999). A

survey by on-site visit of 30 mammography centers in Mumbai, India was conducted to acquire the information related to the processor type, processing temperature/time, chemicals, film and pH of the processing solutions as shown in table 2.1. Although various mammography centers have used both Kodak and Agfa mammography films but Kodak was the film which has been used in large quantity. In most of the surveyed centers it was observed that the measured and set temperature on the processor varied by more than 5ºC. Even the temperature control system of the processors was not working in many of the facilities. It was also observed that at some of the places manual processors were in use which has contributed large variation in the development time of mammography film. It was also observed that replenishment rate of the developer solutions were inadequate which resulted in a rapid decrease in the concentration of the developer solution. The use of a common processor for processing the medical x-ray films (radiography and mammography) in the radiology department was found to be the major reason for finding the inadequate replenishment. Also, at few centers it was observed that the pre-used and exhausted developer solution was sent back to the machine as replenishment.

In India where the work load for routine radiography is much significant in comparison to mammography workload, it becomes impractical to have a dedicated mammography processor. With the use of a common processor it becomes utmost important that the processor undergoes daily QC check and a record for the same is maintained and analyzed because the use of a common processor results in rapid decrease in the concentration of the developer solution if the replenishment rate is inadequate. During visit to the many mammography centers we have observed that none of the facilities were having processor QC equipments like sensitometer, densitometer, pH meter and digital thermometer. While

interacting with the mammography technologists working in these centers, it was found that majority of them are not aware about the mammography QC procedures.

The present study investigates the effect of changing the development temperature and time on the sensitometric indices like base plus fog, OD_{max}, AG and speed of Kodak MinR-2000 mammography film. The aim of the study was to emphasize the importance of dark room QC procedures to be carried out by the technologists in the mammography centers of India as it is well established that daily QC programme for the processing conditions will remove any discrepancy incurring due to processor related variables which may spoil the patient film images leading to retake.

Table 2.1 Summary of the survey conducted at 30 mammography centers, Mumbai, India to acquire information related to mammography processing conditions

Processor type (No. of processor units)	**Temperature control option**	**Measured temperature ranges**	**Processing time (seconds)**	**Processing chemicals used**	**Film used**	**Measured pH ranges of developer/Water/Fixer**
Kodak M 35 XO-Mat (8)	Inside	28-30 ºC	90	Kodak ,Agfa and Fuji chemicals	Kodak, Agfa	9.2-10.6 /7.0-7.1/ 4.0-5.8
Protec Optimax (7)	Outside	30-33 ºC	90	Kodak ,Agfa, Fuji and Rolex chemicals	Kodak, Agfa	8.5-10.1/6.9-7.0/3.6-4.9
Konica SRX-101A (2)	Outside	29-33 ºC	90	Kodak, Agfa, Fuji, Konica and Rolex chemicals	Kodak, Agfa	9.5-10.5/7.0-7.5/4.8-5.2
Promax (6)	Outside	29.5-33 ºC	90	Kodak, Agfa, Fuji and Rolex chemicals	Kodak, Agfa	9.0-10.7/6.9-7.2/5.0-5.3
Velopex ExtraX (3)	Inside	32.5-34 ºC	90	Kodak, Agfa and Fuji chemicals	Kodak, Agfa	8.9-10.3/7.1-7.2/3.9-4.8
Ecomax (1)	Outside	30- 30.5 ºC	117	Kodak, Agfa and Fuji chemicals	Kodak, Agfa	9.0-10.5/7.0-7.6/3.8-5.5
Manual (3)	Outside	26-28.1 ºC	Variable as per the technologists choice	Premier and Photon chemicals,	Kodak, Agfa	9.1-11.8/7.0-7.3/2.7-5.9

2.2 Materials and methods

2.2.1 Light sensitometry

A light sensitometer, with single flash and incorporated with blue and green emitting light sources and an optical step wedge was used for exposing the film. A Victoreen dual colour and dual control electronic sensitometer model 07-417 operated in the green spectrum was used to produce a 21-step sensitometric strip as shown in figure 2.1. Total 33 film strips were cut from a single Kodak MinR-2000 mammography film box. Assuming film to film variation is negligible, these film strips were randomly grouped together to form three sets comprising 11 film strips per set. Every subsequent step transmitted 40% more light than the previous step, and was associated with an increase of a log relative exposure of 0.30.

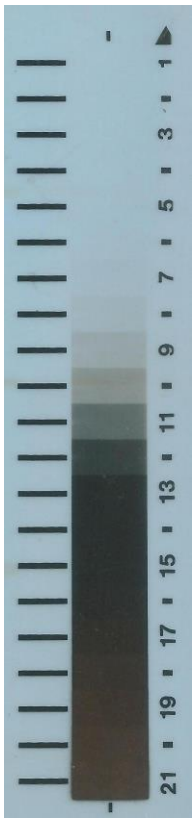

Figure 2.1 A filmstrip exposed for light sensitometry

2.2.2 Processing

A set of 3 film strips was exposed using a light sensitometer for a given processing temperature and time. To examine the effect of varying development temperature on the film sensitometric characteristics, these strips were developed in an automatic film processor (PROMAX^{TM}, Chayagraphics (India) Pvt, Ltd., Bangalore) with Rolex processing chemicals which has an outer knob for temperature control. Developer chemical is made up of hydroquinone ($C_6H_6O_2$) and metal/phenidone ($C_9H_{10}N_2O$) in which sodium sulphite is used as a preservative and potassium bromide as restrainer. Fixer chemical is made up of sodium/ammonium thiosulfate ($H_8N_2O_3S$) in which potassium alum ($KAl(SO_4)_2$) is used as hardener and sulfuric/acetic acid ($C_2H_6O_6S$) is used as acidifier. The processor model has a constant development time of 1.5 minutes. As the variation of development time was not possible in this automatic processor, a manual processing facility with Kodak chemical was employed to study the effect of varying development times on the film sensitometric characteristics at constant development temperature of $26^0C \pm 1^0C$. The manual processing facility comprises three anti-corrosion steel tanks each of 30 liters capacities which were separately mounted on the stands made up of iron rods. A digital thermometer having 0.1^0C resolution and $\pm 0.2^0C$ accuracy was used to measure the temperature of developer, water and fixer solutions. A pH meter having the range of -1.0 to 19 pH, resolution of 0.1 pH and accuracy of ±0.1 pH was used to verify the pH of the developer, water and fixer solutions.

2.2.3 Densitometry

The optical density is defined as the logarithmic ratio of the incident light intensity to the transmitted light intensity. For measurements of the optical density of the film strips a standard diffuse transmission Optel Trans-4 densitometer having white light source and

accuracy of △D = ±0.01 was used. To study the sensitometric indices of a mammography film, Hurter and Driffield (H&D) curves were plotted for three film strips corresponding to one set of processing condition. This densitometer was calibrated to a photographic density strip standards traceable to NIST, USA. Figure 2.2 shows the photograph of the processor quality control kit used in the study.

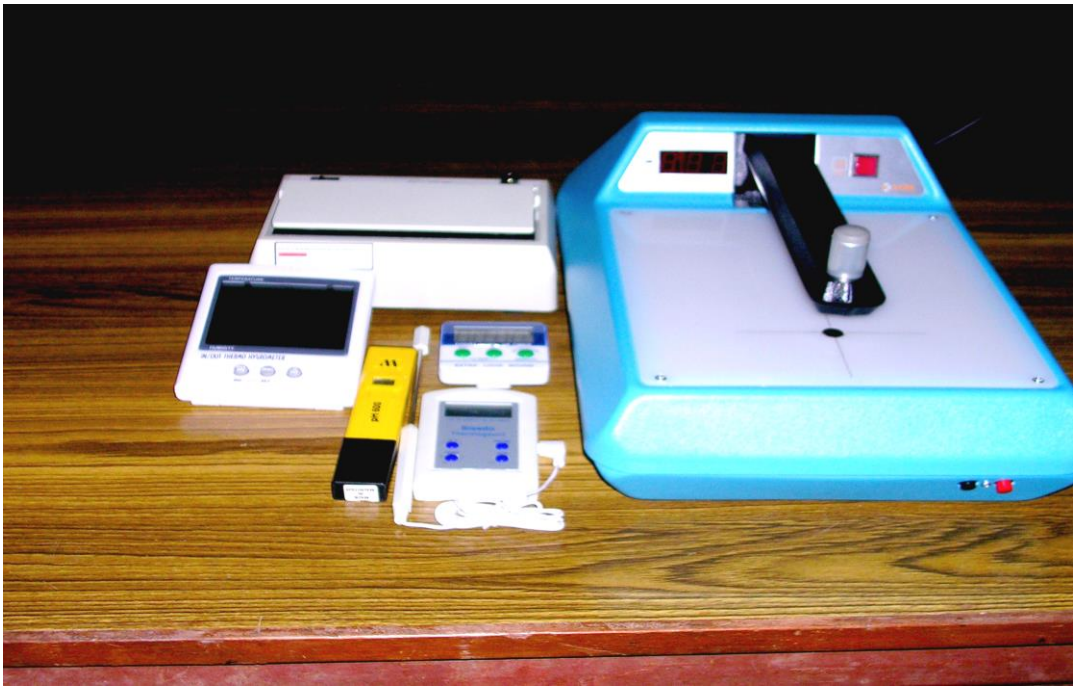

Figure 2.2 Photograph of processor quality control kit

2.2.4 Evaluation of sensitometric parameters

Characteristic curves were measured for five different development temperatures and six different development times. The base plus fog level, OD_{max}, average gradient (AG) and speed were calculated from the characteristic curve of each film strip. For a single set of processing condition three film strips were analyzed as we have processed the three film strips in a single processing condition. The mean values and standard deviations of these three film strips data were calculated.

2.2.4.1 Basic fog density

A base plus fog level of more than 0.20 OD is generally recommended as unacceptable (Sharma and Sharma 2012). Therefore measurement of this parameter is most important. The base fog density is defined as the optical density of an unexposed film simply after fixing the film whereas the base plus fog density is referred to the density of unexposed film when it is subjected to the complete film processing cycle.

2.2.4.2 Average Gradient ($\hat{G}$)

The average gradient of the characteristic curve is an indication of the contrast of the film. The average gradient is determined by the slope between the two points with an optical density of 0.25 plus base plus fog and an optical density of 2.0 plus base plus fog and is given by the expression $\hat{G} = (D_2 - D_1)/ (\log E_2 - \log E_1)$.

where D_2 and D_1 are net densities of 2.0+ basic fog and 0.25+ basic fog respectively and E_2 and E_1 are the corresponding values of exposures (in milli Roentgen). The required average gradient for a mammography film is ≥ 3.0.

2.2.4.3 Speed

The sensitivity or speed of a screen film system is derived from the sensitometric curve. The absolute speed of a screen film system can be determined from the sensitometric curve which is simply the inverse of the exposure (measured in Roentgens) required to achieve an OD of 1.0 + Basic fog.

2.2.4.4 Maximum optical density (OD_{max})

The maximum optical density which can be produced on the medical X-ray film is called its OD_{max} and its specified limit for a mammography film is ≥ 3.0 OD.

2.3 Results and discussion

Figure 2.3 shows the characteristic curves of a Kodak MinR-2000 mammography film at five different development temperatures (32, 33, 34, 35 and 37^0C) and a constant development time of 1.5 minutes. Figures 2.3.1 (a), 2.3.2 (b) and 2.3.3 (c) show the measured variation in the average gradient, film speed and OD_{max} of the film at five different development temperatures.

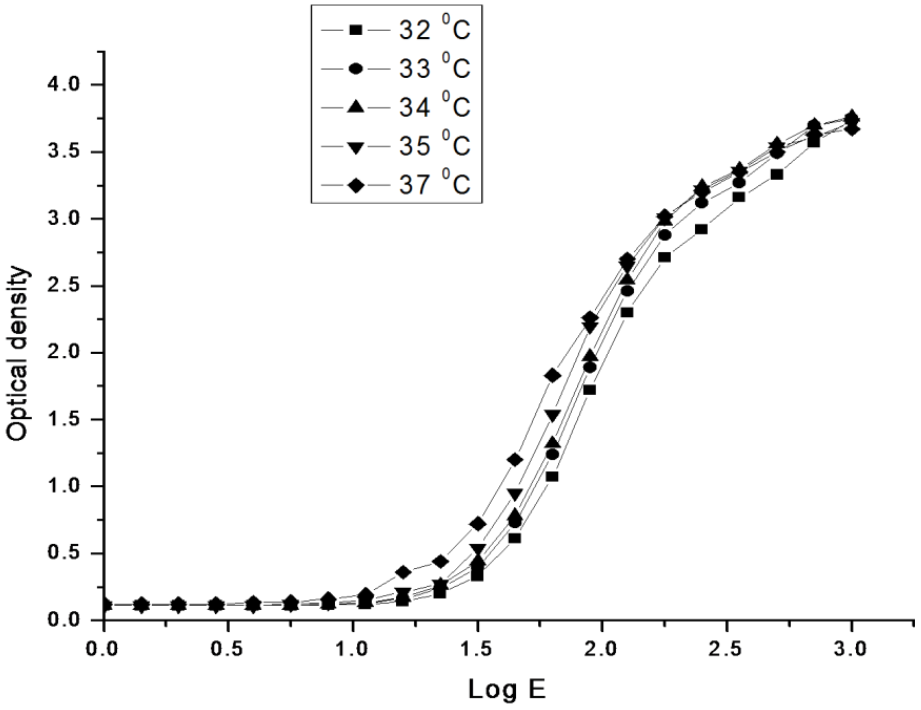

Figure 2.3 Characteristic curves of a single emulsion Kodak MinR-2000 mammography film at five different development temperatures at constant development time of 1.5 minutes

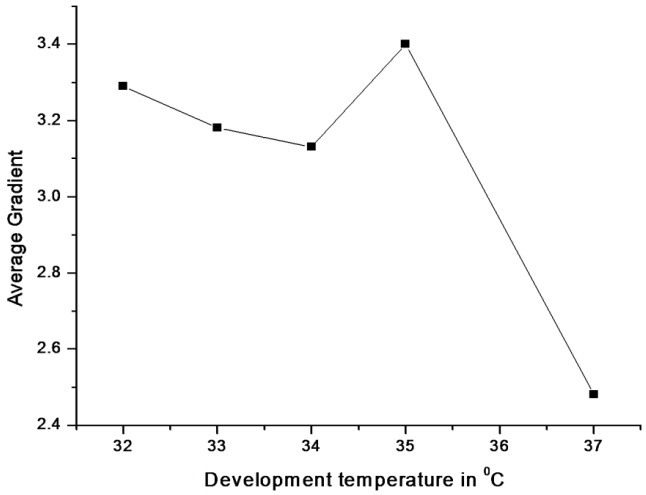

Figure 2.3.1 (a) Variation in the average gradient of a single emulsion Kodak MinR-2000 mammography film with varying development temperature at constant development time of 1.5 minutes

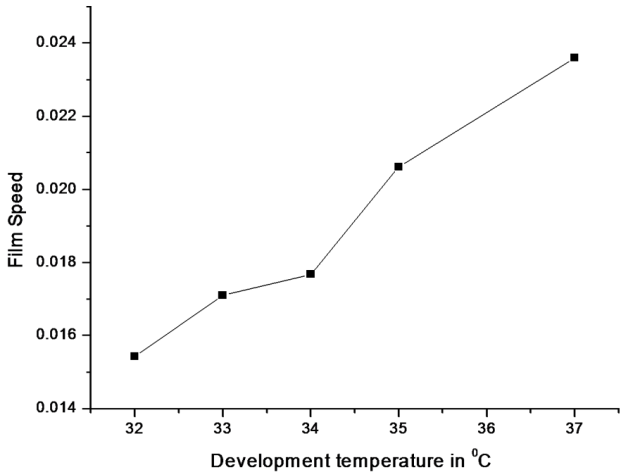

Figure 2.3.2 (b) Variation in the speed of a single emulsion Kodak MinR-2000 mammography film with varying development temperature at constant development time of 1.5 minutes

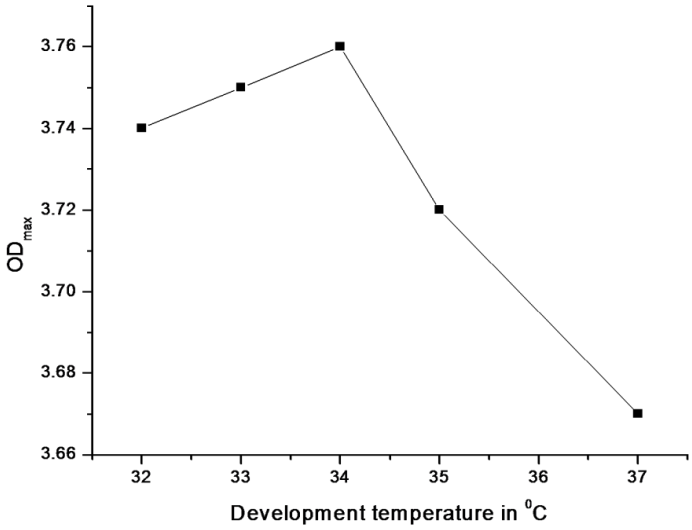

Figure 2.3.3 (c) Variation in the OD_{max} of the single emulsion Kodak MinR-2000 mammography film with varying development temperature at constant development time of 1.5 minutes

Figure 2.4 shows the characteristic curves of a single emulsion Kodak MinR-2000 mammography film at six development times (1, 2, 3, 4, 5 and 6 minutes) and a constant development temperature of $26^0C \pm 1^0C$. Figures 2.4.1 (a), 2.4.2 (b) and 2.4.3 (c) show the measured variation in the average gradient, film speed and OD_{max} of the film at six development times.

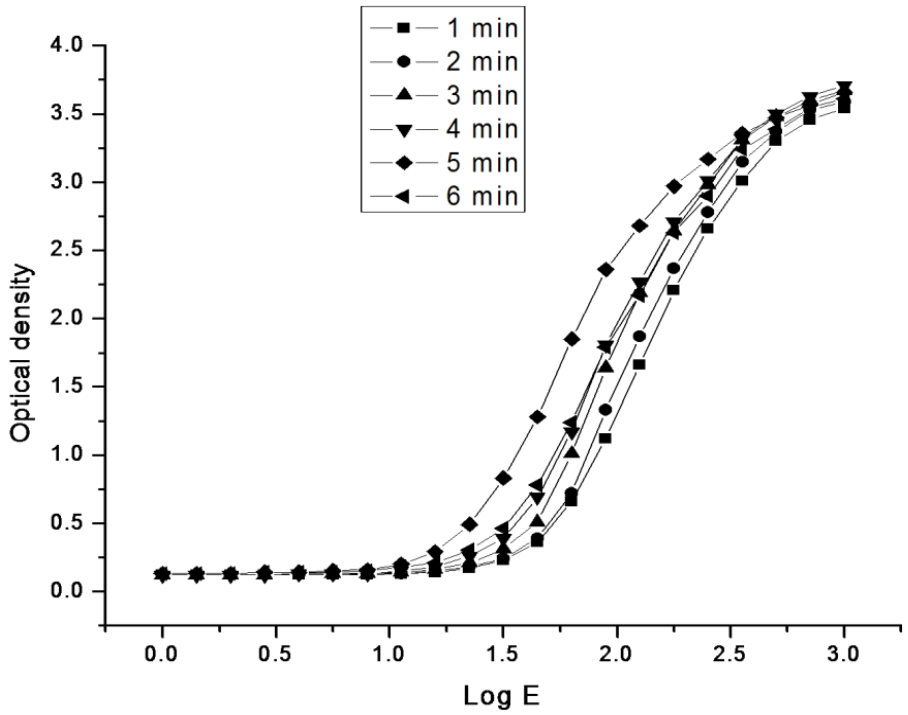

Figure 2.4 Characteristic curves of a single emulsion Kodak MinR-2000 mammography film at six different development times at constant development temperature of 26^0C

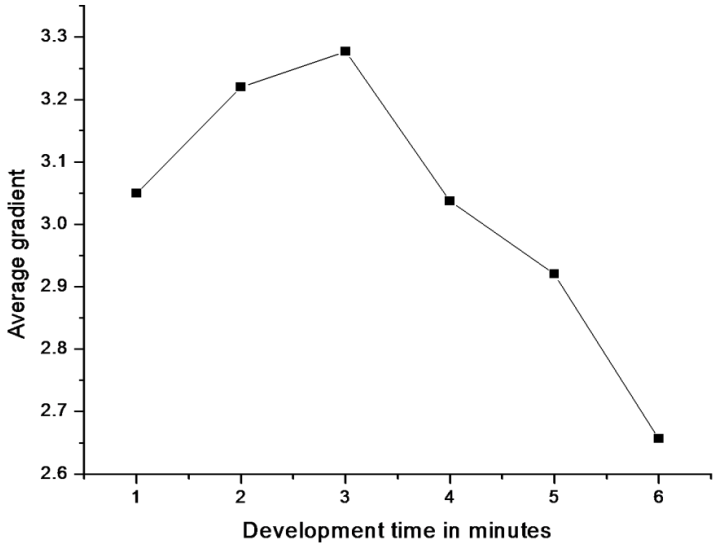

Figure 2.4.1 (a) Variation in the average gradient of a single emulsion Kodak MinR-2000 mammography film with varying development time at constant development temperature of 26^0C

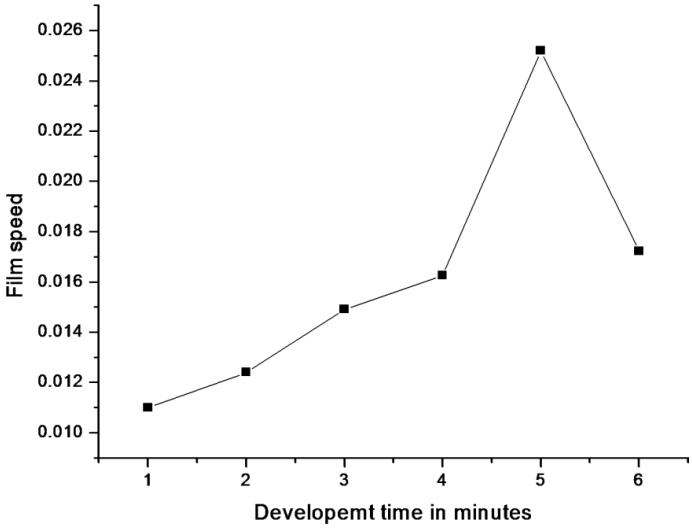

Figure 2.4.2 (b) Variation in the speed of a single emulsion Kodak MinR-2000 mammography film with varying development time at constant development temperature of 26^0C

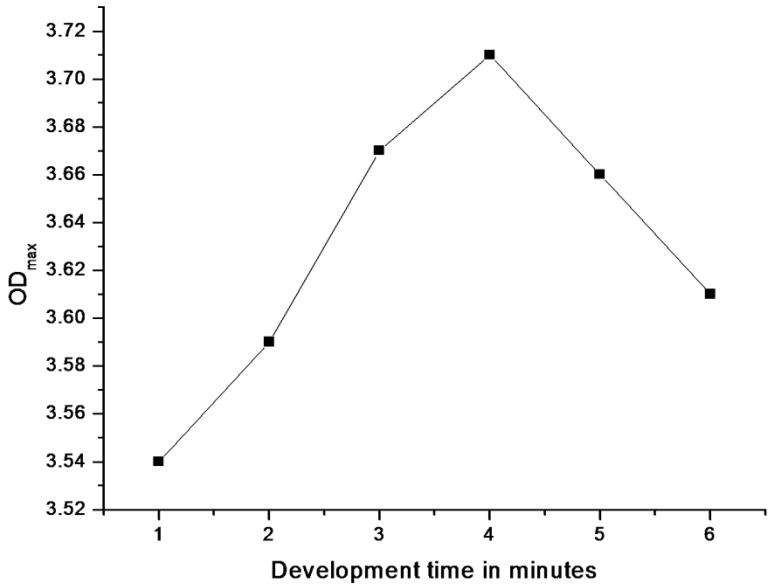

Figure 2.4.3 (c) Variation in the OD_{max} of a single emulsion Kodak MinR-2000 mammography film with varying development time at constant development temperature of 26^0C

2.3.1 Base plus fog level

The base plus fog levels of the film strips were not adversely affected with change in development temperatures and times involved in the study. Although not shown, the constant base plus fog level of 0.11±0.00 was recorded when the development temperature was varied from 32 to 37^0C. For the development times between 1 to 4 minutes the base plus fog level was 0.11±0.00 and for the development times between 5 mins to 6 mins the base plus fog level has the single value of 0.14±0.00.

2.3.2 Film contrast

The average gradient for the developing temperature and times is presented in figure 2.3.1 (a) and figure 2.4.1 (a) respectively. When the developing temperature was increased from 32^0C to 34^0C, the average film gradient decreased from 3.29±0.01 to 3.13±0.005

respectively at a fixed development time of 1.5 mins. There was a rapid increase in average film gradient from 3.13±0.005 to 3.4±0.00, when the developing temperature was increased from 34^0C to 35^0C which means an increase in contrast level of 23%. When developing temperature was increased from 35 to 37^0C there can be seen a rapid decrease in the average gradient of the film from 3.4±0.00 to 2.48±0.01 which means a decrease in contrast level of 37%. The average film gradient increased from 3.05±0.005 to 3.27±0.01 when the developing times were increased from 1 minute to 3 minutes at a fixed development temperature of 26^0C±1^0C. It is also observed that the average gradient starts decreasing from 3.27±0.01 to 2.66±0.02 when the times were increased from 3 mins to 6 mins.

2.3.3 Speed

The speed for the different temperatures and times are shown in figure 2.3.2 (b) and 2.4.2 (b) respectively. A rise in temperatures from 32^0C to 37^0C had an appreciable impact on the speed of a film which has increased from 0.015± 0.000 at 32^0C to a maximum value of 0.0236±0.000 at 37^0C which means a decreased radiation level of 56%. At a fixed development temperature of 26^0C±1^0C the speed increased when the developing times were increased from 0.011±0.000 at 1 min and to a maximum value of 0.025±0.000 at 5 mins which means a decreased radiation level of 25%. At development time of 6 minutes the speed of the film was measured as 0.017±0.000 which means an increased radiation level of 48% when compared with maximum speed obtained at 5 mins development time.

2.3.4 Maximum optical density (OD_{max})

The maximum optical density (OD_{max}) produced on a film for the different temperatures and times are shown in figure 2.3.3 (c) and 2.4.3 (c) respectively. A rise in temperatures from 32^0C to 37^0C shows the increase in OD_{max} of a film from 3.74 ±0.01 at

32^0C and to a maximum value of 3.76± 0.05 at 34^0C. It was also observed that when development temperature was increased from 34^0C to 37^0C, the measured OD_{max} decreases from 3.76±0.05 to 3.67±0.02 as can be seen hown in figure 2.3.3(c).

At fixed development temperature of 26^0C±1^0C, a rise in development times 1 min to 6 mins had an appreciable impact on the OD_{max} of a film as it is increased from 3.54 ±0.03 at 1 min and to a maximum value of 3.71±0.01 at 4 mins. When the development times were increased from 4 mins to 6 mins the OD_{max} decreases from 3.71±0.01 to 3.61±0.05.The observed OD_{max} values do not show much significant change with applied processing variables.

Alteration in the sensitometric indices e.g. average gradient, film speed and OD_{max} of a mammography film due to influence of development temperature and time can be seen in the study. In this context, it may be noted that Tsalafoutas et al (2004) has made an investigation to study the variation of the seven mammography films with processing conditions and showed that the different mammography films present different sensitometric characteristics that can be altered by processing conditions. It is evident from the present study that for the investigated film and processing variables, the best development temperature range is 32 to 35^0C for an automatic processor cycle time of ~1.5 minutes as on these settings the average gradient requirement needed for a film has been optimized. In case of required film speed and OD_{max} values the above said temperature settings are again considered to be the best choices. Also it can be seen from the figure 2.4 that the best suitable development time ranges for the manual processor setting applied in the study are 3 to 5 minutes for getting the optimized parameters investigated e.g. AG, film speed and $OD_{max.}$

2.4 Conclusions

Sensitometric characteristics of the Kodak MinR-2000 mammography film were evaluated with varying processing temperature and time. This mammography film is widely used in most of the mammography departments and shows the influence of processing conditions on its sensitometric characteristics. Although a single type of mammography film was used in this study, the effect of processing variables on any type of mammography film cannot be excluded which brought the changes in its sensitometric indices due to varying processing conditions. In depth analysis of sensitometric characteristics of a film from the contrast and radiation level point of view concludes that that there is a need for each mammography centre to carry out sensitometric study for their film and development chemistry to optimize the image quality and radiation dose levels.

****

Chapter 3

Development of mammography phantom

3.1 Introduction

Phantom based measurements in mammography are well suited for quality control and inter system comparisons (Craig et al 2001, ACR 1999, NCS 6 1993). Polymethyl methacrylate (PMMA) is among the best suitable materials for simulation of the breast (Dance et al 1999, Thilander-Klang 1997). It is an inexpensive readily available material which can be easily machined for making mammography phantom of desired geometry. Homogeneous PMMA phantom is suitable for dose measurements and quality control of the operational function of the automatic exposure control (AEC) unit. However, for studies of mammography image quality other phantoms need to be used (Thilander-Klang 1997). Commercially available mammography phantoms such as NA phantom (Nuclear Associates, Cleveland, Ohio, USA), CIRS-011A phantom (Computerized Imaging Reference Systems Inc. Norfolk, Virginia, USA), ACR accreditation phantom and BR-12/L-016A phantom (Ludlum Measurements Inc., Texas, USA) are used to measure image quality and mean glandular dose (MGD) during quality assurance (QA)/quality control (QC) testing of the mammography machine.

Presently, in India, mammography QC programme have not been initiated at national level and higher purchasing cost of the QC test tools including imaging and dosemetric phantoms are the major cause behind it. Considering the cost and availability of the mammography phantom, a PMMA phantom was developed for mammography imaging and dosimetry as import substitute to demonstrate its suitability in the quality assurance QA/QC of mammography systems. In screen-film mammography, the exposure is normally controlled by AEC system and the correct operation of this system is essential if mammograms are to be produced with a suitable film exposure. Calibration of the AEC system is required for the

correct film exposure to be obtained for the wide range of breast thicknesses and compositions. Under AEC mode, the radiation exposure is usually controlled by a detector positioned behind the image receptor which monitors the x-rays transmitted. The exposure is terminated when the monitor reaches a predetermined level corresponding to the desired optical density on the film. AEC compensation can be assessed using varying thicknesses of tissue mimicking materials such as Perspex and considering this a PMMA based thermoluminescent dosimeter (TLD) slot phantom was locally developed and fabricated which can be used to evaluate the various QC parameters of a mammography machine such as breast entrance exposure (BEE), MGD, percentage depth dose (PDD) /percentage surface dose distribution (PSDD), calibration check of AEC and density control function of a mammography machine. Under this study, a brief description of the phantom and its application for testing the various QC parameters of a mammography x-ray machine have been described.

3.2 Materials and methods

3.2.1 PMMA TLD slot phantom

The PMMA TLD slot phantom shown in figure 3.1 is made up of PMMA slabs of different length and radii. The length and radius of the central slab is of 21 cm and 10 cm respectively and every slab on either side of the central slab continue to decrease in length and radius at an interval of 5 mm respectively. The total thickness of phantom is 5 cm comprising total 10 slabs. The same sheet of PMMA was used while making the slabs of different radius and length to avoid the differences in thickness (Faulkner et al 1995). The thickness of each slab is 5mm and every slab has 15 TLD slots comprising 3 slots in a row at five different locations as shown in figure 3.1. The total thickness of developed phantom was kept 5 cm

because a comparison of entrance surface dose for radiographs of PMMA phantoms of varying thickness and compressed breasts of various thicknesses shows agreement for thicknesses of about 5 cm (Zoetelief et al 1989b). As a reference phantom for dosimetry, a 5 cm thick PMMA phantom has been recommended (NCS 6 1993).

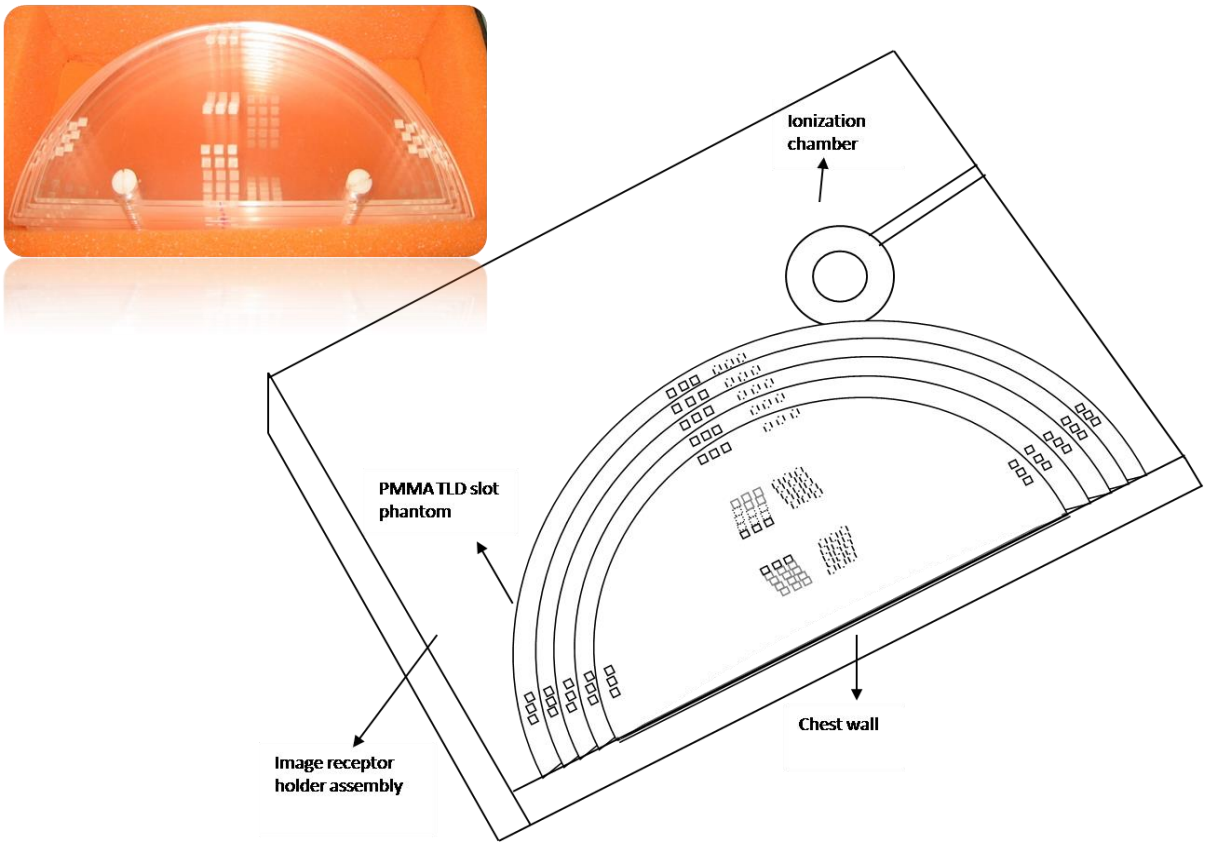

Figure 3.1 Schematic drawing of PMMA TLD slot phantom and photograph of original phantom having center slab of length 21 cm and radius of 10 cm along with ionization chamber for the measurement of the breast entrance exposure

3.2.2 Mammography x-ray machine

The mammography machine employed for testing of the phantom is a screen–film mammography (Model: Xtromam-2000, Xtronics Imaging Systems, Mumbai, India). The system contains image receptor assembly, moving grids and compression paddles for both 18

x 24 cm and 24 x 30 cm image receptors. The X-ray tube has Mo/Mo target filter combinations with 0.76 mm beryllium window and 30-µm molybdenum filters. The x-ray tube has a rotating anode and focal spot sizes of 0.3 mm^2 to 0.1 mm^2. The maximum operating potential and current of the unit is 35 kV and 60 mA. It has got a microprocessor controlled, full wave rectified generator of 3 kilowatt (kW) capacity. The available compression force range is 110 –200 Newton and is never more than 200 Newton, which is the tolerable limit. The compression paddle gets released immediately on the termination of the exposure. The compression paddle can be released manually in case of power failure. The x-ray tube insert is imported from UK (Varian Medical Systems). The HVL was determined for tube voltages from 24 kV to 35 kV with a Mo/Mo target filter combinations. HVL measurements of the mammography machines were carried out following the methodology recommended by American College of radiology (ACR 1999). The distance between the focal spot and the image receptor for the machine is 60 cm. Comprehensive QA tests were carried out before using this machine in the present study.

Various mammography guidelines/protocols recommended the use of different types of phantoms for dosimetry including PMMA phantom (Craig et al 2001, ACR 1999, Tung et al 2010, EC 2006). For comparing its percentage radiation transmission property with four other commonly available phantoms it was exposed at 28 kVp in the mammography machine.

3.2.3 Measurements of breast entrance exposure (BEE) and mean glandular dose (MGD)

All the exposure measurements were carried out on the XTROMAM-2000 mammography machine and before taking the phantom for exposure, the kilovoltage peak (kVp) reproducibility and half value layer (HVL) measurements of the machine were carried

out. For the measurement of HVL of the beam in Al (1100 alloy) and kVp, the Victoreen Model 8000, NERO^{TM} mAx (Inovision Radiation Measurements, Cleveland, Ohio, USA) along with an internal chamber (with an accuracy of ±1 kV and ±5% radiation output) was used. The calibration of this system was traceable to National Institute of Standards and Technology (NIST), USA. An external mammographic ionization chamber (Victoreen Model 6000-529, Volume 3.3 cc^3) with a calibration traceable to NIST, USA was used to evaluate the breast entrance exposure (BEE). The experimental set up of BEE measurement is shown in figure 3.1. The MGD values were derived from the BEE applying two different methods. In first method conversion factors given by Dance was used while in the second NCRP-149 recommended data was used (Dance 1990, NCRP 149 2004).

As per Dance's method, the MGD was calculated by multiplying BEE by a conversion factor 'p' which converts the air kerma for a tissue equivalent phantom to a model breast and another factor 'g' which is dependent on breast thickness and beam quality. The following equation for calculating MGD value from BEE was used.

$$MGD = K_f . g . p \qquad (3.1)$$

Where K_f is measured BEE without backscatter contribution from the phantom. As per NCRP-149 recommended method, the MGD was calculated by multiplying BEE by a conversion factor provided by Wu et al (1991). The following equation for calculating MGD value from BEE was used.

$$MGD = X_{ESE} \ . D_{gN} \qquad (3.2)$$

where X_{ESE} is the BEE and D_{gN} is the mean glandular dose (millirad) for 1 R entrance skin exposure (free in air) for Mo/Mo target/filter and 50: 50 glandular/adipose breast tissue combinations.

3.2.4 Thermoluminiscence dosimetry

LiF: Mg, Cu, P, chips (TLD-100 H, Poland make) of dimensions 3.2 mmX3.2 mmX0.38 mm were used in this study. This TL material was selected for dose measurements because of its sensitivity and near tissue equivalence for low energy photons used in mammography (IAEA HHS 2009). 200 TLD chips were stored in a specially fabricated galvanized Al tray which has engraved circular disc hole of diameter 5 mm and depth 0.5 mm in the matrix form of 15 x 15 rows and column. These chips were annealed at 240^0C for 10 minutes in an annealing oven having temperature control with an accuracy of ± 1^0C. After annealing, the TLD containing Al tray was placed in another Al tray for purpose of cooling. 200 freshly annealed chips were irradiated at 100 kVp uniformly in a Polydoros-LX, diagnostic x-ray unit (Siemens Ltd. Mumbai, India) with total filtration 3.6 ± 0.4 mm aluminium (Al). Chips having sensitivity variation within 1% were selected for further measurements.

TL response calibrations of the TLD-100 H chips were carried out at known doses corresponding to 22 kVp to 35 kVp in the mammography. Measurement for reading out of the exposed TLD chip was carried out in a Harshaw TLD reader (Model 3500).

3.2.5 Measurements of percentage depth dose (PDD) and percentage surface dose distribution (PSDD)

For PDD measurements, 3 freshly annealed chips of TLD-100 H were placed on central TLD slot of every slab of the PMMA TLD slot phantom as shown in figure 3.2. Total 30 chips were used for PDD measurement corresponding to a single kVp. For PSDD measurement corresponding to a single kVp, total 15 chips were used by keeping them at 5 different places on the surface of the phantom as shown in figure2. For both PDD and PSDD

measurement PMMA TLD slot phantom was positioned at 60 cm distance from the source. The measurements were made employing different mammography X-ray beam qualities at tube voltages of 24, 28, 30, 33 and 35 kVp. PDD Vs depth curves were plotted and a generalized fit equation was derived from the experimental data.

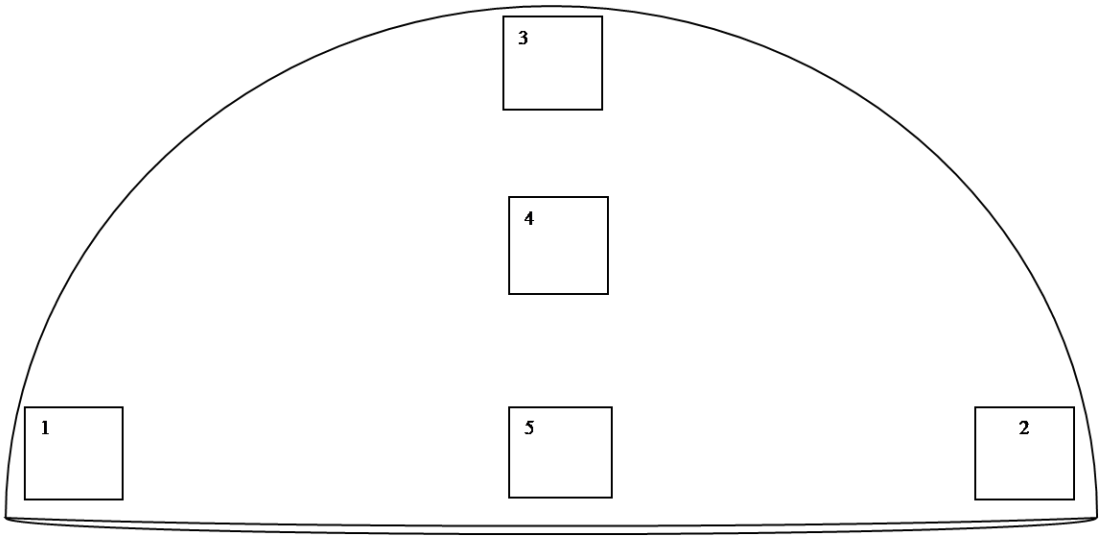

Figure 3.2 TLD positions at 5 different places in PMMA TLD slot phantom for measurement of the percentage surface dose distribution

3.2.6 Performance evaluation of automatic exposure control (AEC) system

AEC system of a mammography machine maintains a constant image optical density over a broad range of imaging techniques and patient variables. AEC performance of the XTROMAM-2000 mammography X-ray machine was evaluated using PMMA TLD slot phantom of 2, 3, 4, and 5 cm thickness. For evaluating the performance stability of this function, normal density setting i.e. '0' setting was used. The machine was operated in fully automatic mode in which automatically kVp and mAs get selected. PMMA phantom of varying thicknesses was positioned on the image receptor with dimensions of 18 cm x 24 cm. Kodak film loaded in a Kodak min- R-2 cassette with Kodak min- R-2190 screen was placed

in a bucky system for exposing the phantom every time. Prior to each exposure, it was ensured that the phantom fully covers the AEC system sensor. For every exposure, kVp and mAs were recorded. The image optical density was measured at the center of each of the phantom film using a standard diffuse (Optel Trans-4 (Indian) B/W) transmission densitometer having white light source and accuracy of $\triangle D = \pm 0.01$. The densitometer was calibrated against a photographic density strip standard traceable to NIST, USA. It is recommended that the image optical density should ideally remain constant within a variation of ±0.15 as phantom thickness and clinical technique factors are varied.

3.2.7 Performance evaluation of density control function

Density control function was evaluated using Kodak film, Kodak min- R-2 cassette and Kodak min- R-2190 screen. PMMA phantom of 4.5 cm thickness was used to represent medium thickness of breast. The phantom was exposed at 30 kVp under semi automatic mode i.e. manual selection of kVp, machine will adjust mAs itself. It was ensured that the phantom fully covers the AEC system sensor before giving the exposure. The phantom was exposed in the density range of -2 to +2 of machine and the image optical density was measured at the center of each of the phantom film.

3.3 Results and discussion

Results of the kVp reproducibility and HVL measurements of the XTROMAM-2000 mammography X-ray machine are given in table 3.1.The reproducibility of measured kVp was within the tolerance limits of ± 5% and of the specified values over the clinically relevant range of 22 kVp to 35 kVp.

Table 3.1 kVp reproducibility and measured HVL values of the XTROMAM-2000 mammography x-ray machine

Set kVp	Measured kVp	Measured HVL (mm Al)
22	21.90±0.24	0.32
24	23.98±0.11	0.34
25	25.10±0.12	0.36
26	25.56±0.17	0.37
28	27.82±0.15	0.38
30	30.24±0.21	0.40
32	32.14±0.15	0.41
33	33.00±0.10	0.42
34	34.10±0.07	0.43
35	35.12±0.08	0.43

Table 3.2 presents the measured percentage radiation transmission property of the developed PMMA TLD slot phantom and commercial mammography dosimetry phantoms. It can be observed from table 2 that % radiation transmission of all the phantoms including our phantom is approximately equal to each other with the range value of 3.03 to 3.83. This verifies the suitability of our PMMA TLD slot phantom for mammography dosimetry.

3.3.1 PDD and PSDD measurements

Figure 3.3 presents the variation of PDD with depth in PMMA TLD slot phantom at mammography beam energy of 24, 28, 30, 33 and 35 kVp with Mo/Mo target/filter combination. It is observed from this curve that PDD for all the five beam qualities follows the similar trend. This variation of PDD with depth in the phantom can be represented by the following general equation.

$$PDD(x, Q) = A_1(Q).\ Exp\ (-x/t1) + Y_0(Q) \qquad (3.3)$$

where A_1 and Y_0 are the fit constants the values of which depends on beam quality Q, x is the depth in cm and t1 is a fit parameter in cm^{-1} which are also dependent on beam quality Q. The exponential part of this equation represents the primary radiation which decreases with the depth. The values of the fit parameters for equation 3 for 24, 28, 30, 33 and 35 kVp with Mo/Mo target/filter combination are given in table 3.3. As can be seen from this table, the value of A_1 has the value in the range of 93.34 to 97.81, t1 ranges from 0.93 to 1.22 cm^{-1} and Y_0 has the values in the range of 6.48 to 2.68.

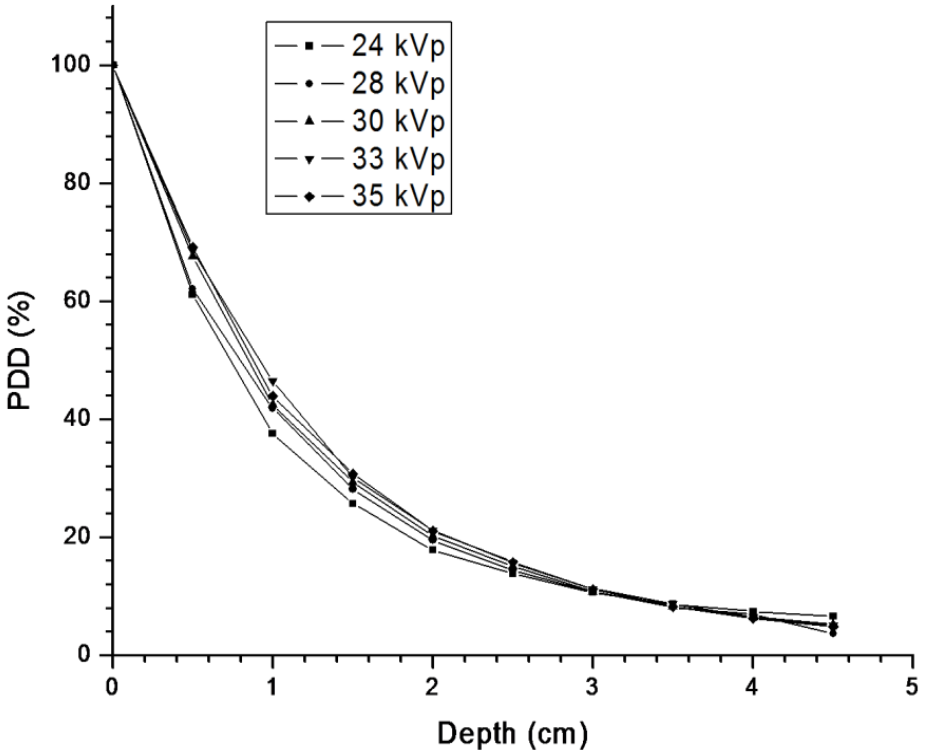

Figure 3.3 Variation of PDD with depth in PMMA TLD slot phantom at mammography beam energy of 24,28,30,33 and 35 kVp with a Mo/Mo target/filter combination

Table 3.2 Percentage radiation transmission and aluminium equivalence of the developed PMMA phantom with commercial mammography phantoms

Phantoms	**Compressed breast thickness (centimeter)**	**kVp (HVL in mm Al)**	**Percentage radiation transmission**	**Al equivalence (mm)**
BR-12	4.3	28 (0.38)	3.04	2.71
CIRS	4.5	28 (0.38)	3.34	2.61
ACR	4.2	28 (0.38)	3.83	2.49
NA	4.3	28 (0.38)	3.79	2.49
PMMA (developed)	4.5	28 (0.38)	3.03	2.71

Table 3.3 Values of fit parameters of equation 3

Mammography beam energy (kVp)	**A_1**	**t1**	**Y_0**
24	93.34	0.93	6.48
28	94.95	1.08	4.22
30	96.81	1.14	3.65
33	97.78	1.21	2.69
35	97.81	1.22	2.68

Figure 3.4 presents the variation of depth corresponding to PDDs of 75%, 50% and 25% in PMMA TLD slot phantom at mammography beam energy of 24,28,30,33 and 35 kVp with a Mo/Mo target /filter combination. PDDs of 75%, 50% and 25% were noted down from PDD Vs depth curve (Figure 3.3) and their corresponding depth values ranges from 0.32 to 0.40 cm, 0.73 to 0.92cm and 1.54 to 1.78 cm respectively. As the HVL increases, the depth increases because of increased penetration of the photons.

Table 3.4 gives the measured values of PSDD in developed phantom at 5 different places as shown in figure 4. The PSD values are evaluated with reference to dose at 4 cm distance from the chest wall edge. It can be seen from the table 3.4 that the position5 shows higher PSD value than in the other positions of phantom, which arises due to the orientation of the cathode-anode axis along the chest wall to nipple direction (Bushberg et al 2002).

Table 3.4 Percentage surface dose distribution in PMMA TLD slot phantom with reference to dose at 4 cm distance from the chest wall edge

kVp	**% Surface dose distribution (using TLDs) on Phantom at different positions**				
	Position-1	Position-2	**Position-3**	**Position-4 (at 4 cm distance from the chest wall edge)**	**Position-5**
24	94.45	95.23	97.99	100	100.92
28	97.78	97.90	98.79	100	101.21
30	96.8	96.82	99.04	100	102.96
33	97.79	97.89	97.97	100	102.20
35	95.79	97.5	98.71	100	102.33

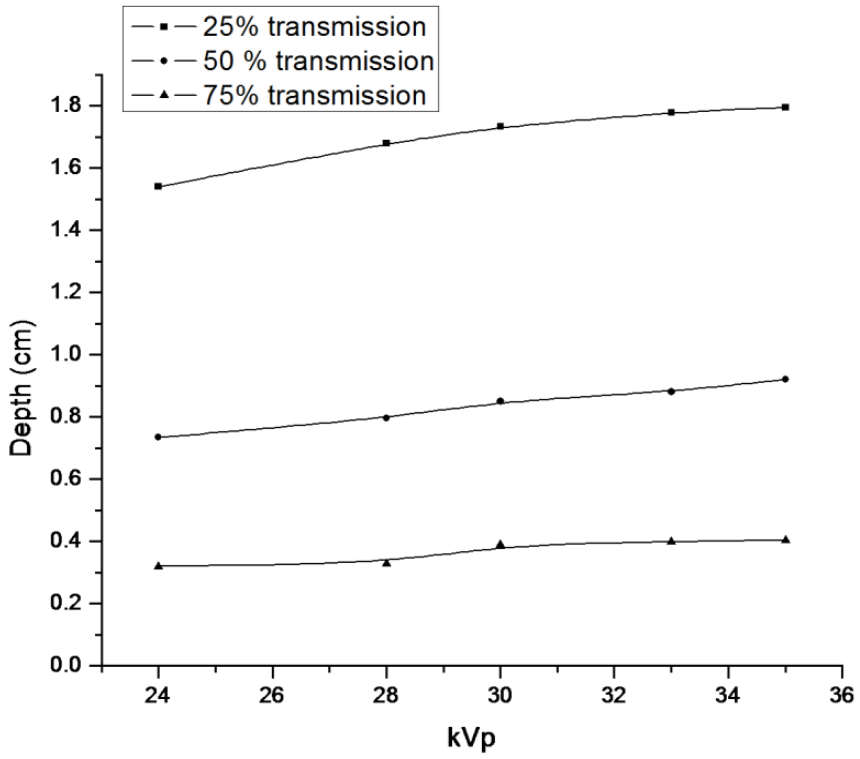

Figure 3.4 Variation of depth corresponding to percentage depth dose of 75%, 50% and 25% in PMMA TLD slot phantom at mammography beam energy of 24,28,30,33 and 35 kVp with a Mo/Mo target/filter combination

3.3.2 AEC and density control function performance

Table 3.5 and 3.6 presents the result for AEC and density control function configuration testing of Xtromam-2000 mammography machine using a developed phantom. The results obtained for AEC configuration testing show that the observed mean optical density of the phantom image was 1.59 O.D and optical density difference for every successive increase in thickness of the phantom was observed to be within ±0.15 O.D.

Table 3.5 Performance testing of AEC configuration of Xtromam-2000 mammography machine using different thicknesses of PMMA TLD slot phantom

Density setting: Normal **Anode/Filter: Mo/Mo** **AEC Mode: Fully Auto i.e. automatically machine will select kVp and mAs**										
PMMA Phantom thickness (cm)	**kVp**	**mAs**	**HVL (mm Al)**	**BEE (mR)**	**MGD (mGy) (Dance 1990)**	**MGD (mGy) (NCRP-149)**	**Percentage difference in MGD**	**Image O.D**	**Mean O.D**	**Variation in image O.D from Mean O.D**
2	26	47	0.37	297	1.312	0.989	32.6	1.69	1.59	+0.10
3	29	65	0.39	500.8	1.616	1.319	22.5	1.50		-0.09
4	30	89	0.40	824	2.048	1.733	18.2	1.62		+0.03
5	31	120	0.41	1094.6	2.229	1.890	17.5	1.54		-0.05

Table 3.6 Density control function testing of Xtromam-2000 mammography machine using PMMA TLD slot phantom

Set kVp:30, HVL=0.40 mm Al **Mode: Semi Auto (select kVp manually machine will adjust mAs itself)** **Anode/Filter: Mo/Mo** **Compressed thickness of PMMA phantom =4.5 cm**								
Density control setting	**mAs**	**Breast Entrance Exposure (mR)**	**MGD (mGy) (Dance 1990)**	**MGD (mGy) (NCRP -149)**	**Percentage difference in MGD**	**Image O.D**	**Normal density setting O.D**	**Variation in image O.D from normal density setting O.D**
-2	40	425.18	0.942	0.799	17.9	1.45	1.56	-0.11
-1	50	554.8	1.232	1.042	18.2	1.50		-0.06
0	60	687.4	1.523	1.292	17.9	1.56		-0.00
+1	70	758.0	1.683	1.424	18.2	1.73		+0.17
+2	78	888.4	1.971	1.669	18.1	1.85		+0.29

It is recommended that the AEC shall be capable of maintaining film optical density within ±0.15 of the mean optical density when the thickness of a homogeneous material is varied over a range of 2 to 6 cm and the kVp is varied appropriately for such thicknesses over the kVp range used clinically in the facility (Craig et al 2001, ACR 1999). Under density control function testing, it was observed that at -2 and -1 density setting of the mammography machine, the observed variation in film image O.D was within ±0.15 O.D of the normal density setting '0' and at density settings of +2 and +1, it was observed that the variation in film image O.D was within ±0.30 O.D of the normal density setting'0'.

3.4 Conclusions

The developed PMMA phantom is an inexpensive tissue equivalent phantom which can be fabricated easily. The studies carried out using the phantom indicate that it is equivalent to other commercial phantoms and can be used to measure many mammography QC parameters including phantom dosimetry. The results of the study concludes that the developed phantom can be used for initiating the quality audit programme involving phantom dosimetry and system performance studies of the mammography centers at national level.

****

Chapter 4

Image quality and dosimetry of digital mammography system

4.1 Introduction

In India, screen-film mammography (SFM) is gradually being replaced by digital mammography systems mainly in urban areas of the country due to its several advantages over SFM. Digital mammography has the potential to overcome the several limitations of SFM and has also shown the improved breast cancer detection and lesion characterization at an early stage (Feig et al 1998, Pisano 2000, Pisano et al 2000, Williams et al 1996). The major disadvantage with SFM technique is the limited dynamic range, trade-offs between dynamic range and contrast resolution, noise due to film granularity, and compromise between resolution and efficiency. Whereas digital mammography technology offers simplified archival, retrieval and transmission of images, reduction in mean glandular dose (MGD), higher patient workflow and improved diagnostic accuracy (Skaane 2010). Digital mammography utilizes digital detectors having wider dynamic range and is categorized on basis of direct and indirect flat panel detector technology. Digital detectors (even with a lower spatial resolution than film) also appear to improve lesion conspicuity through their improved efficiency of absorption of x-ray photons, a linear response over a wide range of radiation intensities and low system noise (Tabar 2012). In addition, post-processing software can be utilized to assist the radiologist in evaluating the images for suspicious findings by altering contrast and brightness automatically or manually. Also in digital mammography system, the images can be displayed in hard and softcopy formats. Other advantage of using digital mammography is that computer aided detection (CAD) software can be utilized to highlight the abnormal areas of density, mass or calcification on the mammogram image.

Image quality characterization of any x-ray based imaging system is evaluated by measuring three primary physical parameters: contrast, resolution and noise and the quantification of these metrics can be done by evaluating objective image quality parameters

defined as contrast to noise ratio (CNR), modulation transfer function (MTF) and noise power spectra (NPS) (Andrew and Srinivasan 2012). CNR defines the image contrast of a digital imaging system. Also, CNR measurement is very useful for assessing the performance of automatic exposure control (AEC) system that can be related to the effect on threshold object thickness of a given system (Young et al 2010). In the present study, we have evaluated the image quality of direct flat panel based mammography systems by measuring CNR values under clinically used operating conditions following the European protocol (Perry et al 2006, Baldelli et al 2009). Present days, a new concept called as figure of merit (FOM) is used as a tool in digital mammography to assess the performance in terms of image quality and patient doses (Borg et al 2012, Williams et al 2008). FOM of digital mammography system was evaluated in terms of CNR^2/MGD under automatic exposure control (AEC) and clinically used OPDOSE mode using indigenously made polymethylmethacrylate (PMMA) phantom having different thicknesses (Borg et al 2012, Williams et al 2008, Sharma et al 2012). OPDOSE mode selects the best target/filter combination depending on breast thickness, density, whereas AEC mode selects optimize exposure parameters for each individual breast size and composition and determines the dose based on the contrast needed for the image. European guidelines for quality control in Full-Field Digital Mammography (FFDM) recommends to measure the threshold contrast (i.e. the lowest contrast value for which the objects are visible) visibility under clinical conditions which is used to express the image quality (van Engen et al 2006). Also several studies have also reported that measurement of contrast detail resolution of the digital mammography system is also an essential part as it helps to visualize the objects with very small contrast and diameter from the background (Thomas et al 2005, van derBurght et al 2010, Young et al 2008, E-Cabrera and Brandan 2015, Figl et al 2015, Rivetti et al 2006, Konstantinidis 2014, Rojas et al 2017, Fausto 2017,

Samei and Flynn 2002). Contrast detail resolution studies on the digital mammography system simulating the clinical operating conditions were carried out using the Artinis make Contrast-Detail Mammography (CDMAM 3.4) phantom.

MTF measurement describes the sharpness of digital imaging detector at different spatial frequencies and gives the quantitative analysis of spatial resolution (Samei and Flynn 2003). Various methods have been employed for deriving MTF quantity which is based on slit, edge and bar pattern (Samei and Flynn 2003, Samei et al 2005, Perry et al 2013). Also for any digital imaging system, noise characterization through estimation of the noise power spectrum (NPS) is a central component (Williams et al 1999). NPS measurement of digital mammography system describes the noise amplitude and texture observed in images obtained with a uniform filed of radiation (Williams et al 1999, Borasi et al 2003, Salvagnini et al 2013, Padgett and Kotre 2005, Siewerdsen et al 2002, Marshall 2007, Ranger et al 2005). In this paper we report an edge method which was used for deriving MTF of a direct digital mammography imaging system. Under NPS measurement, variance of image intensity divided among its frequency components is calculated from ROIs taken from a region of a uniformly exposed image. In the present study we have evaluated NPS from the uniformly exposed digital mammography images following the European Guidelines.

Estimation and optimization of mean glandular dose (MGD) is an important component of quality control (QC) programme in mammography due to associated risk of radiation-induced carcinogenesis (Dance et al 2000). Also in case of digital mammography single dose measurement at one thickness is not sufficient and it requires different PMMA thicknesses and breast simulating phantoms to measure the radiation doses (Sharma et al 2012, Bick and Diekmann 2010). Hence, MGDs for the digital mammography system was measured using different breast tissue simulating phantoms.

4.2 Materials and methods

4.2.1 Digital mammography x-ray machine

Mammomat Inspiration digital mammography machine (Siemens Medical Systems, Germany) was employed for all the measurements as shown in figure 4.1. The Mammomat Inspiration is DR based mammography machine which contains Molybdenum (Mo) and Tungsten (W) targets. This machine also contains different filters, namely 30 μm Mo for Mo target, 25 μm rhodium (Rh) for Mo target, 50 μm Rh for W target. The operating kilovoltage of the machine is in the range of 23-35 kV at an increment of 1 kV and the focus-to-imager distances (FIDs) are 65.0 cm 65.55 cm for Mo and W targets respectively. Exposure modes available with the machine are OPDOSE, AEC and manual. The image receiver of the machine contains solid-state amorphous selenium (a-Se) detector with pixel size of 85 μm. The detector size is 24×30 cm^2 but the irradiation field is automatically collimated to 18×24 cm^2 when the smaller compression paddle is fitted.

4.2.2 Mammography phantoms

CIRS mammography research set (012A), CIRS mammography accreditation phantom (015A) supplied by Computerized Imaging Reference Systems (CIRS), Norfolk, Virginia, USA, and in-house developed PMMA phantom (Referred as BARC PMMA phantom) were used to carry out the dosimetry measurements with digital mammography systems (Sharma et al 2012). The CIRS mammography research set contains three different breast tissue equivalent phantoms having semispherical shapes and total thicknesses of 4, 5 and 6 cm (Figure 4.2).

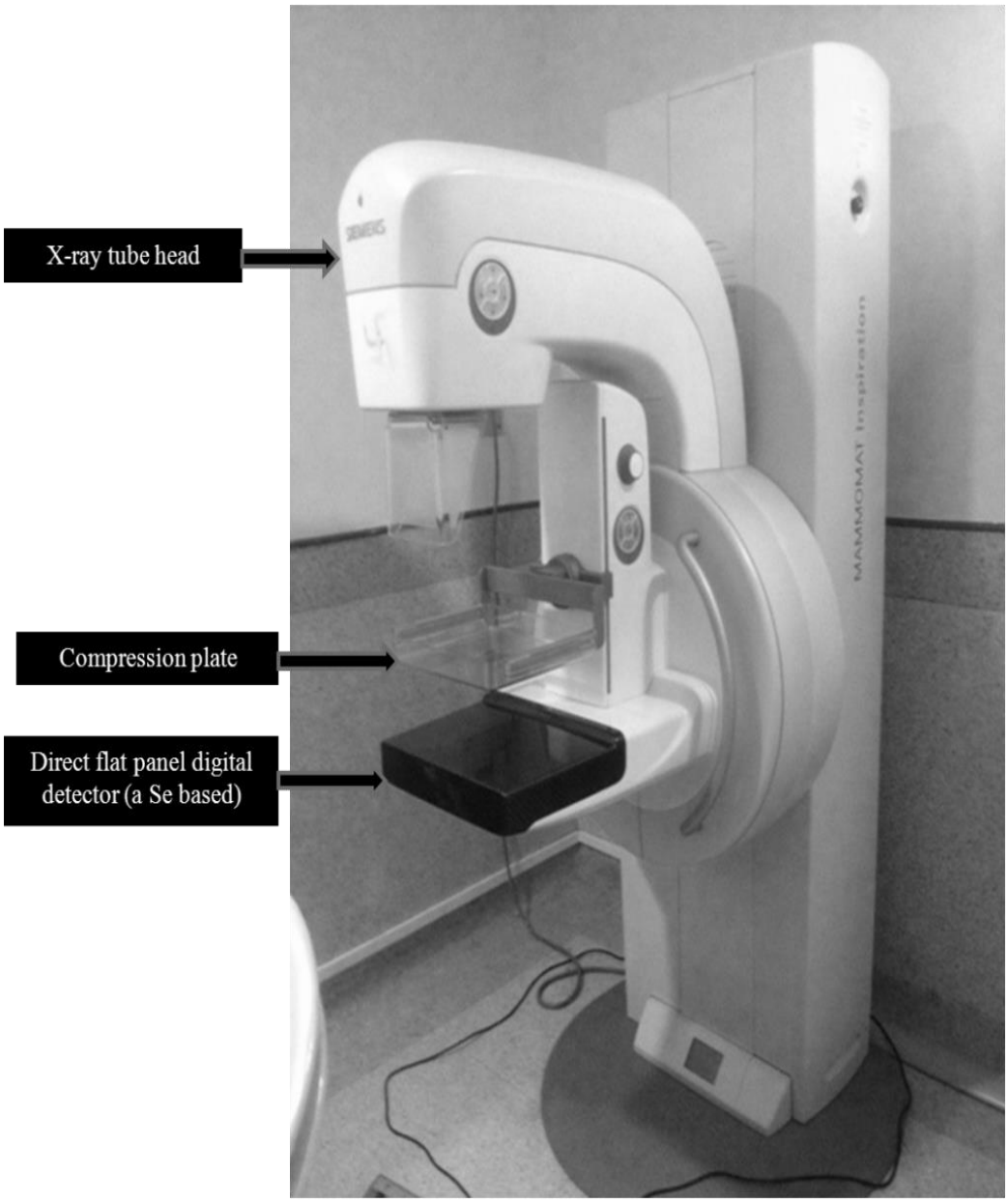

Figure 4.1 Photograph of the digital mammography machine used for carrying out imaging and dosemetric study

CIRS Mammography Research Set 012A

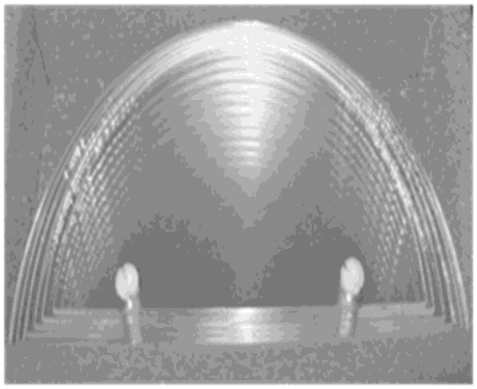

RPAD,BARC made PMMA Mammography Phantom

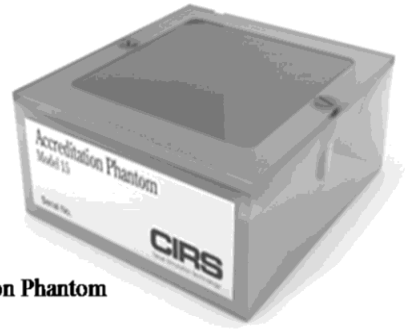

CIRS Accreditation Phantom

Figure 4.2 Photograph of various phantoms used for imaging and dosemetric study of digital mammography system

Physical and dimensional details of these phantoms are given in table 4.1. The relative contents of glandular and adipose tissues of these phantoms are 50/50%, 30/70%, and 20/80% respectively. CIRS research set also includes 10 cm x 12.5 cm photo timer compensation plates with varying thicknesses (0.5 cm to 7 cm) and varying relative contents of glandular and adipose tissues (30/70%, 50/50% and 70/30%).The material used in the CIRS phantoms is epoxy resin which mimics the photon attenuation coefficients of a range of breast tissues. The BARC mammography phantom is made up of PMMA and was used for measuring CNR of the digital mammography system at various thicknesses. The BARC mammography phantom is equivalent to commercially available mammography phantoms and considered to be

suitable for measuring radiation doses in different breast equivalent thicknesses (Sharma et al 2012). Hence it was also used for measuring MGD values at different PMMA thicknesses.

Table 4.1 Physical and dimensional details of different mammography imaging and dosimetry phantoms

Phantom type (glandular/adipose)		**Descriptions**	**Quantity (nos.)**	**Material**
CIRS mammography research set (012A)	CIRS 30/70 Slabs	Slab Dimensions: 10x12.5x0.5 cm^3 Slab Dimensions: 10x12.5x1.0 cm^3 Slab Dimensions: 10x12.5x2.0 cm^3	2 2 2	Epoxy resin
	CIRS 50/50 Slabs	Slab Dimensions: 10x12.5x0.5 cm^3 Slab Dimensions: 10x12.5x1.0 cm^3 Slab Dimensions: 10x12.5x2.0 cm^3	2 2 2	
	CIRS 70/30 Slabs	Slab Dimensions: 10x12.5x0.5 cm^3 Slab Dimensions: 10x12.5x1.0 cm^3 Slab Dimensions: 10x12.5x2.0 cm^3	2 2 2	
	CIRS 10 B	Tissue equivalent mammography phantom, 4 cm thickness having 50% glandular tissue and 50% adipose tissue	1	
	CIRS 10 A	Tissue equivalent mammography phantom, 5 cm thickness having 30% glandular tissue and 70% adipose tissue	1	
	CIRS 10 C	Tissue equivalent mammography phantom, 6 cm thickness having 20% glandular tissue and 80% adipose tissue	1	
CIRS mammography accreditation phantom (015A)		Dimensions: 10.8 x 10.2 x 4.4 cm^3	1	PMMA
BARCPMMA phantom		Semispherical phantom with the length and radius of the central slab of 21 and 10 cm respectively.	1	PMMA
CIRS: Computerized imaging reference systems; BARC: Bhabha Atomic Research Centre; PMMA: Polymethylmethacrylate.				

For contrast detail resolution study of digital mammography machine, CDMAM phantom (CDMAM 3.4) along with automated CDMAM Analyzer software V 1.2 (Artinis medical Systems, The Netherlands) was used (van Engen et al 2013). The phantom is

delivered with set of five PMMA blocks of different thicknesses ranging from 5 mm to 10 mm and physical dimensions of 180 mm x 240 mm as shown in figure 4.3. The CDMAM phantom shown in figure 4.3 consists of a 16 cm x 24 cm x 0.3 mm Aluminum (Al) plate with 205 square cells (arranged in 16 rows x 16 columns) with gold disks of various thicknesses (0.03 µm to 2.00 µm) and diameters (0.06 mm to 2.00 mm). These disks are aligned on a two-dimensional grid where two disks can be found in each cell, one in the center and another in one of the four cell corners. Columns have equal gold disc thickness whereas rows have equal gold disc diameters.

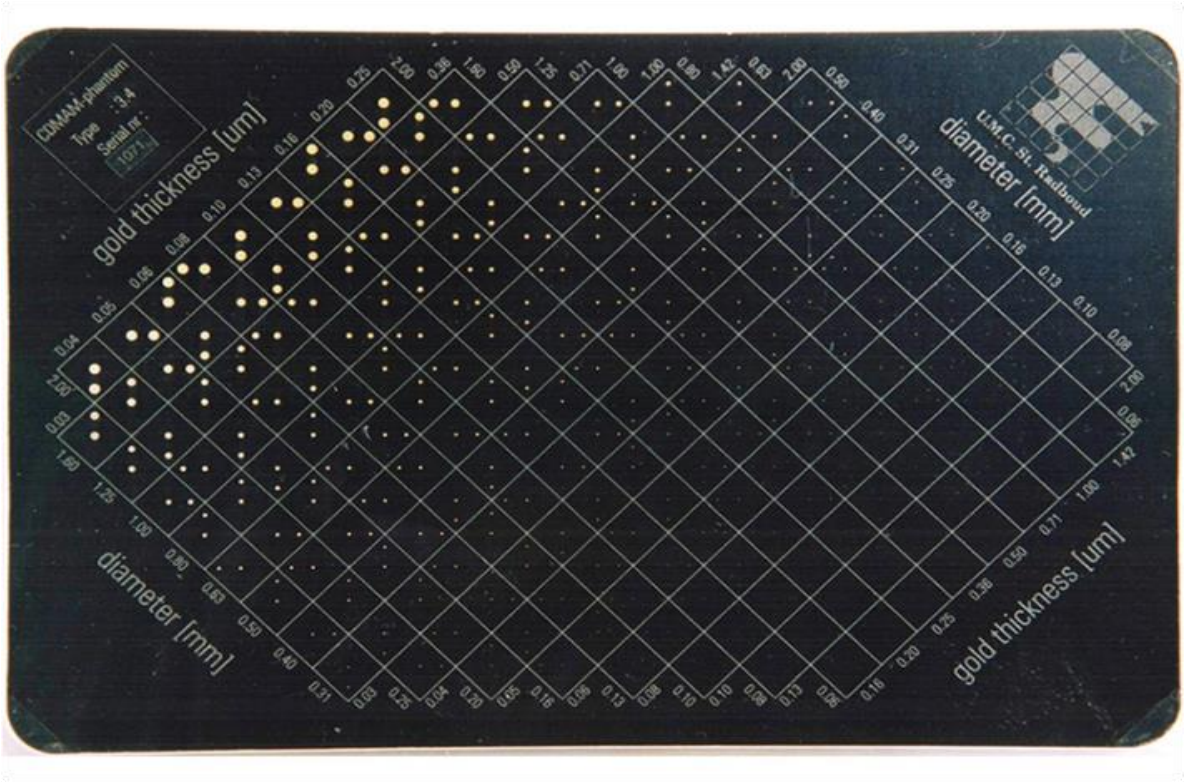

Figure 4.3 Photograph of CDMAM 3.4 phantom used for contrast detail resolution study of digital mammography system

The CDMAM 3.4 phantom was positioned on the bucky of the mammography machine. The structures with the smallest diameter were located closest to the chest wall side of the bucky. PMMA blocks supplied along with CDMAM phantom were used to increase the

total thickness of the phantom. CDMAM Analyzer software was used for computing the contrast detail (CD) curve, the inverse image quality figure (IQF_{inv}) and % detected gold disks, which offers the various functionality test on the exposed CDMAM 3.4 phantom images which should be DICOM (digital imaging and communications in medicine) tagged (van derBurght et al 2010). CDMAM analyzer software offers the possibility to analyze more than one CDMAM image into one result thus reducing the influence of image noise (van Engen et al 2013). For image quality evaluation, smallest thickness of the disks just visible for each diameter, called the threshold contrast was measured using automatic software analyzer and same was plotted in CD curve for the various clinically used operating conditions. The IQF_{inv} numbers were obtained from the analyzed CDMAM phantom images which determines the contrast (thickness) threshold in the image of the object as a function of the detail (diameter) and is calculated using given equation 4.1.

$$IQF_{inv} = \frac{100}{\sum_{i=1}^{16} C_{i,th} * D_i} \qquad (4.1)$$

Where $C_{i,th}$ denotes the threshold thickness in diameter-column i and D_i, denotes the threshold diameter in contrast column i. The contrast is given in 'μm' whereas the diameter is taken in 'mm'. Also % detected disks were obtained from the analyzed CDMAM phantom image which is also used as the image quality indicator. Higher the IQF_{inv} better the low contrast visibility.

4.2.3 Measurements of half value layer (HVL), radiation output, breast entrance exposure (BEE) and mean glandular dose (MGD)

Beam quality (HVL) and radiation output (mGy) measurements at different kVp stations and target/filter combinations were carried out using Raysafe X2 base unit along with

Raysafe X2 MAM sensor (Fluke Biomedical, USA) having measurable dose range of 1 μGy to 99.99 Gy with uncertainty of 5%. All these measurements were performed using manual mode digital mammography machine. Raysafe X2 base unit along with Raysafe X2 MAM sensor was also used for measuring breast entrance exposure (BEE) while exposing different mammography phantoms. During BEE measurement, Raysafe X2 MAM sensor was placed at one side of the phantom and compression plate was used in contact of phantom to simulate clinical exposure conditions as shown in figure 4.4.

The MGD values were calculated from the measured BEEs by applying multiple conversion factors using equation 4.2 (Dance et al 2000, Dance 1990).

$$MGD = K.\ g.\ c.\ s \qquad (4.2)$$

where, K represents the BEE (i.e. incident air kerma) at the upper surface of the breast, g is the incident air kerma to mean glandular dose conversion factor corresponding the glandularity of 50%, c is the correction factor for difference in breast composition from 50% glandularity and s is the correction factor for difference in x-ray spectra. Dance et al. have given g and c values against HVL of the x-ray beams in the tabulated form (Dance et al 2000, Dance 1990). Using these standard tables, data points were plotted and same were used to derive the values of g and c factors corresponding to the HVL values measured for different mammography phantoms for the studied digital mammography system in the present study (Figure 4.5).

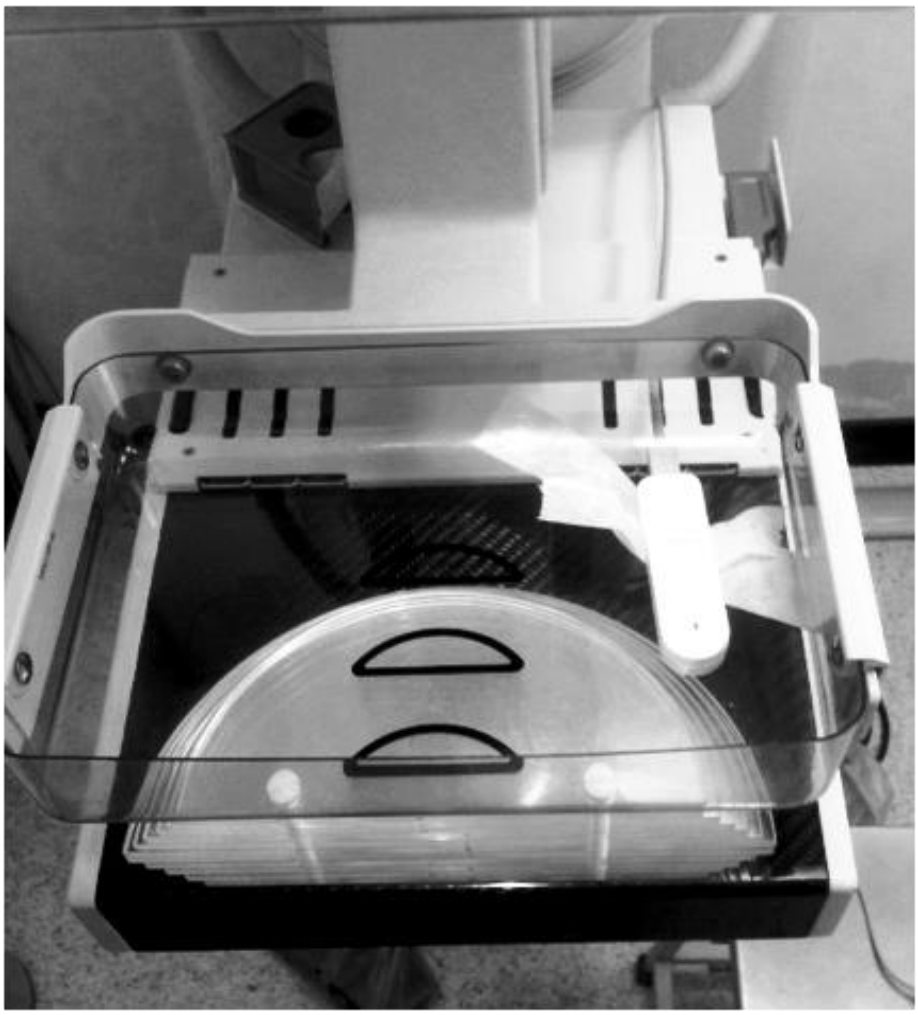

Figure 4.4 Experimental set up for measurement of breast entrance exposure (BEE) in mammography phantom

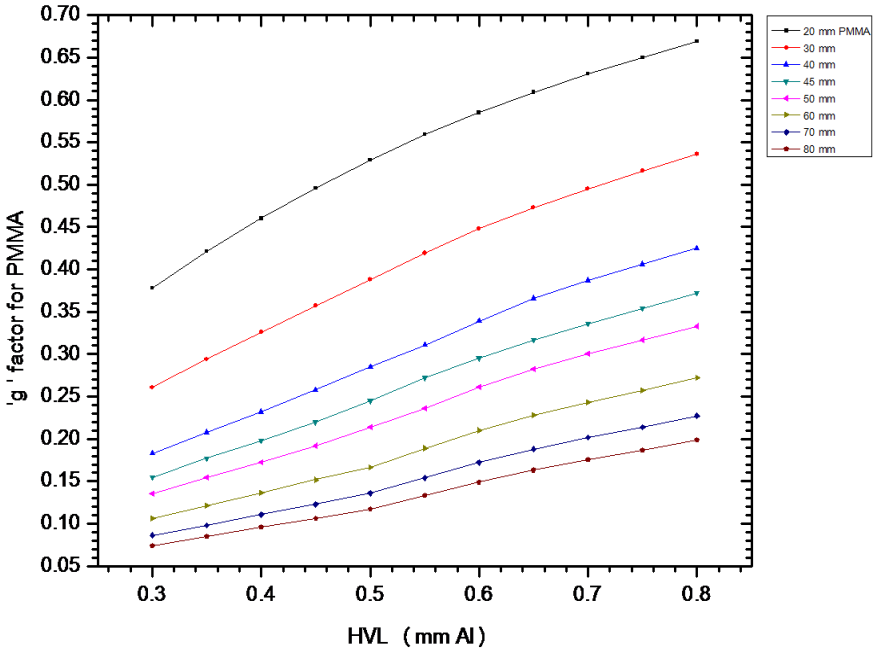
'g ' factor for PMMA
HVL （mm Al）
20 mm PMMA
30 mm
40 mm
45 mm
50 mm
60 mm
70 mm
80 mm

(a)

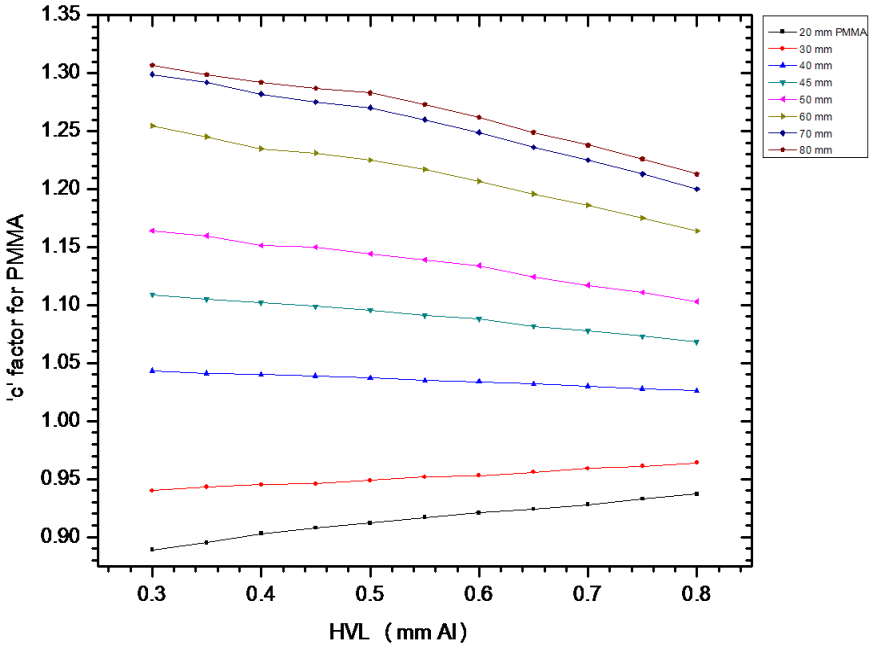
'c' factor for PMMA
HVL （mm Al）
20 mm PMMA
30 mm
40 mm
45 mm
50 mm
60 mm
70 mm
80 mm

(b)

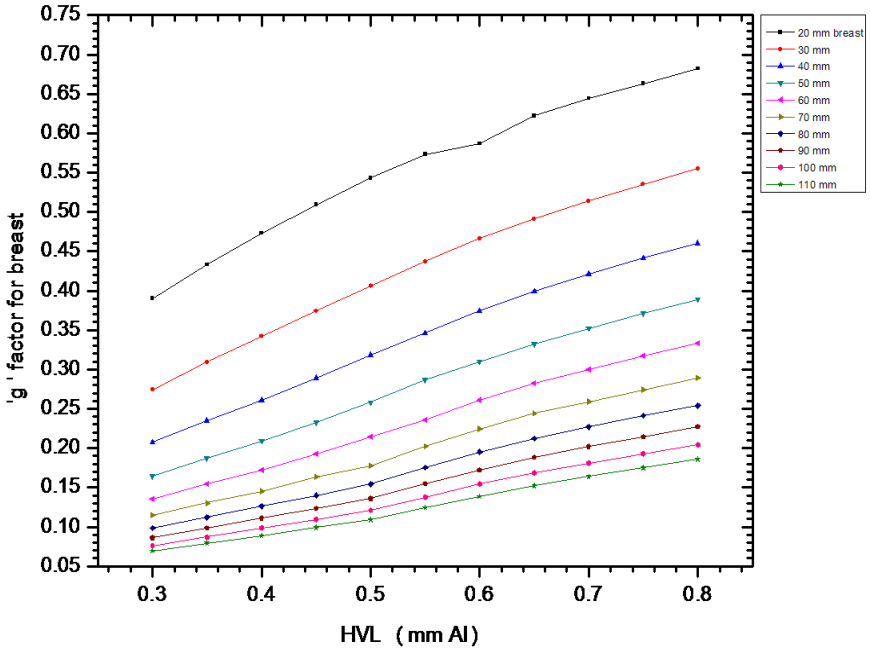
'g ' factor for breast
HVL （mm Al）
20 mm breast
30 mm
40 mm
50 mm
60 mm
70 mm
80 mm
90 mm
100 mm
110 mm

(c)

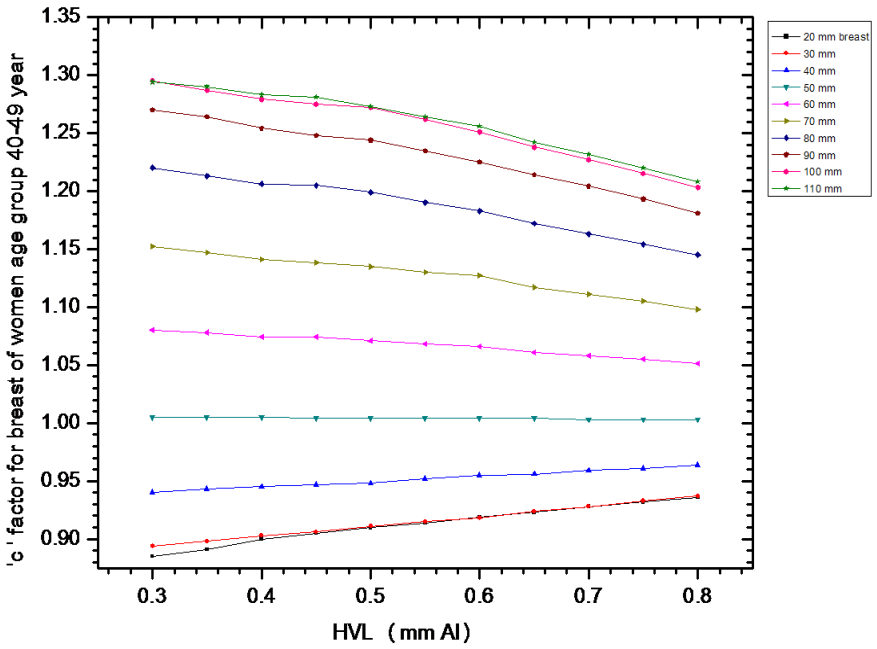
'c ' factor for breast of women age group 40-49 year
HVL （mm Al）
20 mm breast
30 mm
40 mm
50 mm
60 mm
70 mm
80 mm
90 mm
100 mm
110 mm

(d)

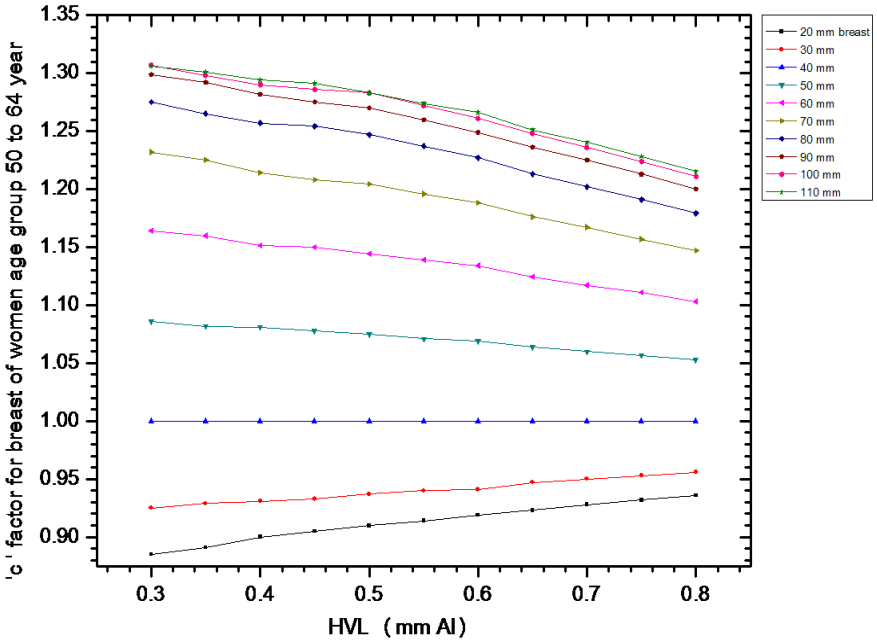

(e)

Figure 4.5 Plot of various conversion factors required to calculate the MGD values from experimentally measured BEE as suggested by Dance et al. (a) g factors in PMMA, (b) c factors in PMMA, (c) g factors to breast, (d) c factors for breasts of women of age group 40-49 years, (e) c factors for breasts of women of age group 50-64 years

4.2.4 Measurement of contrast to noise ratio (CNR)

For CNR measurements, a square plate of aluminium (Al) of dimension 10 mm x 10 mm and thickness 0.2 mm was placed on different thickness of PMMA phantom which ranges from 2 to 8 cm as shown in figure 4.6.While carrying out the CNR measurements, BEE was measured using Raysafe X2 MAM sensor positioned by the side of PMMA phantom of different thicknesses and compression paddle in contact of phantom to derive the actual MGD**.** The images of the different PMMA phantom thicknesses obtained during the dose measurement were analyzed to obtain the CNR values using Image J software (Ferreira and Rasband 2015). A 5 mm × 5 mm square region of interest (ROI)was used to determine the

average signal pixel value (PV_{signal} at location2, Al) and the standard deviation (SD) in the signal within the image of the Al square and the surrounding background (ROI) at location 1 (PMMA) as shown in figure 4.6. The CNR was calculated for each image as defined in the European protocol using the following equation 4.3.

$$CNR = \frac{PV_{Signal} - PV_{Bkg}}{\sqrt{\frac{(SD_{Signal})^2 + (SD_{Bkg})^2}{2}}} \quad (4.3)$$

Where, PV_{signal} is the average pixel value of the signal, PV_{bkg} is the average pixel value of background, SD_{signal} is the standard deviation (SD) in the signal area 2, and SD_{bkg} is the standard deviations in the background area 1.

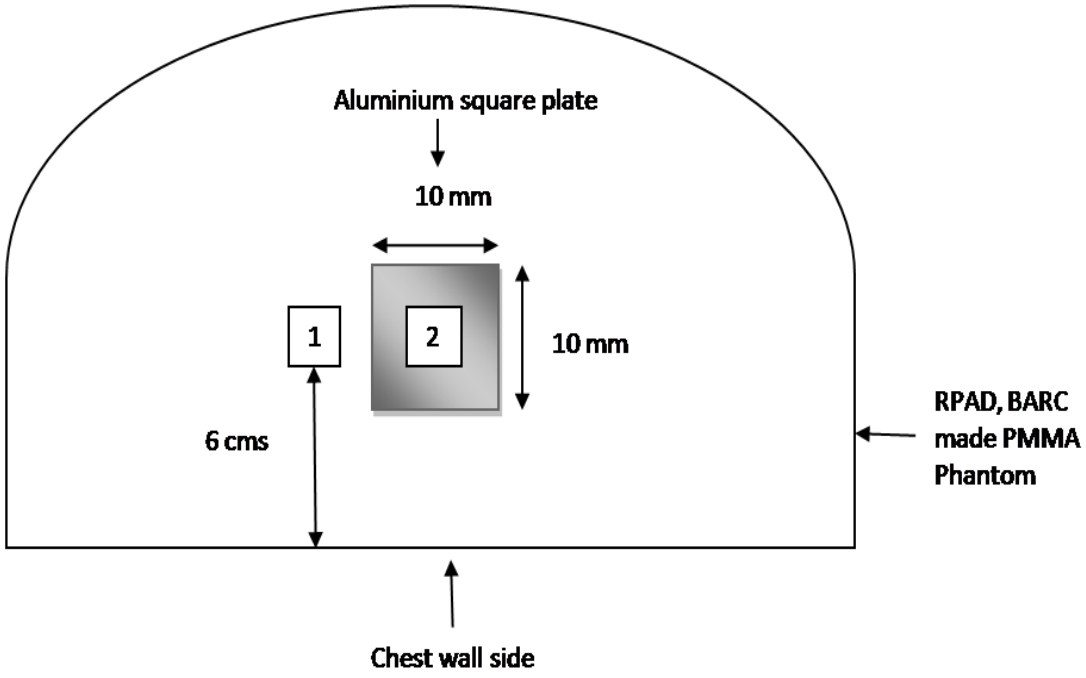

Figure 4.6 Set up for contrast to noise ratio (CNR) measurement with different BARC PMMA phantom thicknesses

4.2.5 Measurement of figure of merit (FOM)

FOM for the digital mammography system was evaluated using the measured CNR values and corresponding MGDs in BARC mammography PMMA phantom. Equation 4.4 was used for all the FOM calculation.

$$\mathrm{FOM} = \frac{\mathrm{CNR}^2}{\mathrm{MGD}} \tag{4.4}$$

Also percentage change (%) was calculated in terms of increased or decreased value for the three measured parameters called CNR, MGD and FOM using the formula given by equation 4.5.

$$Percentagechange\ (\%) = \frac{[Reference_{value} - Observed_{value}]}{Reference_{value}} * 100 \tag{4.5}$$

4.2.6 Measurements of modulation transfer function (MTF) and noise power spectrum (NPS)

Modulation transfer function (MTF) of the digital mammography system was measured using a slanted radio-opaque edge placed at the detector input plane with grid in position (Samei and Flynn 2003, Samei et al 2005, Perry et al 2013). Image of the exposed radio-opaque plate (Figure 4.7). Radio-opaque plate was made up of tantalum having sharp and straight edge with dimensions 10 cm X 10 cm and thickness of 100 μm.

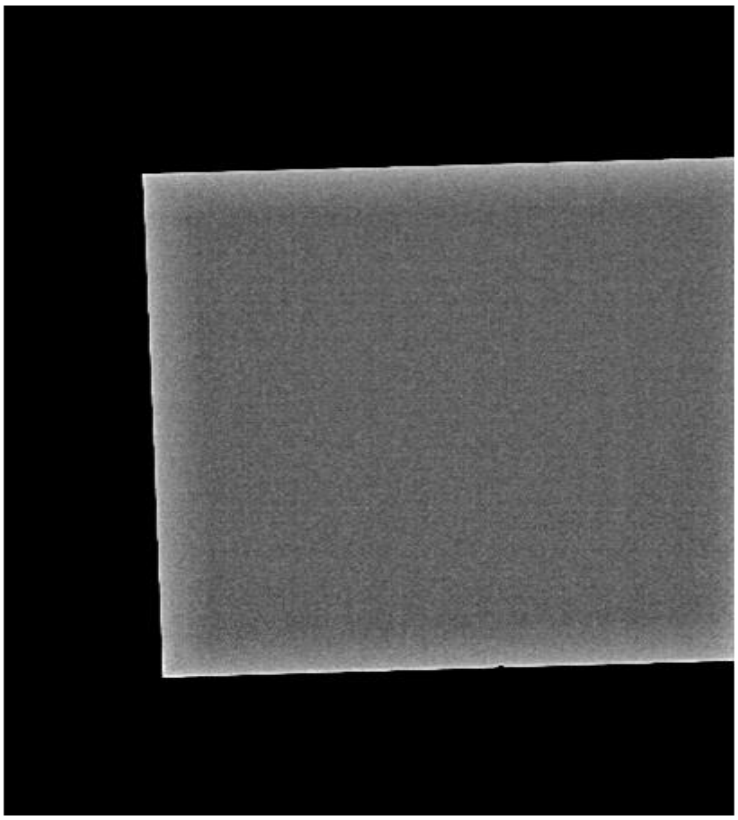

Figure 4.7 Image of exposed radioopaque tantalum plate used for modulation transfer function (MTF) measurement

The edge spread function (ESF) was obtained using Image J software from the image of tantalum plate. Derivative of the ESF was calculated to generate line spread function (LSF) as given by the following equation.

$$\text{LSF (X)} = \frac{d}{dx}\text{ESF}\ (x) \qquad (4.6)$$

The pre-sampled MTF was obtained from the LSF using Fast Fourier Transform (FFT) and by calculating the magnitude as given by the following equation.

$$\text{MTF} = |\text{FFT}[\text{LSF}(x)]| \qquad (4.7)$$

NPS of the digital mammography system was calculated from a series of flat-field images acquired at radiation dose of ~100 μ Gy using the following equation (Perry et al

2013, (Williams et al 1999, Borasi et al 2003, Salvagnini et al 2013, Padgett and Kotre 2005, Siewerdsen et al 2002, Marshall 2007, Ranger et al 2005).

$$NPS(u,v) = \frac{\Delta X \, \Delta y}{M \cdot 256 \cdot 256} \sum_{m=1}^{M} \left| \sum_{i=1}^{256} \sum_{j=1}^{256} \left(I(x_i, y_j) - S(x,y) \right) e^{-2\pi i (u_n x_i + v_k y_j)} \right|^2 \quad (4.8)$$

Where an ROI dimension of 256 x 256 pixels has been used. M is the number of ROIs, $\triangle x$ is the pixel spacing in the x direction, $\triangle y$ is the pixel spacing in the y direction, I (x,y) are the pixel value data, S (x, y) is a 2-dimensional polynomial function used to the entire extracted region used of NPS analysis.

4.3 Results and discussion

For the studied digital mammography machine, measured HVL values for the different T/F combinations are shown in figure 4.8. Before measuring HVL values, accuracy of all the kVp stations and different T/F combinations were evaluated which were found to be <± 1kVp. At Mo/Mo set up, the measured HVL range was found to be 0.294±1E-3 to 0.357 ± 1E-3 for the applied kVp of 23, 25 and 28. At Mo/Rh set up, HVL range was found to be 0.43±0.002 to 0.473 ± 1E-3 for the applied kVp of 28, 32 and 34. At W/Rh set up, HVL range was found to be 0.56 ±0.002 to 0.62±0.002 for the applied kVp of 28, 32, 34 and 35 kVp.

Results of radiation output (mGy) measured at different T/F combinations for the various kVp stations are shown in figure 4.9. Radiation output consistency at all kVp stations and different T/F combinations was calculated in terms of coefficient of variation (COV) and was found to be less than 0.05.For Mo/Mo, T/F the radiation output was found to be in the range of 1.16-2.15 mGy at 23, 25 and 28 kVp. For Mo/Rh, measured radiation output range was observed to be 1.62-2.84 mGy at 28, 32 and 34 kVp and for W/Rh it was found to be 0.639-1.04 mGy at 28, 32, 34 and 35 kVp.

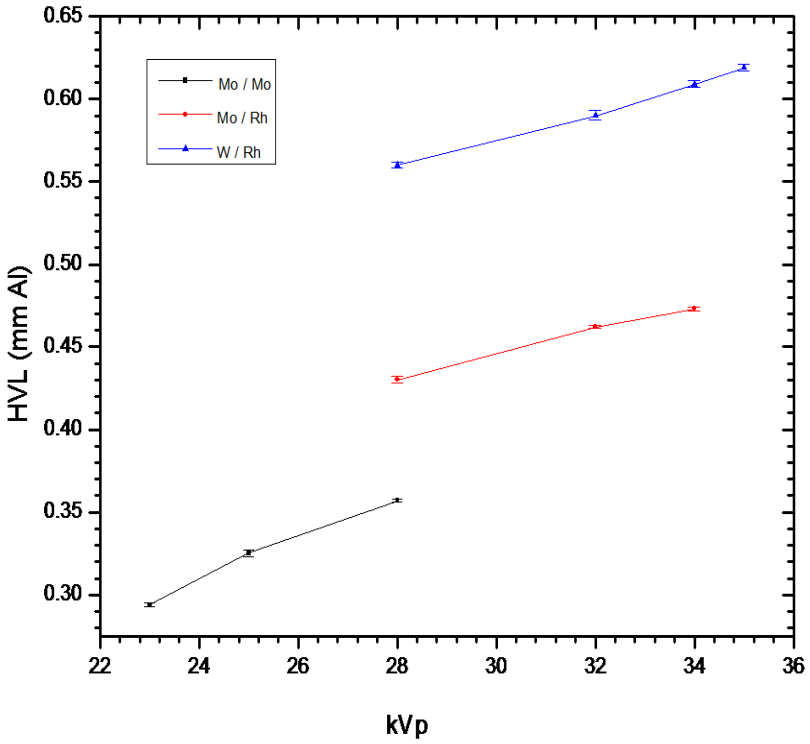

Figure 4.8 Measured HVL values (mm of Al) at different kVp settings for the various target/filter combinations (Mo/Mo, Mo/Rh, W/Rh)

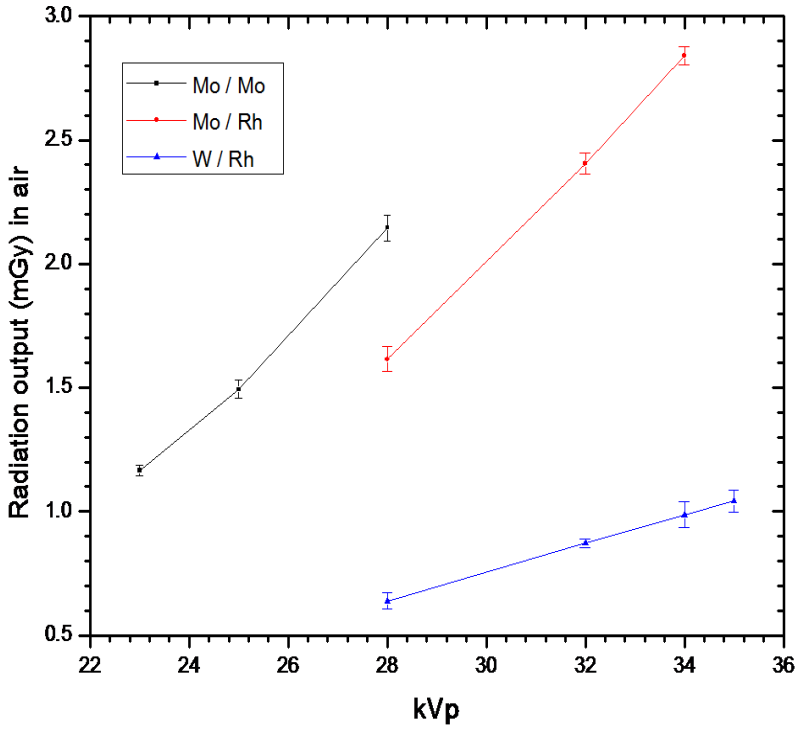

Figure 4.9 Measured radiation output (mGy) in air at different kVp settings for the various target/filter combinations (Mo/Mo, Mo/Rh, W/Rh)

Figure 4.10 shows the FOM values in terms of CNR^2/MGD for the 4.5 cm thick BARC PMMA phantom exposed under AEC mode at three different T/F combinations. CNR values for the BARC PMMA phantom with total thickness of 4.5 cms were found to be 6.71, 6.17 and 5.27 with MGD values of 3.0, 2.4 and 1.4 mGy at T/F of Mo/Mo, Mo/Rh and W/Rh respectively. These measured CNR values are found to be within the European limiting CNR values. [5, 10] Corresponding calculated FOM values were 15.02, 15.88 and 19.82 for these three T/F combinations respectively. Percentage decreases in MGD values were found to be 20 and 53.33% when T/F was changed from Mo/Mo to Mo/Rh and W/Rh respectively. Also for comparing two clinical operating mode i.e. AEC (T/F=W/Rh) and OPDOSE (T/F=W/Rh), % change in MGD, CNR and FOM for the 4.5 cm BARC PMMA phantom were calculated. It

is seen from the compared values that percentage increase of 21.43 was found in MGD value for the AEC than OPDOSE mode. Whereas in CNR values, % increase of 31.5 was observed for OPDOSE than AEC mode. Also % increase of 40.46 was found in FOM value for the AEC than the OPDOSE mode at same T/F combination. Hence it is concluded that for the 4.5 cm thick PMMA phantom, AEC mode provides the better image quality and dose performance.

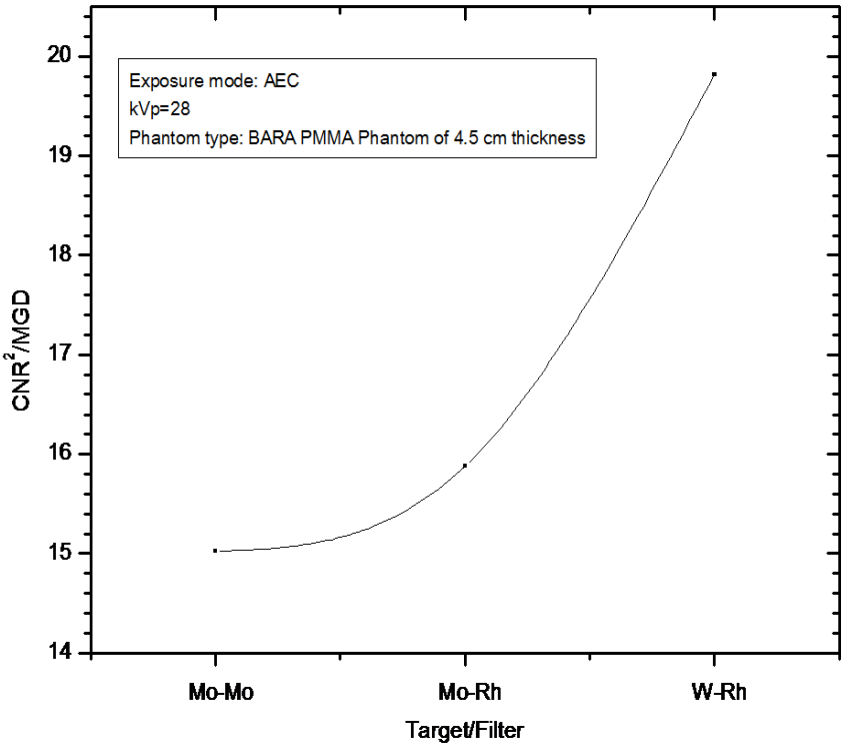

Figure 4.10 Plot for calculated figure of merit (FOM) in terms of CNR^2/MGD values for the BARC PMMA phantom with thickness of 4.5 cms and exposed under AEC mode

Calculated FOM values for BARC PMMA phantom of different thicknesses, exposed under OPDOSE mode are shown in figure 4.11. It was observed that highest CNR and lowest CNR values were found for the 2 and 8 cm thick BARC PMMA at lowest MGD and highest

MGD respectively. Correspondingly highest FOM values were achieved for 2 cm and lowest for 8 cm thick BARC PMMA phantom. Outcome of this analysis suggests that when the breast thicknesses are small, delectability of any mass or microcalcification will be higher due to higher CNR value observed at lower thickness.

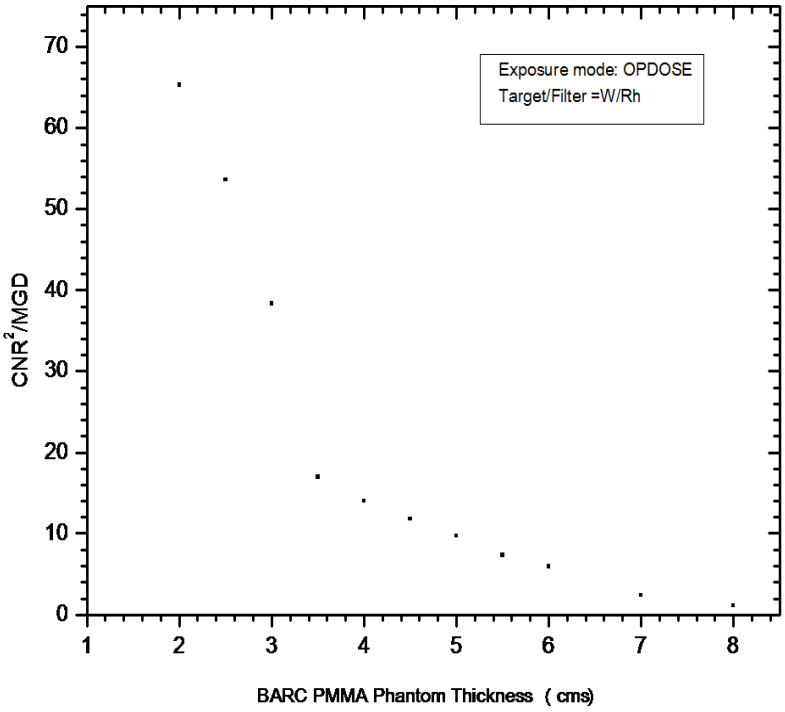

Figure 4.11 Plot for calculated figure of merit (FOM) in terms of CNR^2/MGD values for the BARC PMMA phantom having different thicknesses and exposed under clinically used OPDOSE mode

Calculated MGD values for digital mammography system for different breast tissue simulating phantoms and for different BARC PMMA phantom thickness are given in tables 4.2 and 4.3 respectively. It incorporates the displayed compressed breast thickness (CBT) in cm, machine selected parameters such as T/F combination, applied kVp, mAs, and MGDs. It also include the values of other parameters measured by dosimeter X2 MAM e.g. BEE, HVL,

exposure time and exposure rate. MGD ratio between machine displayed and calculated MGD values using the appropriate conversion factors are also given in table 4.2 and 4.3. Outcome of the study also show that for the CIRS slabs phantom of different glandular/adipose tissue compositions and physical thickness of 7.0 cms, the calculated maximum MGD value were found to be of 3.03 for 70/30, 2.32 for 50/50 and 1.75 mGy for the 30/70 glandular/adipose tissue compositions. Also fitting equation was achieved for the calculated MGD values at different thicknesses of BARC PMMA phantom. The variation of MGD with BARC PMMA phantom thickness can be represented by the following second order polynomial fit equation 4.9.

$$MGD\ (mGy) = 0.83 + B_1 * x + B_2 * x^2 \qquad (4.9)$$

Where 'x' represents the thickness of BARC PMAA phantom in centimeter. In equation 4.9, 0.83±0.09 represents the intercept value with associated standard error of 0.09; B_1 has the value of -0.27±0.04 and B_2 has the value of +0.072±0.004. Adjusted R-squared value for the fitted data points is found to be 0.99. Establishing this fitted equation will be helpful in deriving the MGDs directly for any value of PMMA thicknesses rather calculating it using measured BEE and conversion factors.

Table 4.2 Measured MGD values under clinically operated OPDOSE mode (T/F= W/Rh) for digital mammography system using different breast tissue simulating mammography phantoms

Numbers assigned to phantom types	Phantom type (glandular/ adipose)	Quoted physical thickness (cms)	Machine displayed parameters					Dosimeter X2 MAM readings				Measured MGD (mGy)	MGD Ratio (Machine displayed Vs measured)
			T/F	CBT (cms)	kVp	mAs	MGD (mGy)	BEE (mGy)	HVL (mm Al)	Exposure time (sec)	Exposure rate (mGy/sec)		
1	Slabs of CIRS (30/70)	7.0	W/Rh	6.7	30	182.2	1.9	8.53	0.538	2.229	3.825	1.75	1.09
2	Slabs of CIRS (50/50)	7.0	W/Rh	6.7	30	238.6	2.5	11.19	0.54	2.876	3.890	2.32	1.08
3	Slabs of CIRS (70/30)	7.0	W/Rh	6.8	30	311.5	3.3	14.6	0.54	3.360	4.358	3.03	1.09
4	CIRS 10 C	6.0	W/Rh	5.7	29	113.8	1.2	4.67	0.541	1.588	2.941	1.13	1.06
5	CIRS 10 A	5.0	W/Rh	4.7	28	90.4	1.0	3.29	0.537	1.429	2.299	0.96	1.05
6	CIRS 10 B	4.0	W/Rh	3.8	27	75.4	0.9	2.46	0.517	1.426	1.727	0.69	1.30
7	CIRS 015	4.4	W/Rh	4.2	28	81.4	1.2	2.91	0.532	1.417	2.056	1.02	1.18
8	BARC PMMA	6.0	W/Rh	5.9	29	181	2.1	7.15	0.552	2.241	3.193	1.41	1.49
9	BARC PMMA	4.5	W/Rh	4.1	28	93.3	1.2	3.35	0.521	1.443	2.322	0.89	1.34

CIRS, Computerized imaging reference systems; BARC, Bhabha Atomic Research Centre; PMMA, Polymethylmethacrylate; T/F, Target/Filter; CBT, Compressed breast thickness; kVp, kilovoltage peak; mAs, milliampere second; MGD, Mean glandular dose; BEE, Breast entrance exposure; HVL, Half value layer; mGy, milli Gray; cms, centimeters; mm Al, millimeter aluminium

Table 4.3 Measured MGD values under clinically operated OPDOSE mode (T/F= W/Rh) for digital mammography system using BARC PMMA phantom of different thicknesses

BARC PMMA mammography phantom thickness (cms)	**Machine displayed parameters**			**Dosimeter X2 MAM readings**				**Measured MGD (mGy)**	**MGD Ratio (Machine displayed Vs measured)**	**Acceptable level of dose limits in European guidelines (mGy)**
	kVp	**mAs**	**MGD (mGy)**	**BEE (mGy)**	**HVL (mm Al)**	**Exposure time (sec)**	**Exposure rate (mGy/sec)**			
2.0	24	50.7	0.7	1.01	0.490	1.450	0.699	0.57	1.24	< 1.0
2.5	26	45.4	0.7	1.21	0.523	1.441	0.842	0.60	1.16	-
3.0	26	58.9	0.8	1.58	0.525	1.462	1.084	0.70	1.15	< 1.5
3.5	27	66.9	0.9	2.04	0.535	1.471	1.385	0.81	1.12	-
4.0	27	87.2	1.1	2.71	0.532	1.446	1.875	0.95	1.16	< 2.0
4.5	28	98.8	1.3	3.43	0.542	1.502	2.287	1.10	1.18	< 2.5
5.0	28	126.8	1.5	4.47	0.543	1.900	2.352	1.31	1.14	< 3.0
5.5	29	143.4	1.8	5.59	0.551	2.064	2.711	1.50	1.20	-
6.0	29	181.0	2.1	7.15	0.552	2.241	3.193	1.77	1.19	< 4.5
7.0	30	268.9	2.9	11.97	0.557	3.118	3.840	2.58	1.12	< 6.5
8.0	31	352.6	3.7	17.59	0.560	3.905	4.505	3.32	1.12	-

BARC, Bhabha Atomic Research Centre; PMMA, Polymethylmethacrylate; kVp, kilovoltage peak; mAs, milliampere second; MGD, Mean glandular dose; BEE, Breast entrance exposure; HVL, Half value layer; mGy, milli Gray; cms, centimeters; mm Al, millimeter aluminium

Results of the contrast detail resolution study carried out on digital mammography system are shown in figure 4.12 and 4.13 under different clinical exposure conditions. Figure 4.12 shows the contrast detail curve for the CDMAM phantom kept on top of the 4.5 cm PMMA sheets and exposed under AEC mode at different T/F combinations Table 4.4 gives the detail of image quality parameters analyzed in terms of IQF_{inv} and % detected gold disks from the software generated CD curves (Figure 4.14) along with machine selected and displayed parameters. Figure 4.13 shows the contrast detail curve plotted for the CDMAM phantom in combination with PMMA sheets of various thicknesses to simulate clinical breast thicknesses in digital mammography. For different exposure conditions under which CDMAM phantom was exposed to simulate the clinical environment, the measured IQF_{inv} numbers and % detected gold disks which are taken from the software generated CD curves (Figure 4.15) are presented in table 4.5 along with machine selected and displayed parameters.

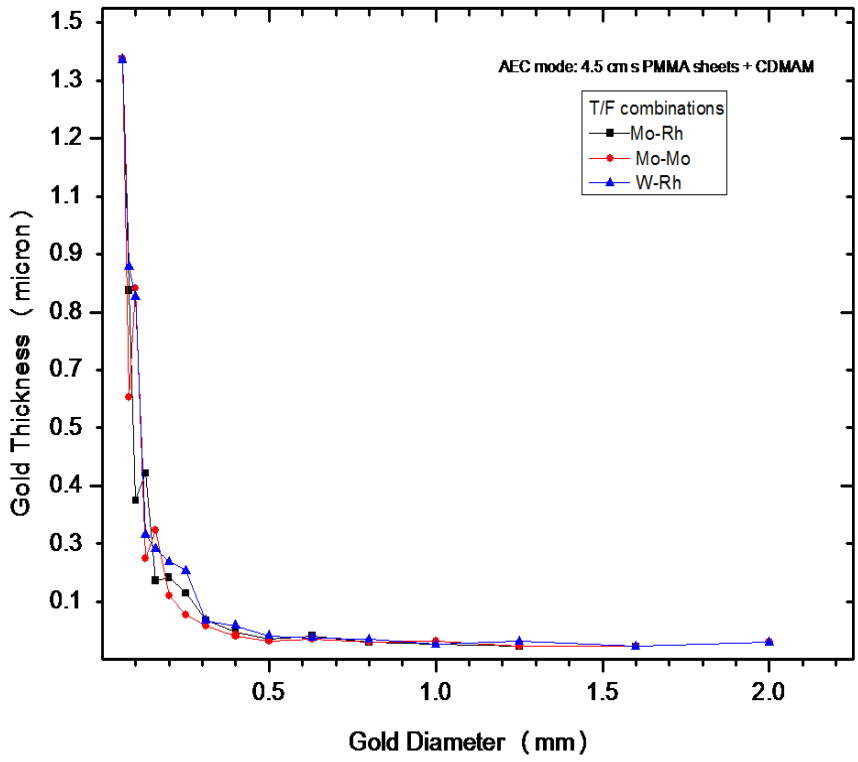

Figure 4.12 Plot of contrast detail performance for the digital mammography machine using CDMAM phantom kept on top of 4.5 cms PMMA sheets and exposed under AEC mode at different target/filter conditions (Mo/Mo, Mo/Rh, W/Rh)

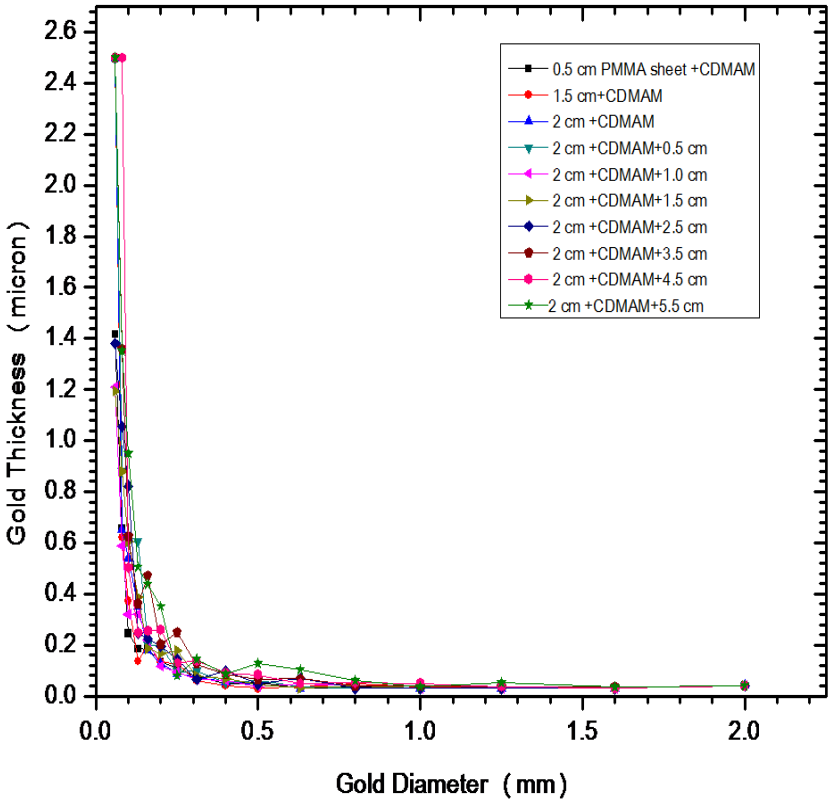

Figure 4.13 Plot of contrast detail performance for the digital mammography machine using CDMAM phantom exposed in combination with PMMA sheets of various thickness to simulate clinical operating conditions under OPDOSE mode

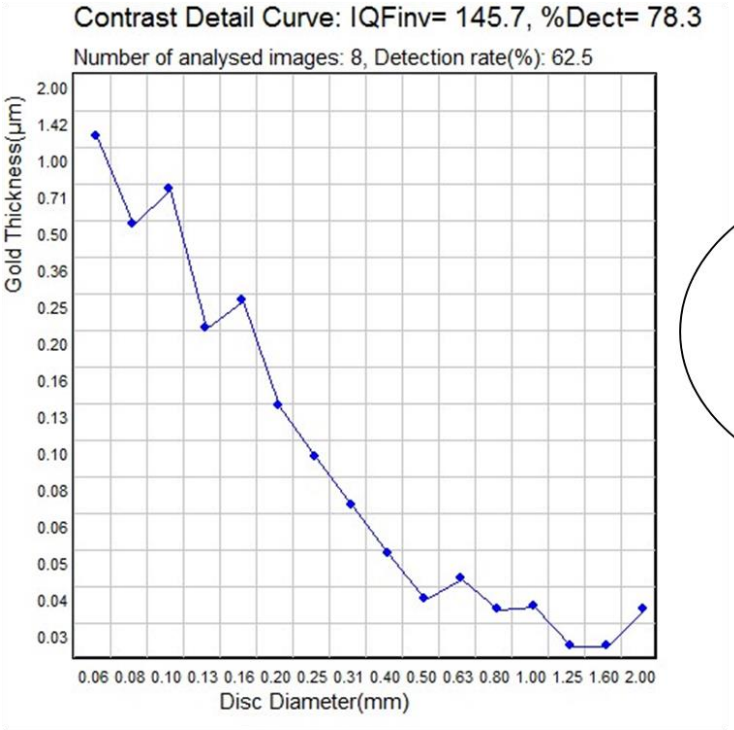

(Target/Filter = Mo/Mo)

4.5 cm PMMA
+
CDMAM phantom

(a)

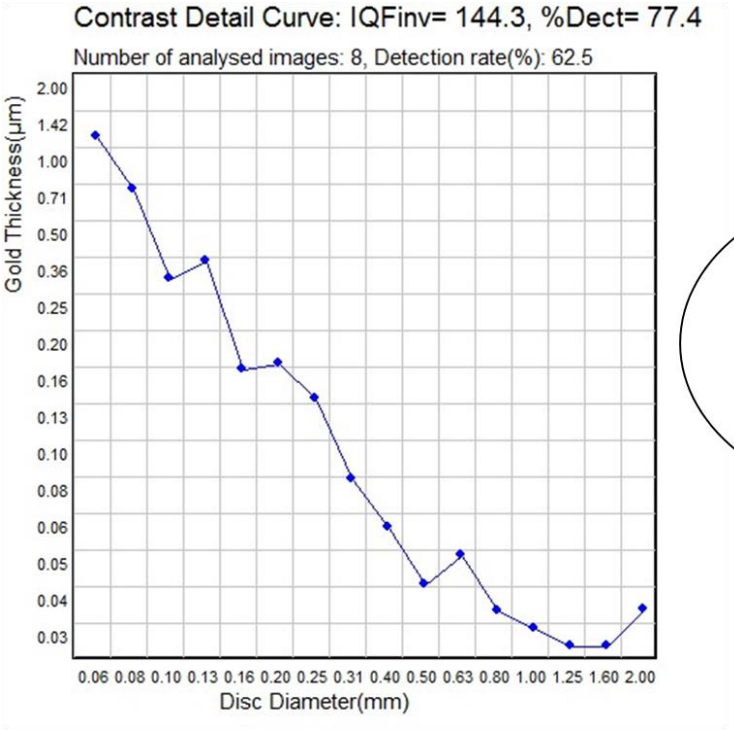

(Target/Filter = Mo/Rh)

4.5 cm PMMA
+
CDMAM phantom

(b)

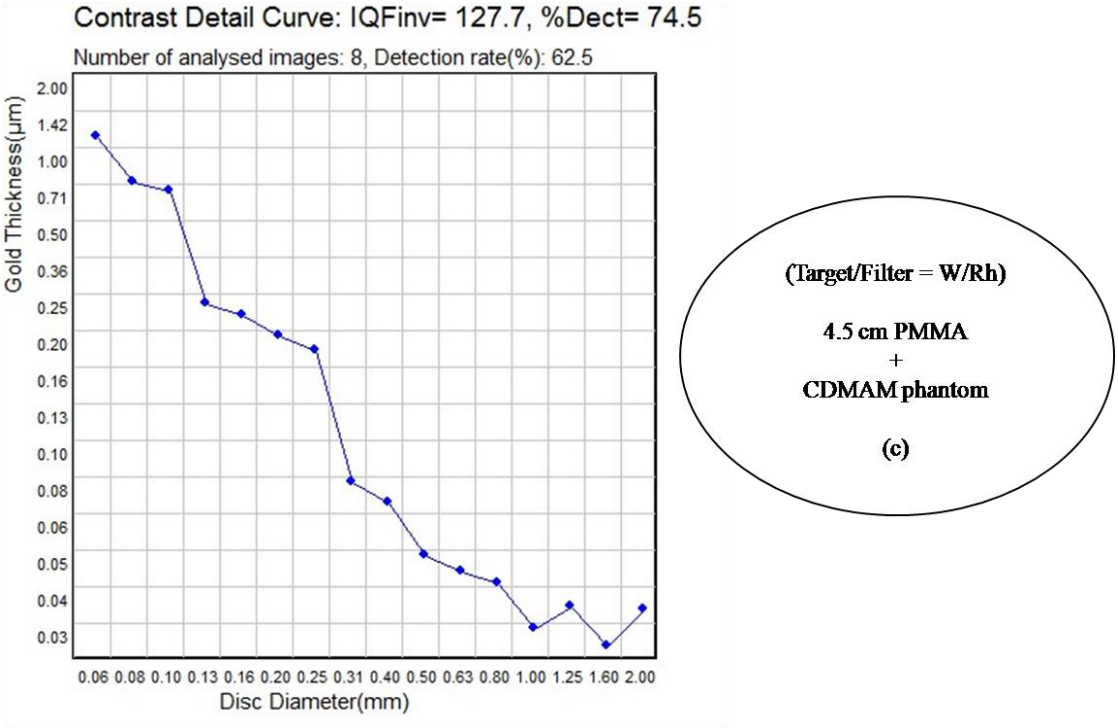

Figure 4.14 Software generated contrast detail curves for the CDMAM phantom kept on top of 4.5 cms PMMA sheets and exposed under AEC mode at different target/filter conditions (a) Mo/Mo (b) Mo/Rh (c) W/Rh

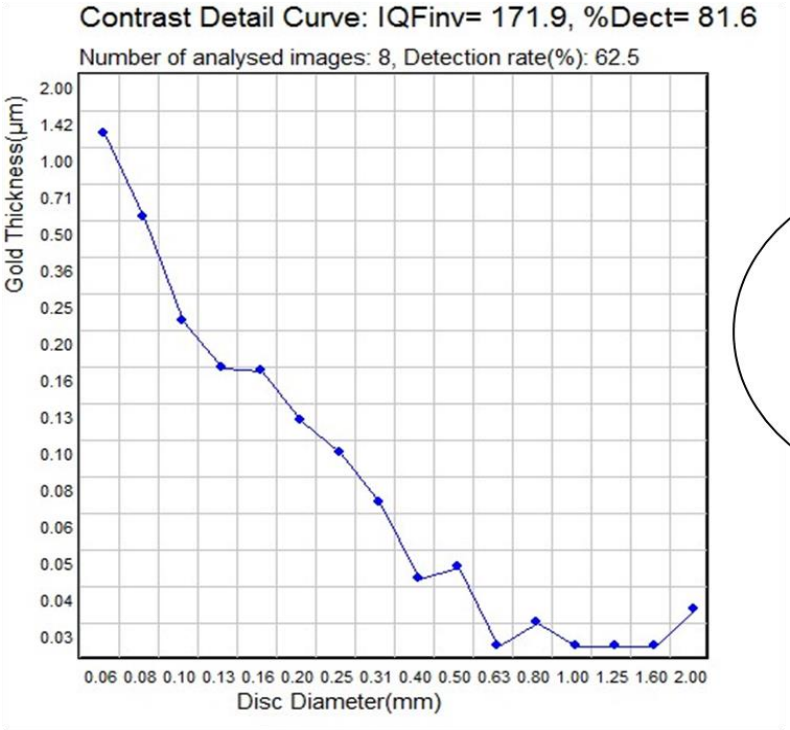

0.5 cm PMMA
+
CDMAM phantom

(a)

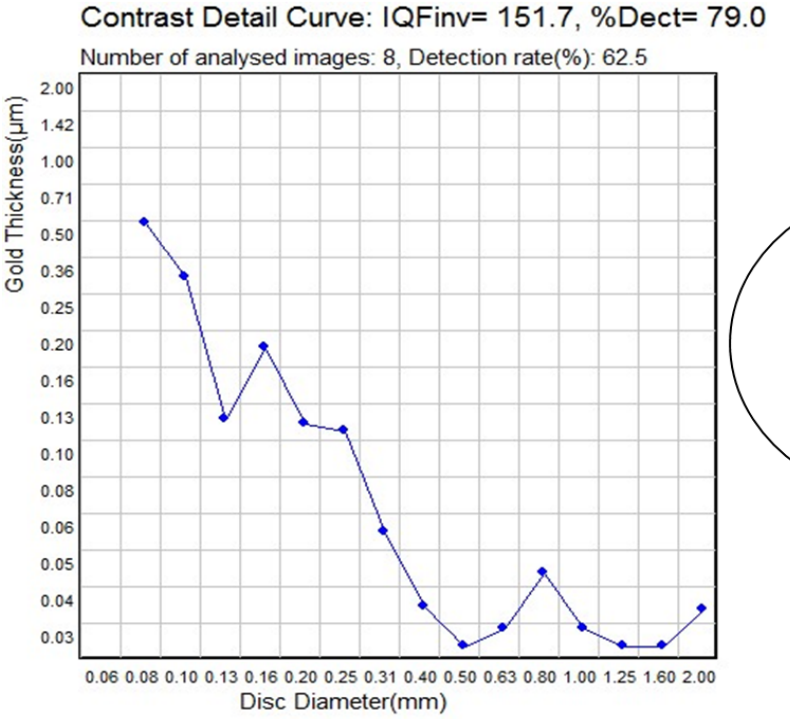

1.5 cm PMMA
+
CDMAM phantom

(b)

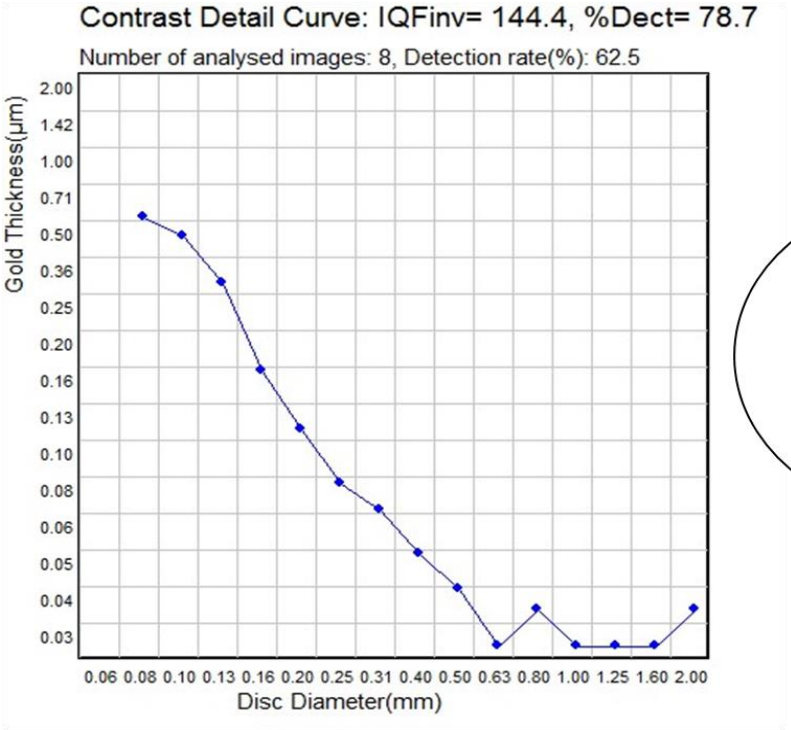

2.0 cm PMMA
+
CDMAM phantom

(c)

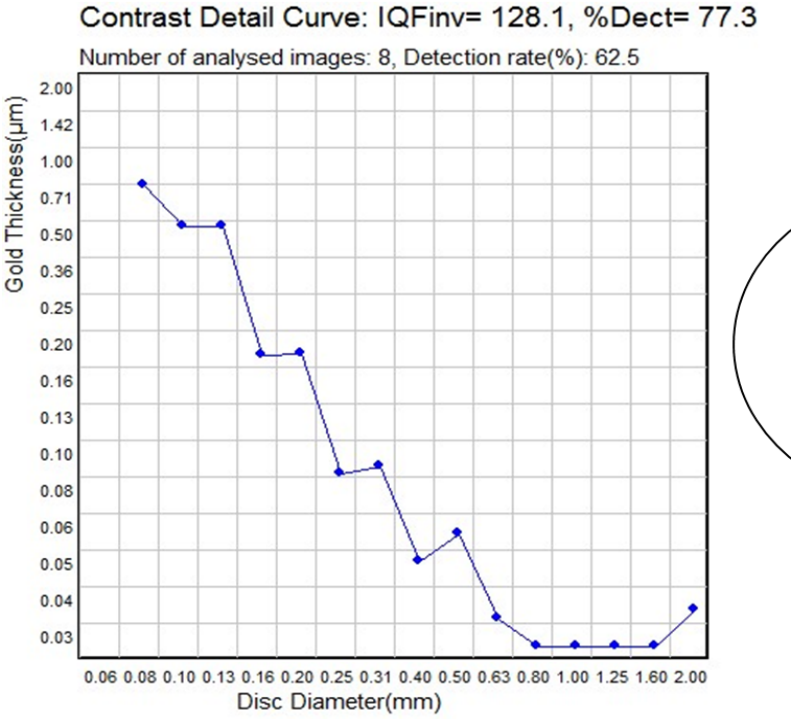

2.0 cm PMMA
+
CDMAM phantom
+
0.5 cm PMMA

(d)

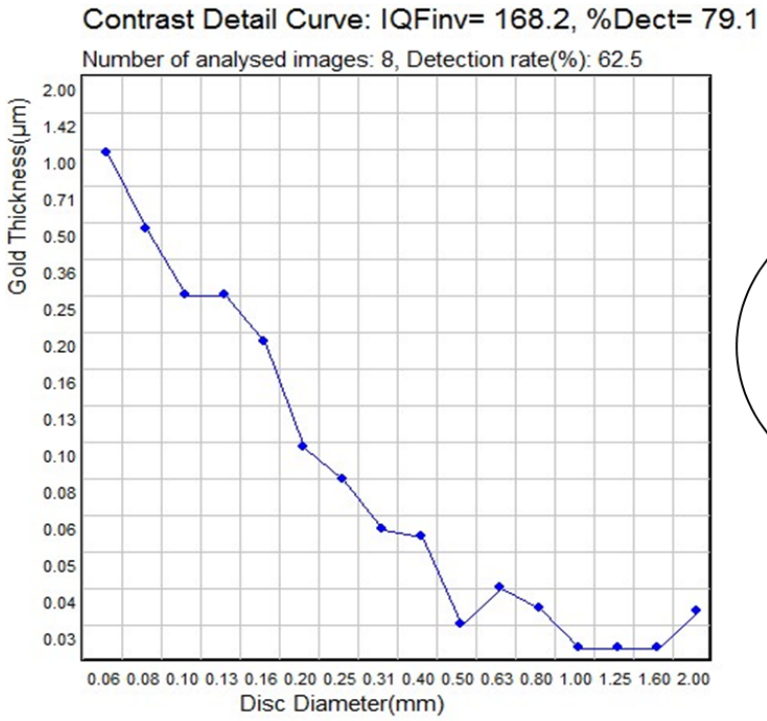

2.0 cm PMMA
+
CDMAM phantom
+
1.0 cm PMMA

(e)

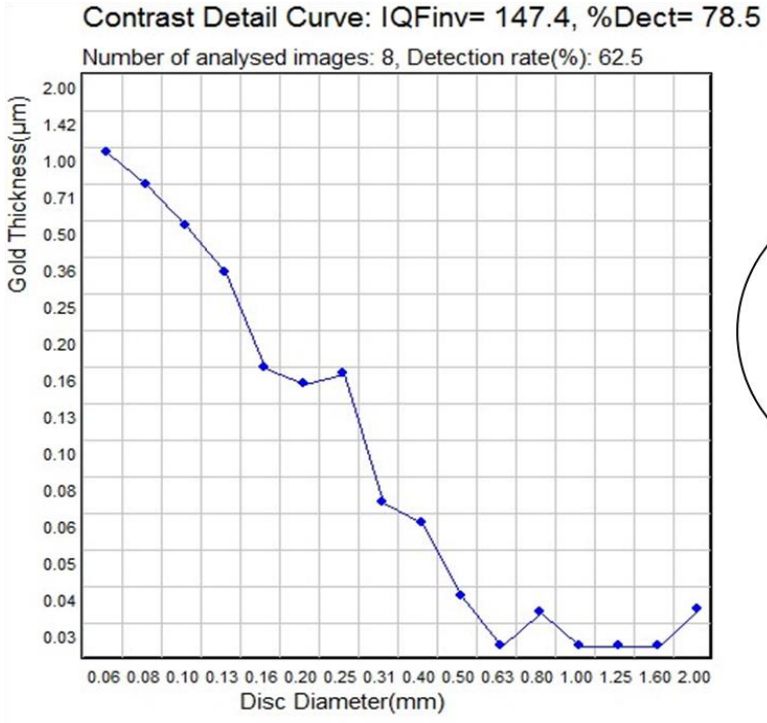

2.0 cm PMMA
+
CDMAM phantom
+
1.5 cm PMMA

(f)

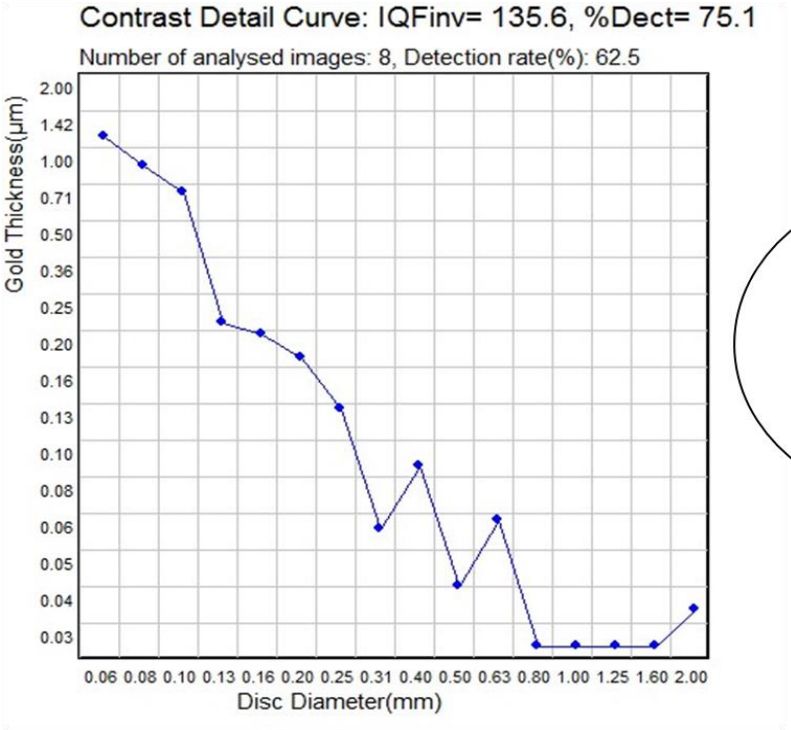

2.0 cm PMMA
+
CDMAM phantom
+
2.5 cm PMMA

(g)

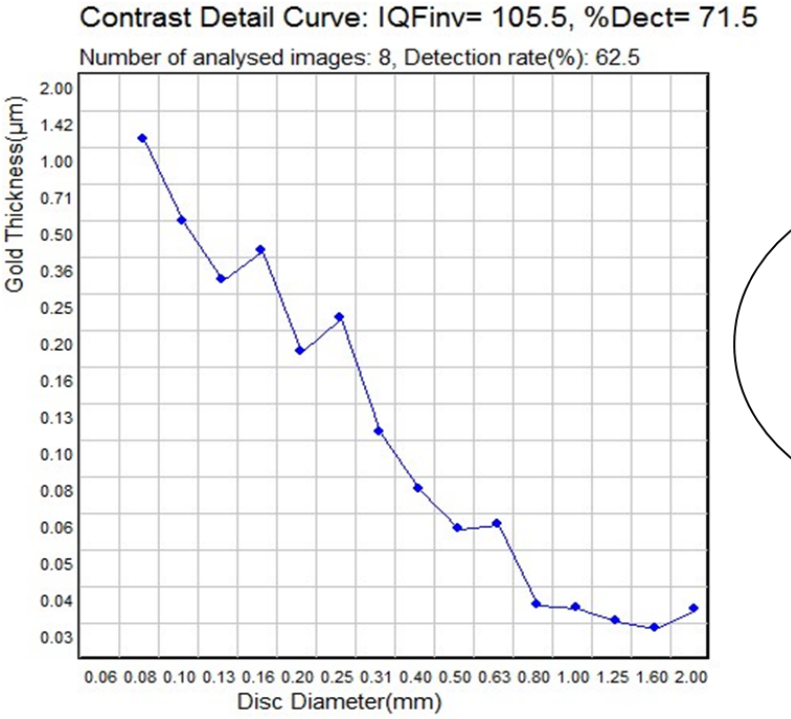

2.0 cm PMMA
+
CDMAM phantom
+
3.5 cm PMMA

(h)

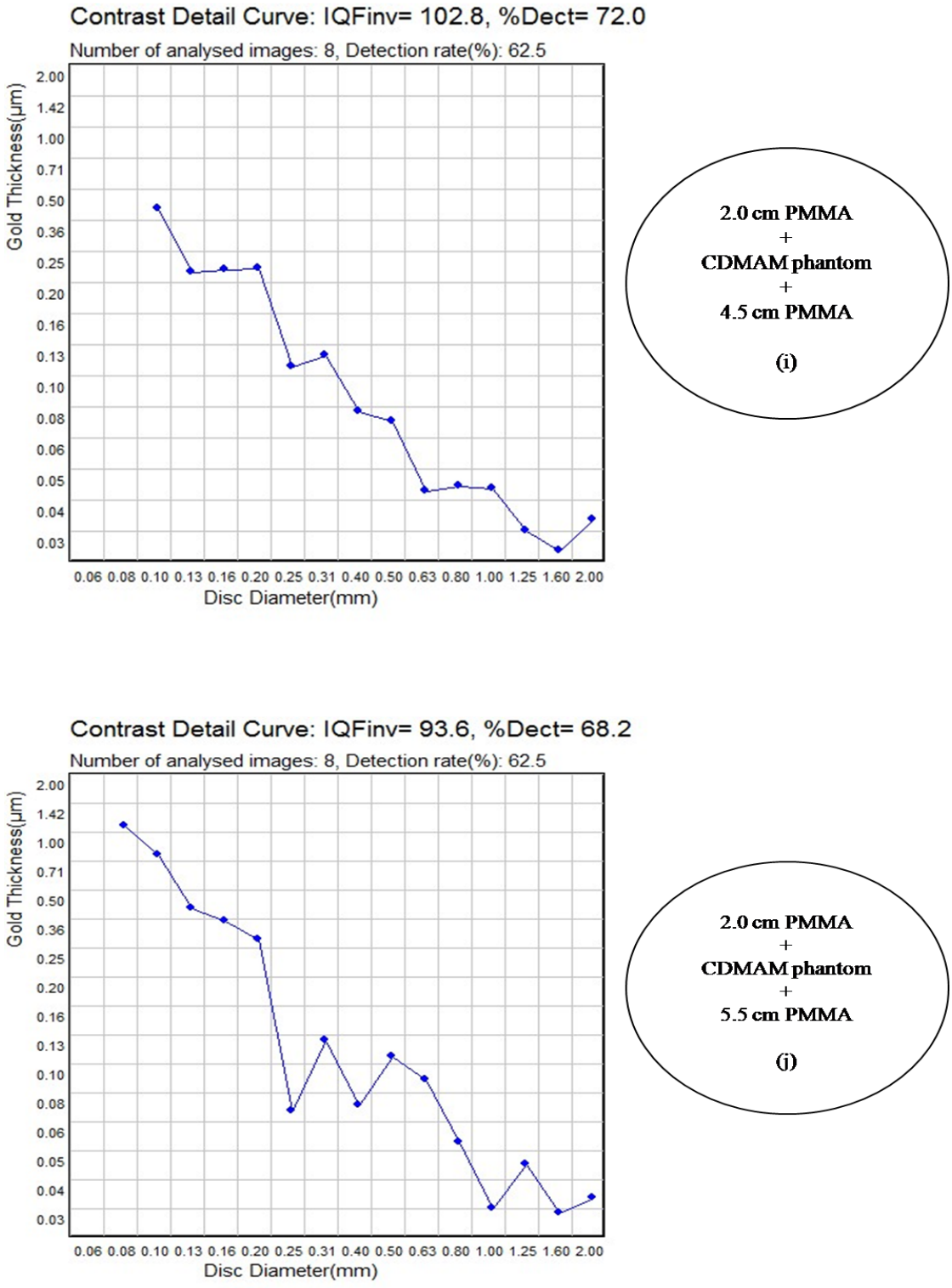

Figure 4.15 Software generated contrast detail curves for the CDMAM phantom exposed in combination with PMMA sheets of various thicknesses to simulate clinical operating conditions under OPDOSE mode (a-j)

Table 4.4 The IQF_{inv} number and % detected gold disks for the CDMAM phantom which was kept on top of the 4.5 cm thick PMMA sheet and exposed at three different target/filter (T/F) combinations using AEC mode

Target filter combination (T/F)	**IQF_{inv}**	**% detected gold disks**	**Operating parameters (kV/mAs) (Average value for eight images)**	**Machine displayed MGD (mGy)**
Mo/Mo	145.7	78.3	28/167.1	3.8
Mo/Rh	144.3	77.4	28/135.2	2.9
W/Rh	127.7	74.5	28/188.9	2.1
T/F, Target/Filter; Mo/Mo, Molybdenum/Molybdenum; Mo/Rh, Molybdenum/Rhodium; W/Rh, Tungsten/Rhodium; MGD, Mean glandular dose; mGy, milli Gray				

Table 4.5 The IQF_{inv} number and % detected gold disks for the CDMAM phantom kept along with PMMA sheets to simulate different clinical breast thicknesses and exposed under clinically used OPDOSE mode

Phantom thickness (cm)	**IQF_{inv}**	**% detected gold disks**	**Operating parameters (kV/mAs) (Average value for eight images)**	**Machine displayed MGD (mGy)**
0.5 cm PMMA + CDMAM	171.9	81.6	24/41.1	0.6
1.5 PMMA + CDMAM	151.7	79	26/49.6	0.8
2.0 PMMA + CDMAM	144.4	78.7	26/63.2	0.9
2.0 PMMA + CDMAM + 0.5 cm PMMA	128.1	77.3	27/71.6	1.0
2.0 PMMA + CDMAM + 1.0 PMMA	168.2	79.1	27/97.45	1.25
2.0 PMMA + CDMAM + 1.5 PMMA	147.4	78.5	28/110.3	1.5
2.0 PMMA + CDMAM + 2.5 PMMA	135.6	75.5	29/152.4	2.0
2.0 PMMA + CDMAM + 3.5 PMMA	105.5	71.5	30/206.45	2.4
2.0 PMMA + CDMAM + 4.5 PMMA	102.8	72.0	31/361.3	3.8
2.0 PMMA + CDMAM + 5.5 PMMA	93.6	68.2	32/342.4	3.75
PMMA, Polymethylmethacrylate; CDMAM, Contrast detail mammography phantom; MGD, Mean glandular dose; mGy, milli Gray				

Figure 4.16 shows the calculated MTF values at different spatial frequencies from the image of exposed slanted edge device using Mo/Mo as T/F combination for the digital mammography system. Figure 4.17 shows the calculated normalized noise power spectrum Vs spatial frequency for the digital mammography system at the entrance air kerma of 100μGy. Both, the MTF and the NPS are found to be falling off at higher spatial frequencies.

However at higher spatial frequencies, lower MTF values are observed when compared with reported values for the studied digital mammography machine.

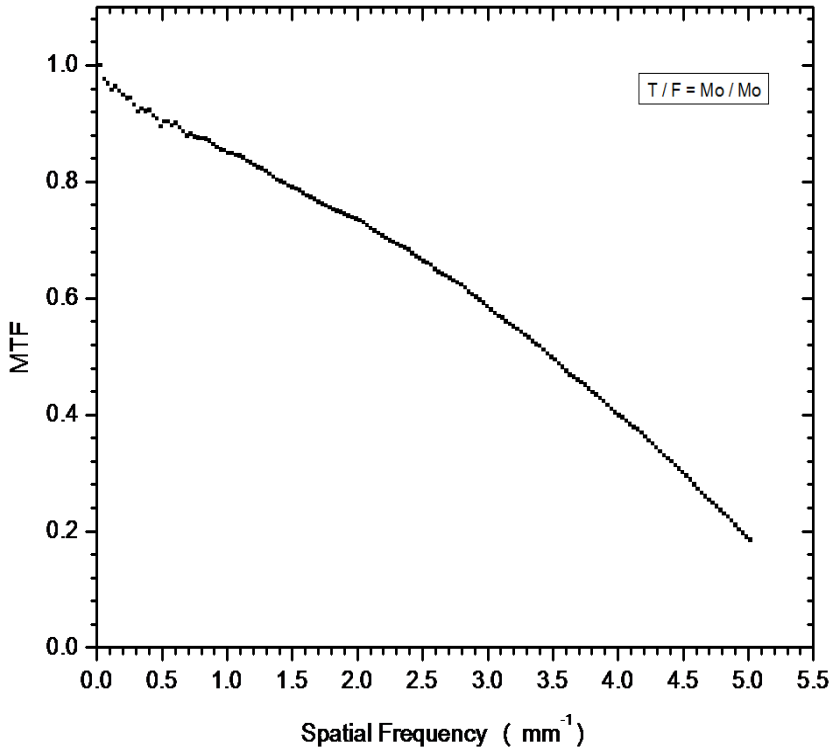

Figure 4.16 Plot of calculated modulation transfer function (MTF) values at different spatial frequencies for the digital mammography system

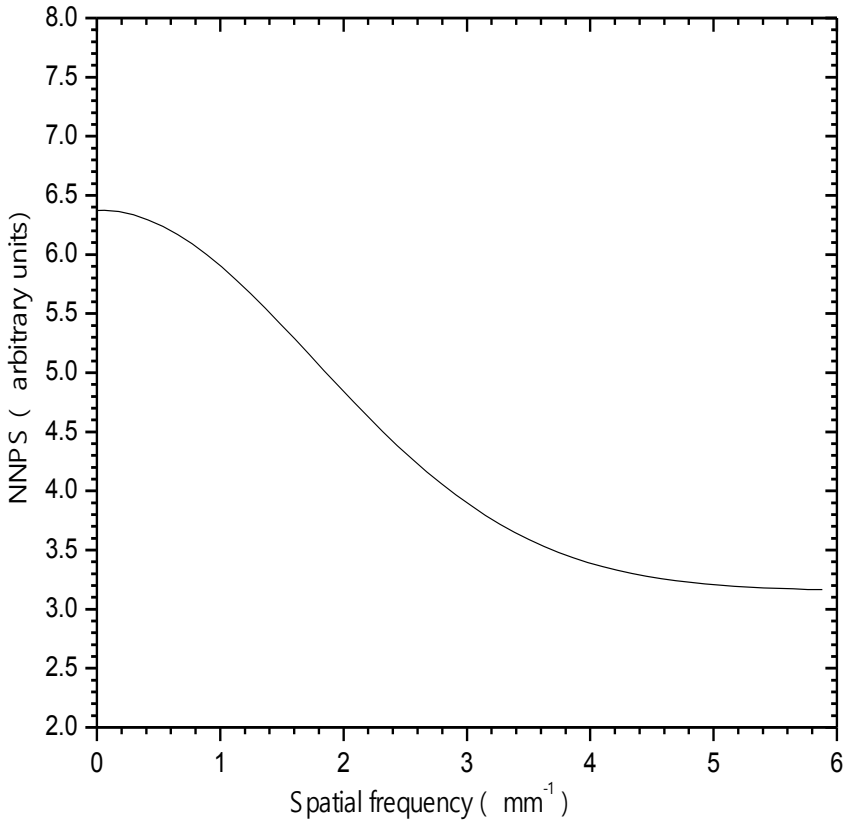

Figure 4.17 Plot of calculated normalized noise power spectrum (NPS) for the different spatial frequency at entrance air kerma value of ~100 μ Gy

4.4 Conclusions

In present study, various imaging metrics such as CNR, contrast detail resolution, MTF and NPS were evaluated for a direct flat panel detector based digital mammography system following the European Guidelines. As the studied digital mammography system have different exposure mode, a system performance study relating to both image quality and doses was carried out by evaluating figure of merit (FOM) in terms of CNR^2/MGD under automatic exposure control (AEC) and clinically used OPDOSE operating mode. Under AEC mode of operation and for a given phantom thickness the highest CNR and MGD values were observed for Mo/Mo, T/F combination whereas W/Rh combination has provided the highest

FOM value. Whereas for clinically used OPDOSE mode highest CNR, lowest MGD and correspondingly highest FOM values were found for 2 cm thick BARC PMMA phantom. From this study, it was also concluded that as the phantom thickness increases, CNR and FOM value decreases. Detailed dosemetric studies were also performed on the digital mammography system by calculating mean glandular doses (MGDs) using several mammography phantoms made-up of breast tissue equivalent materials. However, all the calculated MGDs values were found to be lower than the acceptable level of dose limits provided in European guidelines.

****

Chapter 5

Feasibility studies in mammography using synchrotron radiation

5.1 Introduction

In recent years, use of synchrotron radiation (SR) x-ray source is increasing globally in the medical imaging due to the advent of x-ray phase contrast imaging (XPCI) technology (Fitousi et al 2012, Bradley et al 2007, Munro et al 2010). XPCI has shown the great potential with respect to visibility contrast improvement while examining soft tissues found within the breast (Miao et al 2005). In medical imaging field, XPCI has been employed by three methods which are propagation, interference and analyzer based and present study employs the propagation based method for producing phase contrast. Propagation based XPCI technique relies on the principle of refraction of x-rays at the boundary defined by two different density regions. The refracted and direct wave propagates a finite distance and interferes due to a path difference to produce bright and dark fringes. Outcome of this interaction is manifested in terms of edge enhancement along the boundary of interest. Under XPCI technique, an air gap between the object and the detector is established to transform the phase gradients generated by the interference of x-rays having different phase shifts into intensity gradient on the image (Dreossi et al 2008, Matsuo et al 2005, Weon et al 2006).

Micro-focus and synchrotron based x-ray sources are found to be suitable for phase contrast imaging because of their high spatial coherence whereas conventional x-ray sources are not due to their low spatial coherence (Wong et al 2014, Schleede et al 2012, Nesterets et al 2015). Synchrotron x-ray has several characteristics such as spatially coherent, high intensity, vertical collimation and polarization (Burattini 1997, Longo 2016). It is also reported that when a coherent x-ray beam gets scattered in an object it is distributed not only due to attenuation (photoelectric, absorption, Compton and Rayleigh scatterings) but also due to refraction on the boundaries between media providing better phase contrast visibility at boundaries (Ingal et al 1998).

Several authors have carried out XPCI based mammography work and one such XPCI based mammography study have shown the great improvement in image quality-dose relationship, which was due to monochromaticity and high degree of intrinsic collimation of SR x-ray beam (Moeckli et al 2000). Another XPCI study performed at 17 keV SR x-rays on Ackermann mammographic phantom and biological specimens obtained at postmortem excision were reported and outcome of the study has shown the improved image quality with only slightly increased dose compared with those for SR absorption imaging and also with reduced dose when compared with conventional mammography (Arfelli et al 2000). Another attempt towards XPCI concludes that in the SR x-ray energy range of 15-25 keV, the effects due to phase shift are considerably more relevant than those due to absorption effects for biologic soft tissues (Raven et al 1996).

We have carried out absorption and phase mode imaging studies on various phantoms and samples of clinical relevance1using 12 and 16 keV SR x-ray beam of Indus-2, RRCAT, Indore, India(Indian synchrotron facility). Low keV SR x-ray beams were used in our study because phase contrast signature is upto 1000 times higher than absorption contrast for the soft tissue/objects having small density differences at these energies (Bradley et al 2007, Pelka 2008). SR x-ray images of different phantoms and samples were analyzed and imaging parameters were quantified in terms of edge enhancement index and edge enhancement to noise ratio (Donnelly et al 2006) Dosimetry calculations were also carried out based on the measured SR x-ray flux at different SR x-ray energies and radiation dosimetry formalism (Agrawal et al 2015, Yamazaki et al 2007).

5.2 Materials and methods

5.2.1 Propagation based x-ray phase contrast imaging (XPCI)

XPCI technique is based on the principle of refraction of x-rays at the boundary defined by two different density regions and the complex index of refraction (n) is given the following equations:

$$n=1-\delta-i\beta \quad (5.1)$$

where δ is the index decrement that is responsible for the phase shift and ß is the absorption index. The δ and ß components are expressed as

$$\delta= N_A (Z/A) \rho e^2\lambda^2/(2\pi mc^2) \quad (5.2)$$

$$\beta = \mu\lambda/4\pi \quad (5.3)$$

where N_A is Avogadro's number (=6.02 x 10^{23}), Z is atomic number, A is atomic mass, ρ is density (g/cm^3) of the medium, $e^2/(mc^2)$ is classical radius of electron (=2.82 x10^{-13} cm), λ is the wavelength (cm) of x-ray,μ is a linear attenuation coefficient of the medium. The refractive index decrement δ depends on energy E of the x-ray photons and the density of the object (equation 5.2).Term ß is related to linear attenuation coefficient μ and is the basis for image contrast in attenuation based imaging techniques such as conventional mammography. Figure 5.1 (a and b) is the schematic diagram of experimental set ups of absorption and phase mode imaging techniques used in this work.

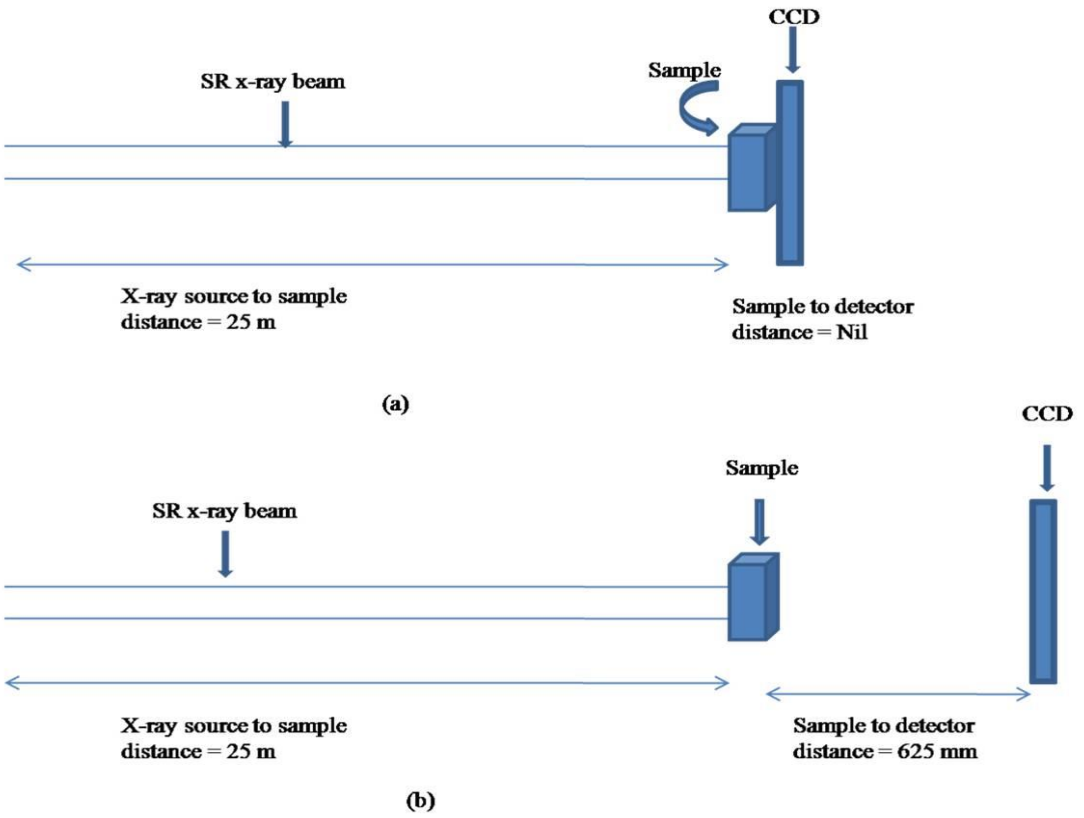

Figure 5.1 Schematic diagram of experimental set up utilized to perform SR x-ray imaging of various phantoms/samples under (a) absorption and (b) phase mode

5.2.2 Synchrotron x-ray source

In this particular study, all the experiments were carried out at imaging beam line, BL-4 of the synchrotron facility Indus-2, having a 2.5 GeV, 300 mA third generation synchrotron radiation source located at Raja Ramanna Centre of Advanced Technology (RRCAT), Indore, India.BL-4 has both monochromatic as well as white beam mode of operation. In monochromatic mode, the energy range covered is 8 to 35 keV while in white beam mode energy upto 50keV is available. The maximum beam dimension in the experimental station is 100 mm x 10 mm and photon flux is ~10^{10} photons/s in monochromatic mode while it is 10^{16} photons/s in white beam mode (Agrawal et al 2015). BL-4 experimental station has all the instruments required to perform various imaging experiments such as phase contrast x-ray imaging as shown in figure 5.2.

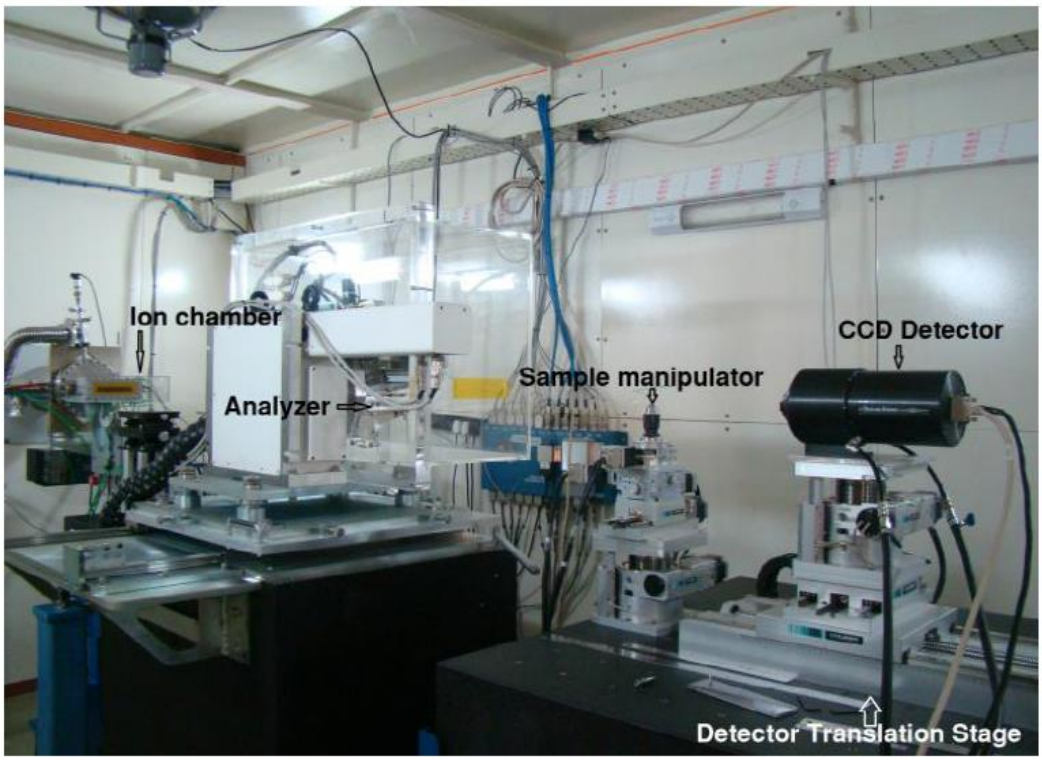

Figure 5.2 Synchrotron x-ray imaging beam line (BL-4) facility at Indus-2, RRCAT, Indore, India

5.2.3 Imaging camera system and sample manipulator

In the present study, we have used VHR-1 imaging camera system (Photonic Science, Mountfield, UK) which contains 1:2 fibreoptic plate coated with gadolinium oxide scintillator and high resolution CCD (pixels 4007 x 2678, pixel size 4.5 μm and field of view 18 mm x 12 mm). The performance of the camera is found to be linear in the energy range 8 to 50 keV and measured resolution for the fibreoptic coupled CCD camera is 5 μm with 8 % contrast (Agrawal et al 2015). BL-4 has high precision six axis sample manipulator stages consisting of X, Y, Z, θ, ψ, φ and high precision three axis manipulator for X, Y, Z motions of the detectors. BL-4 also has an ionization chamber for measuring the online beam current and dose monitoring with fast shutter for controlled exposure time in bio-medical imaging. Complete experimental station on vibration isolated granite tables is shown in figure 5.2. Images were acquired using a fibre optic coupled CCD camera at 12 and 16 keV SR beam for

620 ms exposure time. In the entire phase mode imaging, source to sample distance was 25 meter and phantom to detector distance was 625 mm which was experimentally optimized condition to achieve the proper phase signature of the various phantoms/sample images as shown in figure 5.1.

5.2.4 Image analysis parameters

In XPCI technique, two parameters are defined to quantify the edge effect seen in the image of the object. First parameter is edge enhancement index (EEI) which quantifies the edge enhancement effect of a phase mode image (Donnelly et al 2006). EEI measures the relationship of the edge enhancement effect relative to the absolute change in intensity form absorption differences across the edge (Donnelly et al 2006). The EEI is defined as

$$\mathrm{EEI} = \frac{(\mathrm{P}-\mathrm{T})/(\mathrm{P}+\mathrm{T})}{(\mathrm{H}-\mathrm{L})/(\mathrm{H}+\mathrm{L})} \qquad (5.4)$$

where P and T are the peak and trough intensity values at the edge as shown in figure 5.3(a). Intensity values H and L are the result of no edge enhancement at the high and low intensity regions next to the edge (Figure 5.3).

Second parameter is edge enhancement to noise ratio (EE/N) which measures the edge enhancement relation with image noise and is given by the following equation

$$EE/N = \frac{(P-T)}{\sqrt{\sigma_H^2 + \sigma_L^2}} \qquad (5.5)$$

where σ_H and σ_L are the standard deviation of the pixels used to calculate H and L in the EEI.

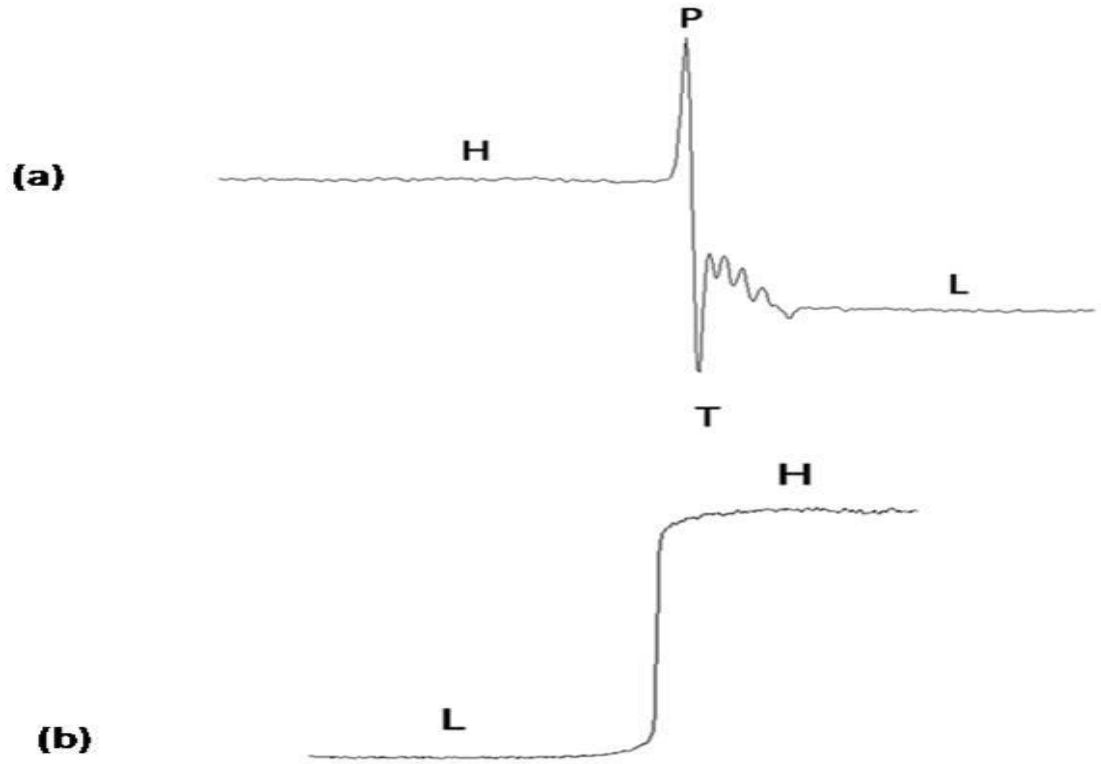

Figure 5.3 Description of various points for calculating EEI and EE/N (a) Used to calculate EEI and EE/N when there is an edge enhancement in the object image (under phase mode imaging) (b) used when there is no edge enhancement seen in the image of an object (absorption mode).In the case of absorption mode image of an object, $P \approx T$ and $H \approx L$

5.2.5 Imaging phantoms

Imaging phantoms are the basis for characterizing any image system. Table 5.1 contains the details of the phantom/samples of breast tissue equivalent material and purpose of their selection.

Table 5.1 Various phantoms and samples used for synchrotron x-ray image analysis

Sr. No.	Phantom/Samples	Purpose for selection
1	CIRS mammography imaging phantom (model 015)	For imaging, various test objects which simulate various breast diseases
2	Aluminium based microcalcification phantom (locally fabricated)	To simulate microcalcifications found in breast cancer patients
3	PMMA and Polystyrene step wedges(locally fabricated)	To simulate thickness variation change within the same tissue types
4	Gel phantom (locally made)	To simulate fibrocystic breast tissues

Following sections provides the construction details and material contents of these phantoms and samples:

5.2.5.1 CIRS mammography imaging phantom

A standard CIRS imaging phantom (model 015) having dimensions of 10.8 cm x 10.2 cm x 4.4 cm was included in this study which is generally used to perform quality control check on the conventional mammography system (CIRS, Virginia, USA). This model of the CIRS phantom consists of a removable wax sheet of 5 mm thickness and embedded inserts that mimic the anatomic breast structures/artificial features such as fibers, specks to simulate microcalcifications, and masses. The wax sheet contains six numbers of nylon fibers of different thicknesses ranging from 0.40 to 1.56 mm, five set of microcalcifications with sizes of 0.16 to 0.54 mm and five glandular masses of 0.25 to 2.00 mm thicknesses as shown in figure 5.4.

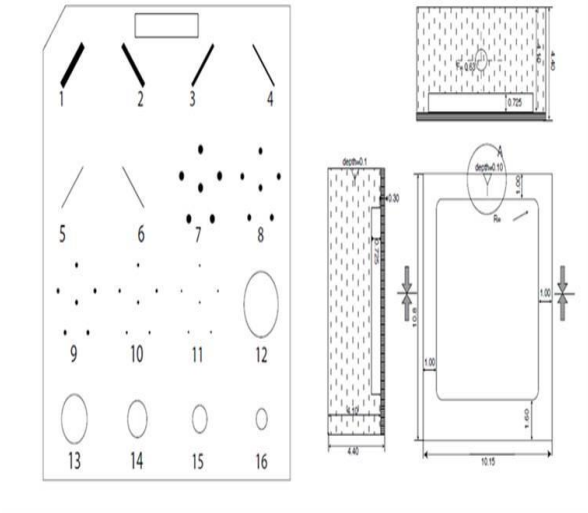

SPECIFICATIONS

WAX INSERT					
FIBERS (Nylon Fiber)		**SPECKS** (Al_2O_3 speck)		**MASSES** (Thickness)	
1.	1.56 mm	7.	0.54 mm	12.	2.00 mm mass
2.	1.12 mm	8.	0.40 mm	13.	1.00 mm mass
3.	0.89 mm	9.	0.32 mm	14.	0.75 mm mass
4.	0.75 mm	10.	0.24 mm	15.	0.50 mm mass
5.	0.54 mm	11.	0.16 mm	16.	0.25 mm mass
6.	0.40 mm	-		-	

Figure 5.4 Wax sheet of mammography imaging phantom with various test objects and their specifications (CIRS model 015)

5.2.5.2 Aluminum based microcalcification phantom

Microcalcifications (MCs)finding in the breast are considered as indirect signs of pathological process and detecting these on mammograms are difficult due to its small size (<1 mm) (Henrot et al 2014, Suryanarayanan et al 2007). In conventional mammography aluminium (Al) is often used as a material for simulation of calcification (Vedantham and Karellas 2013, Warren et al 2013). In view of this, we have designed and locally fabricated a microcalcification phantom using Al in the form of circular discs with diameter of 5 mm and thickness ranging from 50 to 500 microns as shown in figure 5.5. These Al discs were sandwiched between two PMMA sheets each having 1 mm thickness. SR x-ray images of every Al disc was acquired under absorption and phase mode at 12 and 16 keV.

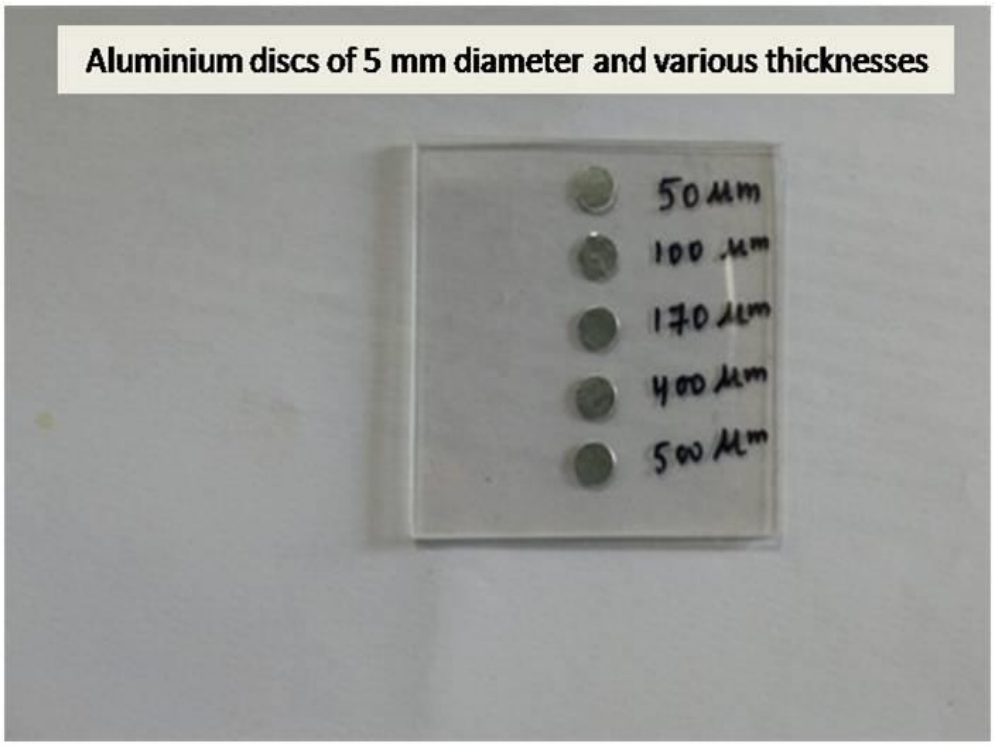

Figure 5.5 Aluminium discs sample to represent microcalcification

5.2.5.3 PMMA and polystyrene step wedges

To simulate thickness variation within the same tissue types, step wedge samples were fabricated. Although different synthetic materials can be used as breast tissue substitute for making mammography phantoms, we have used PMMA (1.19 g/cm^3) and Polystyrene (1.06 g/cm^3) (NIST 2010) as shown in figure 5.6 (Berger et al 2010). Step thickness for these two locally fabricated step wedges ranges from 1.0 to 5.0 mm. Also at various edges of the steps, a line profile was plotted to compare the EEI and EE/N values under absorption and phase mode. SR x-ray images of these step wedges were analyzed and reported using Image J software (Image J) (Rasband 2012).

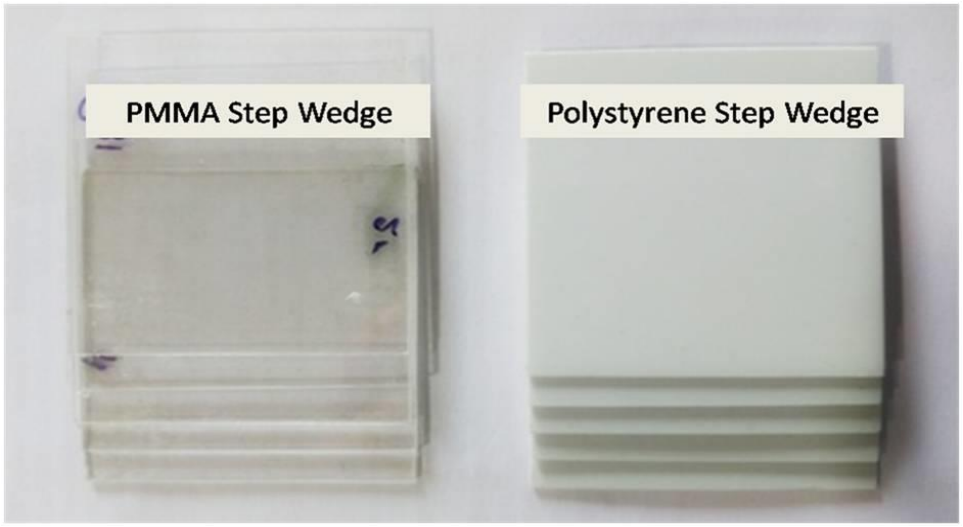

Figure 5.6 PMMA and polystyrene step wedge phantom

5.2.5.4 Polymer gel phantom

In case of conventional mammography examination, viewing a fibrocystic breast tissue is difficult due to insignificant difference between linear attenuation coefficients of fibrous and tumor tissues in the energy range of 15 to 26.5 keV (Chen et al 2010). Polymer gel (1.026 gm/cm^3) exhibits the closet radiological water equivalence and in view of this we have used a dried polymer gel phantom as shown in figure 5.7 to study the artificial fibers structure detectability in SR x-ray beam (Brown et al 2008). This phantom was exposed at 12 keV SR x-ray beam in both absorption and phase mode and results were compared in terms of visual appearance and line plot profile for a small cross sectional image.

Figure 5.7 Top and side view of polymer gel phantom

5.3 Estimation of absorbed dose to air at object plane

Absorbed dose to air (which is equivalent to air kerma at such a low energy) for the monoenergetic x-ray photon beam with energy E is given by the following relation (Mittone et al 2013).

$$D_{air} = \phi\, E\, (\mu_{en}/\rho) \qquad (5.6)$$

where ϕ is the incident x-ray photon fluence and μ_{en}/ρ is the mass energy-absorption coefficient. It may be noted that in the energy domain of keV x-rays, the linear energy absorption (μ_{en}) and energy transfer coefficients (μ_{tr}) are considered to be equal (Mittone et al 2013, Attix 2015). In this study, Si-PIN photodiode based measured values of SR x-ray photon flux and the standard mass energy absorption coefficients were used for estimating the absorbed dose to air (Agrawal et al 2015, Berger et al 2010). Ideally glandular dose is estimated and mean glandular dose is reported for comparing different clinical mammography systems from patient dose point of view. However, in this case, it was not possible to measure and report the mean glandular dose and hence dose to air at imaging plane was measured and reported.

5.4 Results and discussion

5.4.1 Image analysis of CIRS wax sheet

Due to small SR x-ray beam size, we have taken the image of each test objects embedded inside the CIRS wax sheet phantom one by one. Finally, these images were analyzed and stitched together to bring out in the form of a single image. Figure 5.8 shows the images of 16 test objects of CIRS mammography imaging phantom. These images represent the visual image quality of different test objects embedded inside CIRS-wax sheet taken by SR x-ray at 12 and 16 keV energy. Visual analysis of these images was carried out by five different image analysis experts and overall findings of all are reported here. Visual

analysis of the SR x-ray image of CIRS wax sheet provides better edge contrast for the fibers, masses and microcalcifications in the phase mode in comparison to the absorption mode.

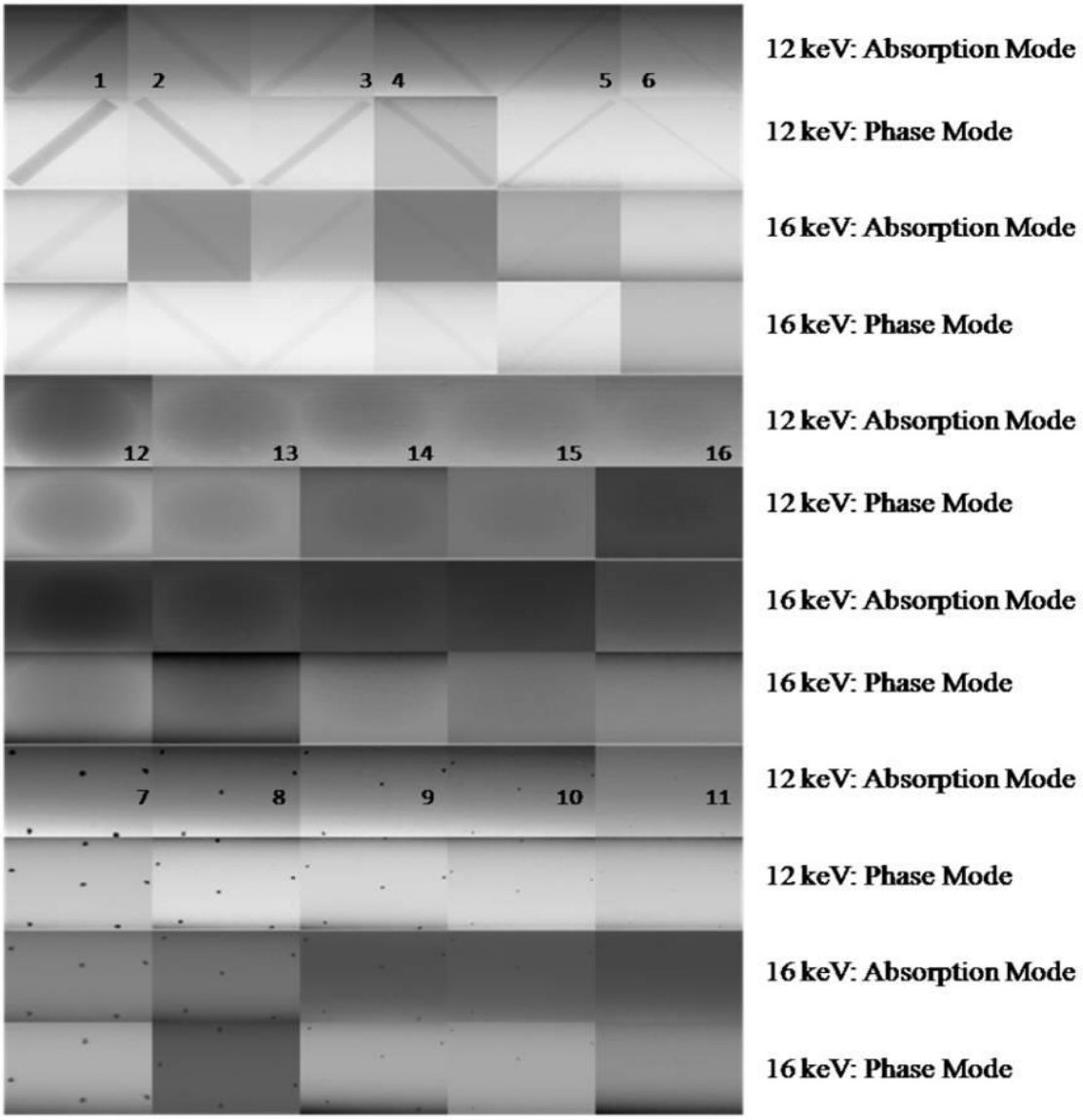

Figure 5.8 Synchrotron x-ray image of various test objects embedded in CIRS mammography imaging phantom at 12 and 16 keV SR x-ray energies

In addition, irregular geometries are also seen in the enlarged view of microcalcifications represented by test object numbers 7 to 11 (Figure 5.9) which is generally not possible with the conventional mammography system. Edge enhancement effect was quantified using EEI and EE/N for the larger test objects (e.g. Fiber1, Mass 12 and MC7) only. For this purpose, line profile from the images of these test objects were plotted as

shown in figure 5.10. Using these profiles, EEI and EE/N were calculated and average values have been shown in table 5.2. It is observed that EEI and EE/N values are relatively higher for the phase mode images than the absorption mode images for these test objects.

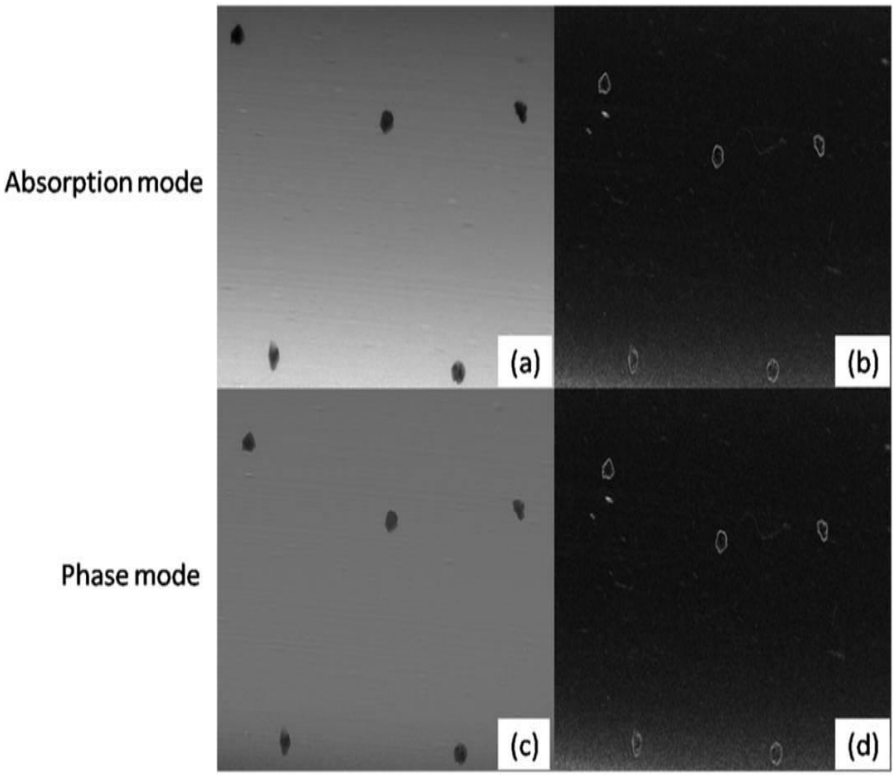

Figure 5.9 Images of microcalcifications represented by test object number 7 of CIRS wax sheet: (a) enlarged view in absorption mode, (b) enlarged view after edge detection processing in absorption mode, (c) enlarged view in phase mode (d) enlarged view after edge detection processing in phase mode

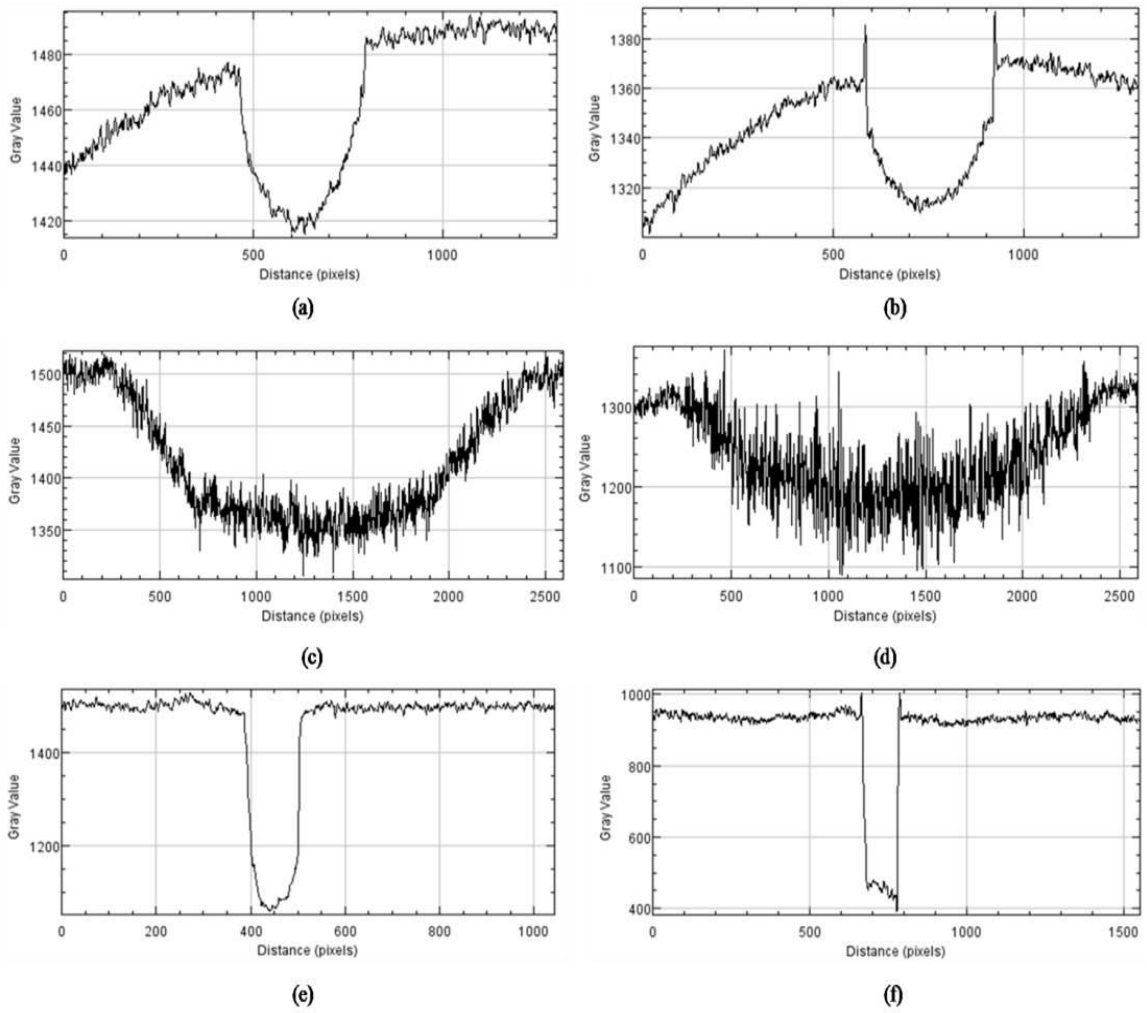

Figure 5.10 Line profile from the images of larger test objects (Fiber 1, Mass 12 and MC 7) of CIRS wax sheet: (a) Fiber 1 from absorption mode (b) Fiber 1 from phase mode (c)Mass 12 from absorption mode (d) Mass 12 from phase mode (e) Microcalcification 7 from absorption mode (f) Microcalcification 7 from phase mode

Table 5.2 Mean measured EEI and EE/N values for largertest objects (Fiber1, Mass 12 and MC7) of CIRS wax sheet

	EEI	**EE/N**	**EEI**	**EE/N**
	Fiber1 @ 12keV		**Fiber1 @ 16keV**	
Absorption mode	0.75±0.16	3.55±0.12	0.79±0.13	1.91±0.30
Phase mode	0.86±0.14	3.85±0.09	1.35±0.06	4.81±0.15
	Mass 12 @ 12keV		**Mass 12 @ 16keV**	
Absorption mode	0.86±0.11	5.2±0.11	0.88±0.09	5.83±0.12
Phase mode	1.11±0.08	7.5±0.30	1.17±0.08	8.2±0.16
	Microcalcification 7 @ 12keV		**Microcalcification 7 @ 16keV**	
Absorption mode	0.97±0.08	12.69±0.18	0.93±0.09	5.83±0.20
Phase mode	1.096±0.05	15.89±0.10	1.17±0.06	8.2±0.16

5.4.2 Image analysis of Al based microcalcification phantom

Line profiles were plotted for all the discs of Al based microcalcification phantom for quantification of image quality in terms of EEI and EE/N. Figure 5.11 shows the line profile of one of the aluminium discs plotted from its absorption and phase mode images.EEI and EE/N values were derived for all the five Al discs. Figure 5.12 shows the variations of EEI and EE/N with respect to thickness of Al discs of microcalcification phantom. The plot includes data from the absorption and phase mode images taken at 12 and 16 keV of SR x-ray energies. It is observed from plots in figure 5.12 that EEI and EE/N values are higher for phase mode than absorption mode at both of these SR x-ray energies.

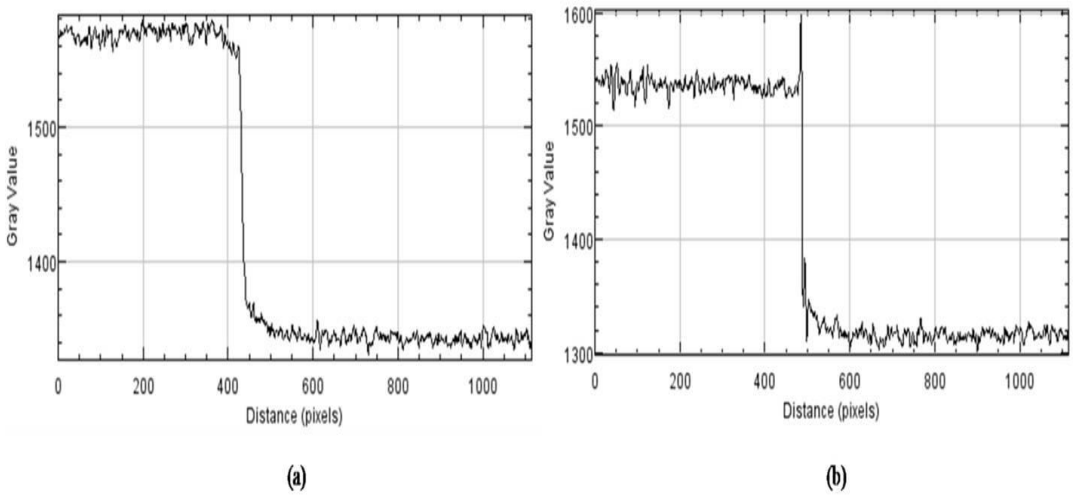

Figure 5.11 Plot of line profile for SR x-ray image of 'Al' disc sample at 16 keV under (a) absorption and (b) phase mode

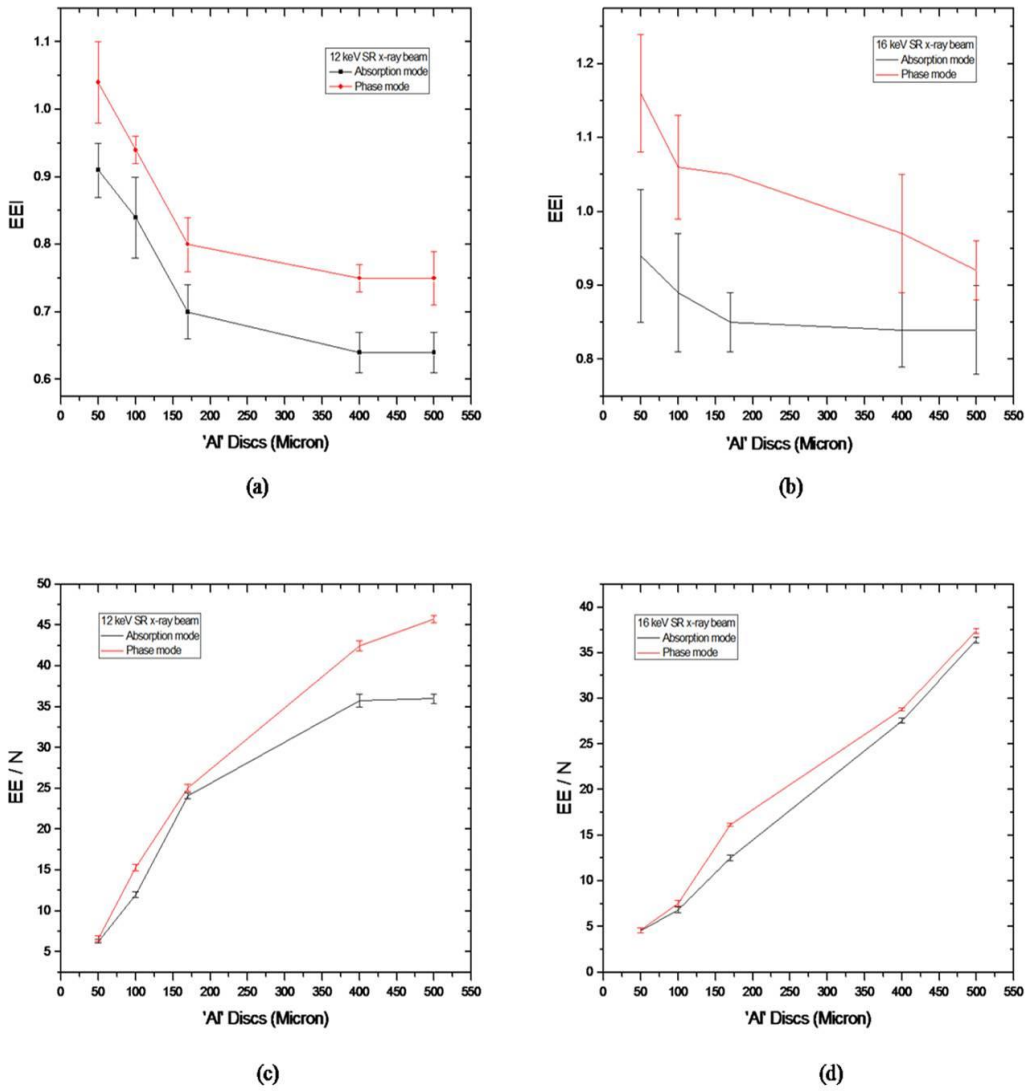

Figure 5.12 Variations of EEI and EE/N with thickness of aluminium discs derived from absorption and phase mode: (a) EEI at 12 keV, (b) EEI at 16 keV, (c) EE/N at 12keV, and (d) EE/N at 16keV

5.4.3 Image analysis of PMMA and polystyrene step wedges

Figures 5.13 and 5.14 present SR x-ray images and the line profiles for PMMA and polystyrene step wedges in absorption and phase modes at 12 and 16 keV energies, respectively. Combined line profiles of absorption and phase modes for visualization of edge enhancement have also been shown in these figures. The mean values of EEI and EE/N derived from the lines profiles are given in table 5.3 for PMMA and polystyrene step wedges.

The plots and the data show that edge contrast enhancement is relatively higher in phase mode.

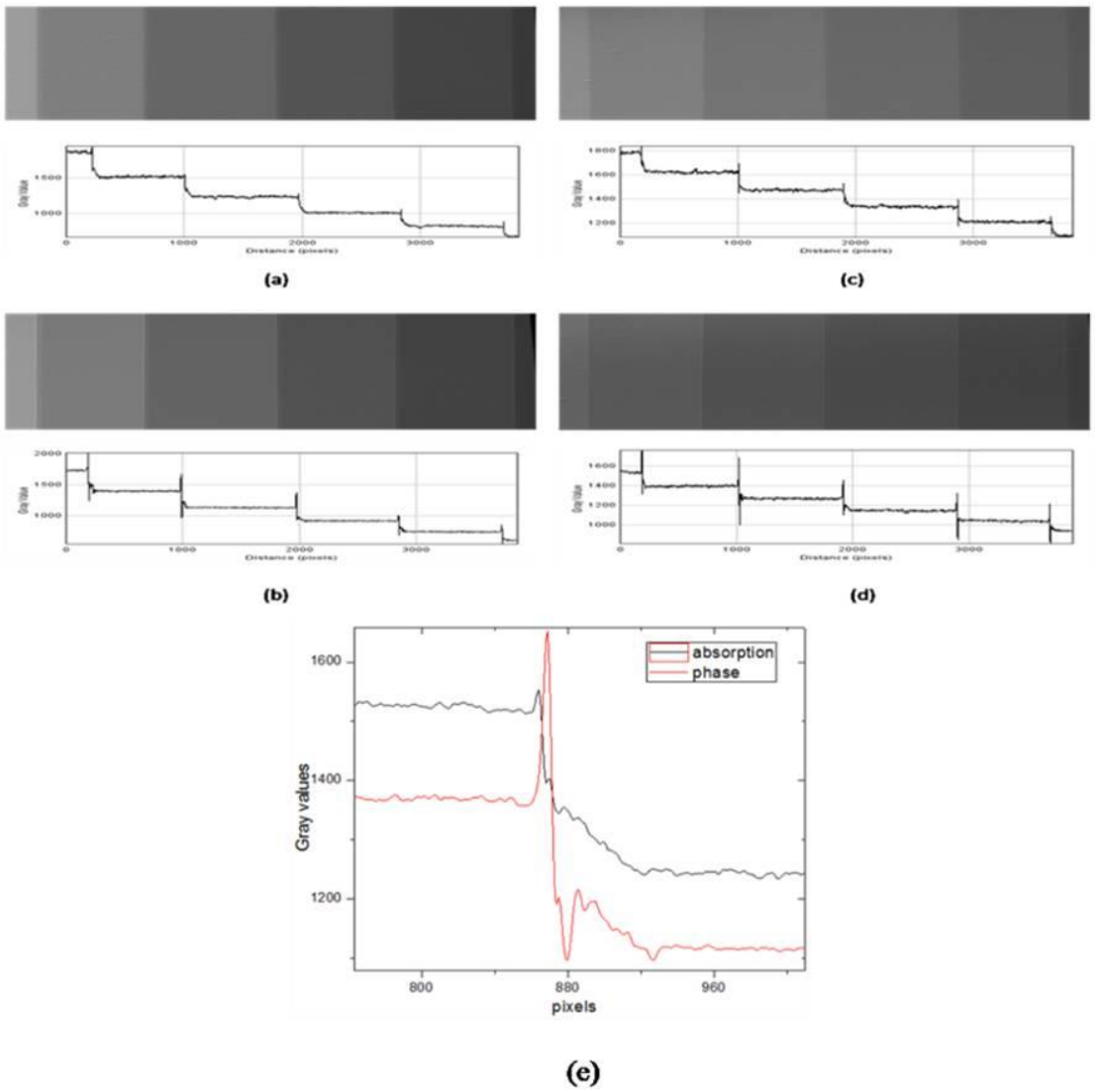

Figure 5.13 SR x-ray images and line profiles for PMMA step wedge in absorption and phase modes: (a) 12keV-absorption mode (b) 12 keV-phase mode (c) 16 keV-absorption mode (d) 16 keV-phase mode, and (e) combined line profiles in absorption and phase mode at 12 keV for visualization of edge enhancement

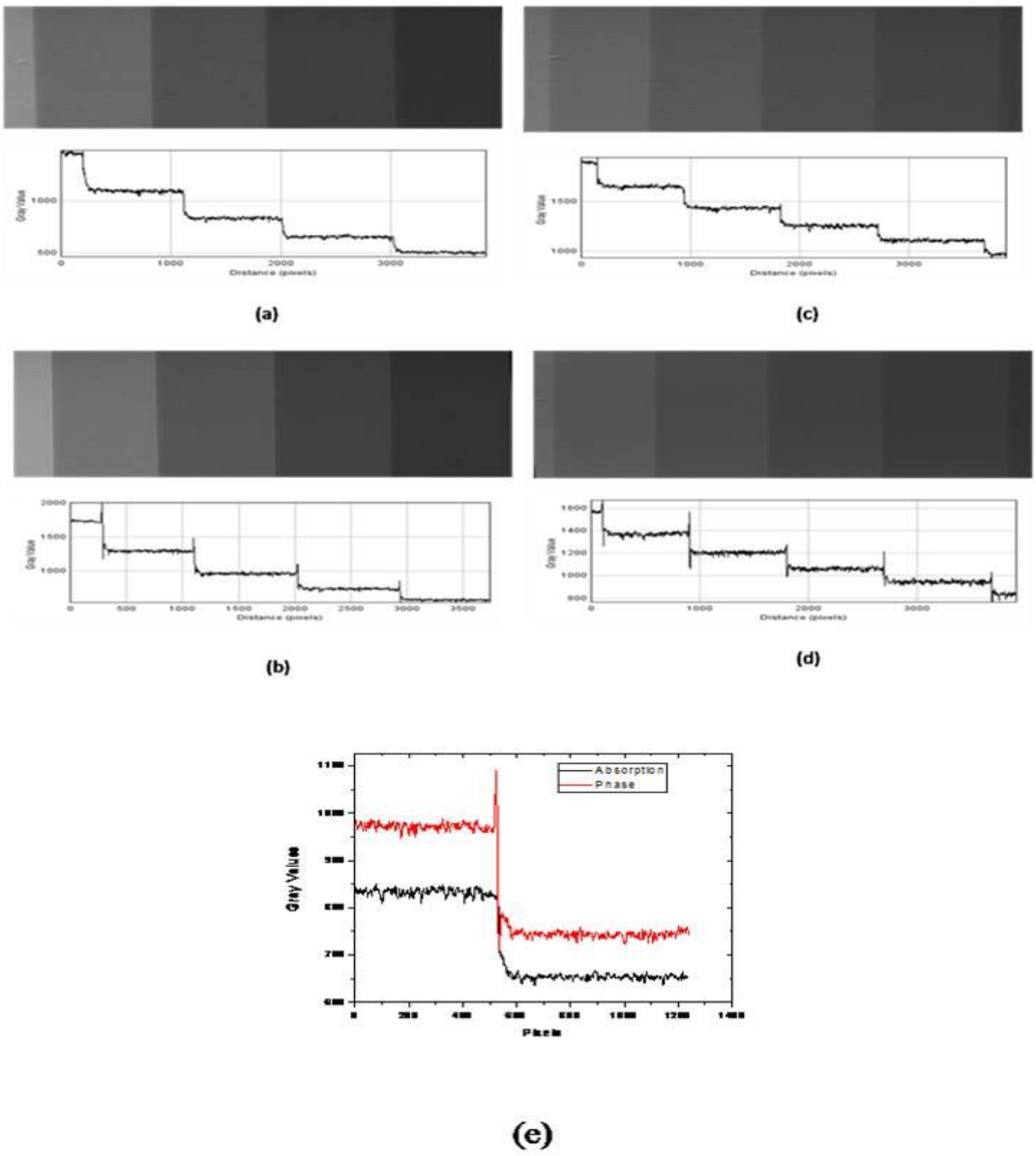

Figure 5.14 SR x-ray images and line profiles for polystyrene step wedge in absorption and phase modes: (a) 12keV-absorption mode (b) 12 keV-phase mode (c) 16 keV-absorption mode (d) 16 keV-phase mode, and (e) combined line profiles in absorption and phase mode at 12 keV for visualization of edge enhancement

Table 5.3 Measured EEI and EE/N values for step wedge samples at 12 and 16 keV SR x-ray beam

Step wedge	**12 keV-EEI**		**12 keV-EE/N**	
	Absorption mode	**Phase mode**	**Absorption mode**	**Phase mode**
PMMA	0.92±0.17	1.64±0.25	11.04±2.03	25±1.83
Polystyrene	0.72±0.06	1.53±0.31	4.54±0.65	10.06±3.26
	16 keV-EEI		**16 keV-EE/N**	
PMMA	1.19±0.36	3.7±1.11	7.73±1.39	21.61±2.47
Polystyrene	0.90±0.10	2.49±0.23	4.8±1.43	11.31±3.04

5.4.4 Image analysis of polymer gel phantom

Figure 5.15 shows absorption and phase mode images of polymer gel phantom and line profiles of a small region of interest from the images. EEI and EE/N were derived from these line profiles and the mean values are shown in table 5.4. Both visual inspection and the quantitative values of EEI and EE/N indicate better image quality (e.g. visualization of fibers) of polymer gel phantom in phase mode.

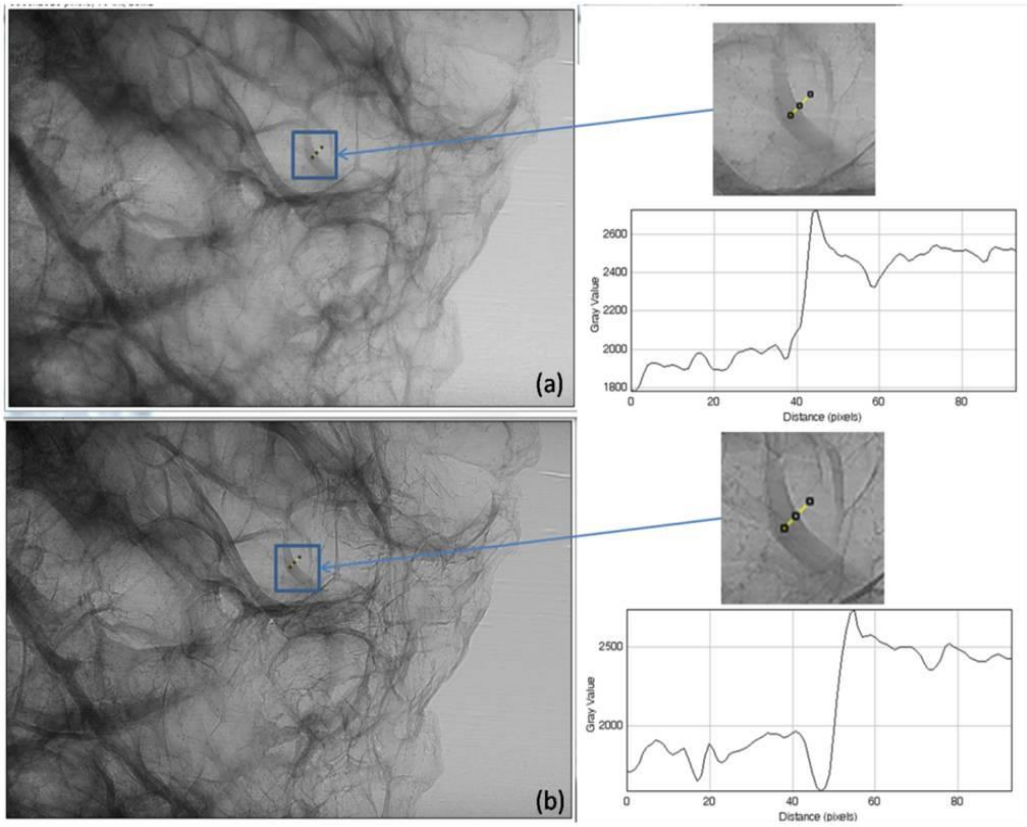

Figure 5.15 Cross sectional image of gel phantom and plot of line profile at 12 keV under (a) absorption and (b) phase mode image

Table 5.4 Mean measured EEI and EE/N values for a small region of the polymer gel phantom

EEI at 12 keV		**EE/N at 12 keV**	
Absorption mode	**Phase mode**	**Absorption mode**	**Phase mode**
1.19±0.21	1.86±0.36	28.21±0.3	35.31±0.67

5.4.5 Absorbed dose to air from SR x-ray beam

The measured photon flux at 12 and 16 keV of SR x-ray energies are 1.74×10^8 and 1.21×10^8photons/s/mm^2. Values of mass energy absorption coefficients for these two SR x-ray energies are 3.48 and 1.44 cm^2/g. Accordingly, absorbed dose to air for the SR x-ray

beam of 12 and 16 keV energies were found to be 75.59 mGy and 28.9 mGy respectively. The value of absorbed dose to air for 16 keV is less than that of 12 keV SR x-ray beam due to low SR x-ray flux and mass energy absorption coefficient value of 16 keV. It can be seen the obtained dose values are very high when compared with conventional mammography system due to high x-ray flux and dose rate at the sample plane when SR is used. However these dose values can be optimized by reducing the image acquisition time without compromising the image quality when clinical samples are imaged.

5.5 Conclusions

As in-phantom measurements are the best solution for characterizing any imaging system, we have used various phantoms and samples made up of breast tissue equivalent materials for carrying out mammography imaging studies at beam line, BL-4, Indus-2 SR x-ray source of RRCAT, Indore, India.SR x-ray images of different phantoms and samples were analyzed and imaging parameters were quantified in terms of edge enhancement index (EEI) and edge enhancement to noise ratio (EE/N). Dosimetry calculations were also carried out based on the measured SR x-ray flux at different SR x-ray energies. Outcome of these studies conclude that improved sensitivity can be achieved by applying low keV SR x-ray based XPCI imaging for examining soft tissue equivalent materials. In conclusion, this work demonstrates the feasibility of x-ray phase contrast imaging in mammography using 12 and 16 keV SR x-ray beams.

****

Chapter 6

Summary and future work

Mammography is popularly being used for diagnosis and screening of breast cancer. However, the use of this technique also has radiation risk associated with it. And the women who are at higher risk of developing breast cancer may get adversely affected if the radiation dose delivered during mammography procedure is not optimized. As the female breast contains glandular tissues which have higher radiation sensitivity; therefore optimization of this particular imaging technique is strictly necessary. Additionally if image quality is not appropriate, there are high chances of missing the breast cancer which may contribute to delay in treatment and such practices are not acceptable. Hence as a part of dissertation work, image quality and dosimetry of conventional and advanced imaging systems were carried out. The major findings and conclusions from the thesis work are summarized as given below:

(i) Screen film mammography uses single emulsion medical x-ray film to overcome the cross over effect unlike the radiography film which is having double emulsion coating on it. In India, at most of the mammography centers, single processor is used for processing of both mammography and radiography films and this particular practice effects the sensitometric characteristic of mammography film as the required temperature and time for processing of these two films are going to be different. Also there are several studies which have reported the adverse effect of processing time and temperature on image quality in mammograms. Hence a sensitometric study was performed on a Kodak MinR-2000 mammography film which is widely used in our country to evaluate parameters like base plus fog level (B+F), maximum optical density (OD_{max}), average gradient (AG) and speed of the film at varying development temperature and time. Recommendations were provided for optimum processing conditions to be used for the studied mammography film on the basis of our work. Similar studies for various types of mammography films will be helpful in deciding the onset processing conditions to be used by the automatic film processors.

(ii) Development of a mammography imaging and dosimetry phantom was carried out using soft tissue equivalent material polymethyl methacrylate (PMMA) as import substitute. The PMMA phantom is made up of PMMA slabs of different length and radii. The length and radius of the central slab is of 21 cm and 10 cm respectively and every slab on either side of the central slab continue to decrease in length and radius at an interval of 5 mm respectively. The total thickness of phantom is 5 cm comprising total 10 slabs. The developed phantom is found suitable for performing quality assurance (QA)/quality control (QC) of the screen film and digital detector based mammography systems. The radiation transmission property of this phantom was comparable with commercially available similar phantoms and can be used in mammography dosimetry. Also the developed phantom has engraved slots for keeping large number of thermoluminiscence dosimeters (TLD) and is found excellent in measuring the breast entrance exposure (BEE), mean glandular dose (MGD), percentage depth dose (PDD), percentage surface dose distribution (PSDD), calibration testing of automatic exposure control (AEC) and density control function of a mammography machine. Also same phantom without having TLD slots can be used to measure contract to noise ratio (CNR) of the digital mammography system. Also this phantom is found best suitable for measuring the inter dose relationship between image quality and mean glandular dose (MGD) by evaluation the parameter called as figure of merit (FOM).

(iii) Various imaging metrics such as CNR, contrast detail resolution, MTF and NPS were evaluated following the European guidelines for an advanced digital mammography system made up of a-Se detector. Also, system performance relating to both image quality and mean glandular dose were evaluated using figure of merit (FOM) in terms of CNR^2/MGD under automatic exposure control (AEC) and clinically used OPDOSE operating mode. Under AEC mode, FOM values for the 4.5 cm thick BARC

PMMA phantom were found to be highest for the W/Rh target/filter (T/F) whereas under OPDOSE mode, FOM values were found to highest for the 65.32, 11.80 and 1.14 for the thickness of 2.0 cm thick BARC PMMA phantom. Under OPDOSE mode, the highest MGD value was found for the CIRS slab phantom having total thickness of 7.0 cm with glandular/adipose tissue composition of 70/30 than the other two combinations of 50/50 and 30/70. Whereas for 2 to 8 cm thick BARC PMMA phantom, calculated MGDs were found to be in the range of 0.57 to 3.32 mGy. The variation of MGD with BARC PMMA phantom thickness was represented by the second order polynomial fit equation and same will be useful for deriving the MGD values directly from the fitted curve for the large number of thickness. However in our study all the calculated MGDs values were found to be lower than the acceptable level of dose limits provided in European guidelines. As in India such kind of systematic studies on the advanced mammography systems are not performed, this study will be helpful to those professional who are associated with this field.

(iv) Although conventional mammography systems, which are based on absorption imaging, can produce good contrast for the samples having high subject contrast. But the same is not true when the absorption imaging is used for the samples having low subject contrast which is the case of soft tissues found within the breast. Hence, the concept of phase based imaging was brought forth in the thesis work. Under this dissertation work, several mammography phantom and soft tissue equivalent samples were used for demonstrating the feasibility of using synchrotron radiation in mammography imaging. The use of synchrotron radiation in medical imaging has shown great potential for improving soft tissue image contrast especially in case of breast. Advanced imaging technique using SR have been explored by carrying out x-ray phase contrast imaging studies in mammography at Indian synchrotron facility Indus-2. Under this study quantitative

evaluation of XPCI technique for the various breast tissue equivalent test materials and mammography phantoms are reported. Different phantoms and samples including locally fabricated samples were used to perform absorption and phase mode imaging at 12 and 16 keV SR beams. Edge enhancement index (EEI) and edge enhancement to noise ratio (EE/N) were measured for all the phantom and sample images. Absorbed dose values to air were calculated for 12 and 16 keV SR beams using the measured SR flux at the object plane and by applying the standard radiation dosimetry formalism. For the first time in India, XPCI studies were carried out in mammography using low energy synchrotron beams of 12 and 16 keV. Outcome of the study suggests good contrast improvement under phase mode than the absorption mode for the various test objects and phantoms giving future scope for imaging the breast tissue specimens.

6.1 Future scope

The thesis describes the development of a mammography phantom as import substitute which can be used for QC and QA check of mammography systems including mammography dosimetry. This phantom will also be helpful in performing the national postal audit of image quality and mean glandular dose received by patients in the various mammography systems at regional level as the developed phantom is of light weight and not very expensive like imported one. Also collected data on MGD at national level can be used for establishing the national reference level or guidance level in mammography. Mammography film studies for its sensitometric evaluation at different development temperature and time can be used to optimize the processing conditions for the mammograms taken on different vendors' mammography films. Digital mammography although has several technical advantages over SFM, but potential for increasing the patient doses cannot be resolved unless a systematic inter image quality and dose relationship is established for the different phantom thicknesses as encountered clinically with the patients. Hence image

quality and dosimetry studies on a-Se based flat panel digital mammography system can be used to set up a bench mark for performing such studies on different digital mammography systems. The XPCI experiment conducted at the Indian synchrotron facility have shown the better visibility for the soft tissue objects when compared with the absorption imaging. In India, medical physicist and medical research communities are not aware applying the use of synchrotron in imaging, whereas globally great opportunities using XPCI method have been shown by several synchrotron researchers. From the work of these researchers it can be concluded that future possibilities of the XPCI method in medical field should not be underestimated. Furthermore clinical use of XPCI demands other factors to be determined such as most appropriate imaging devices, optimized energy levels, dose and other parameters affecting image quality.

****

References

AAPM 1990 Equipment requirements and quality control for mammography AAPM *On-Line Report No 29* (College Park, MD: American Association of Physicists in Medicine Task Group 18)

Agrawal A K, Singh B, Kashyap Y S, Shukla M, Sarkar P S and Sinha A 2015 Design development and first experiments on the x-ray imaging beamline at Indus-2, synchrotron source RRCAT, India *J. Synchrotron Rad.* **22** 1531-39

Alan R, Simon L and Alice L 2016 Imaging techniques in breast cancer. *Surgery (Oxford)* **34** 8-18

Ali I, Wani W A and Saleem K 2011 Cancer scenario in India with future perspectives *Cancer Therapy* **8** 56–70

American College of Radiology (ACR) *Mammography quality control manual-Mammography* (Reston, VA: American College of Radiology)

Andrew K and Srinivasan V 2012 Detectors for digital mammography *(Digital Mammography: A Practical Approach)* (New York: Cambridge University Press)

Arfelli F et al 1998 Low-dose phase contrast x-ray medical imaging *Phys. Med. Biol.* **43** 2845–52

Arfelli F, Bonvicini V, Bravin A, Cantatore G, Castelli E, Palma L D, Michiel M D, Fabrizioli M, Longo R, Menk R H, Olivo A, Pani S, Pontoni D, Poropat P, Prest M, Rashevsky A, Ratti M, Rigon L, Tromba G, Vacchi A, Vallazza E and Zanconati F 2000 Mammography with synchrotron radiation phase-detection techniques *Radiology* **215** 286-293

Attix F H 2004 *Introduction to Radiological Physics and Radiation Dosimetry* (Germany: Wiley)

Babu G R, Lakshmi S B and Thiyagarajan J A 2013 Epidemiological correlates of breast cancer in South India *Asian Pac. J. Cancer Prev.* **14** 5077–83

Balasubramaniam S, Rotti S and Vivekanandam S 2013 Risk factors of female breast carcinoma: a case control study at Puducherry *Indian J. Cancer* **50** 65–70.

Baldelli P, Phelan N and Egan G 2009 A novel method for contrast-to noise ratio (CNR) evaluation of digital mammography detectors *Eur. Radiol*. **1** 2275-85

Berg WA. Nuclear Breast Imaging: Clinical Results and Future Directions 2016 *J. Nucl. Med.* **57** 46S–52S

Berger M J, Hubbell J H, Seltzer S M, Chang J, Coursey J S, Sukumar R, Zucker D S and Olsen K 2010 XCOM: Photon Cross Section Database (version 1.5) *Technical Report* (Gaithersburg, MD: NIST) http://physics.nist.gov/xcom (Accessed: 5 March 2015)

Berns E A, Hendrick R E and Cutter G A 2002 Performance comparison of full-field digital mammography to screen-film mammography in clinical practice *Med. Phys.* **29** 830-83

Bick U, Diekmann F 2010 *Digital Mammography* (Berlin: Springer)

Borasi G, Nitrosi A, Ferrari P and Tassoni D 2003 On site evaluation of three flat panel detectors for digital radiography *Med. Phys*. **30** 1719-31

Borg M, Badr I and Royle G J 2012 The use of figure of merit (FOM) for optimization in digital mammography: A literature review *Radiat. Prot. Dosim*. **151** 81-88

Bradley D, Gundogdu O, Jenneson P, Eleftheria N and Ismail E H C 2007 Review of x-ray phase contrast imaging techniques and propagation based imaging using a benchtop microfocal source *Jurnal Sains Kesihatan Malaysia* **5** 1-16

Brink C, de Villiers J F K, Lotter M G and Vanzyl M 1993 The influence of film processing temperature and time on mammographic image quality *Br. J. Radiol*. **66** 685-690

Brown S, Venning A, Deene Y D, Vial P, Oliver L, Adamovics J and Baldock C 2008 Radiological properties of the PRESAGE and PAGAT polymer dosimeters *Appl. Radiat. Isot.* **66** 1970-74

Burattini E 1997 Synchrotron radiation: New trend in X-ray mammography *Acta. Physica. Polonica A.* **91** 707-713

Burrell H C et al 1996 Screening interval breast cancers: mammographic features and prognosis factors *Radiology* **199** 811–17

Burrell H C et al The positive predictive value of mammographic signs: a review of 425 non-palpable breast lesions *Clin Radiol* **51** 277-81

Bushberg J T, Siebert J A, Leidholdt E M and Boone J M 2002 *The Essential Physics of Medical Imaging* 2nd edn (Philadelphia: Lippincott Williams and Wilkins)

Chen R C, Longo R, Rigon L, Zanconati F, Pellegrin A De, Arfelli F, Dreossi D, Menk R-H, Vallazza E, Xiao TQ and Castelli E 2010 Measurement of the linear attenuation coefficients of breast tissues by synchrotron radiation computed tomography *Phys. Med. Biol*. **55** 4993-5005

Cho Z H, Tsai C M and Wilson G 1975 Study of contrast and modulation mechanisms in X-ray/photon transverse axial transmission tomography *Phys Med Biol.* **20** 879

Chukhovskii F N and Guigay J P 1993 Towards a rigorous treatment of the wave-field propagation according to the statistical theory of dynamical diffraction *J. Phys. D. Appl. Phys.* **26** A53–A56

Cirolla V 2017 *Breast Anatomy* https://www.researchgate.net /publication/321011257_Breast_anatomy (Accessed: 20 June 2018)

CIRS Tissue Simulation & Phantom Technology: *The CIRS Model 011A Breast phantom* http://www.cirsinc.com/011a_mammo.html (Accessed: 10 January 2016)

CIRS Tissue Simulation & Phantom Technology: *The CIRS Model 015 Mammography accreditation phantom* http://www.cirsinc.com/file/Products/015 (Accessed: 10 January 2016)

Collins L 2015 Radiography special issue- Issues in breast imaging *Radiography* **21** 297

Craig A R, Heggie J C P, McLean I D, Coakley K S and Nicoll J J 2001 Recommendations for a mammography quality assurance programme ACPSEM position paper *Australas. Phys. Eng. Sci. Med.* **24** 107-130

Dance D R 1990 Monte Carlo calculation of conversion factors for the estimation of mean glandular breast dose *Phys. Med. Biol.* **35** 1211-19

Dance D R and Sechopoulos I 2016 Dosimetry in x-ray-based breast imaging *Phys. Med. Biol.* **61** R271–R304

Dance D R, Skinner C L and Carlsson G A 1999 Breast dosimetry *Appl. Radiat. Isot*. **50** 185-203

Dance D R, Skinner C L, Young K C, Beckett J R and Kotre C J 2000 Additional factors for the estimation of mean glandular breast dose using the UK mammography dosimetry protocol *Phys. Med. Biol.* **45** 3225–3240

De Martini W, Lehman C and Partridge S 2008 MRI for cancer detection and characterization: A review of evidence-based clinical applications *Acad. Radiol*. **15** 408-16

Di Leo G, Trimboli R M, Sella T and Sardanelli F 2017 Optical imaging of the breast: Basic principles and clinical applications *Am. J. Roentgenol*. **209** 230–238

Dinshaw K A, Shastri S S and Patil S S 2005 Cancer control programme in India: Challenges for the new millennium *Health Administrator* **17** 10-13

Donnelly E F, Lewis K G, Wolske K M, Pickens D R and Price R R 2006 Characterization of the phase-contrast radiography edge-enhancement effect in a cabinet x-ray system *Phys. Med. Biol.* **51** 21-30

Dreossi D, Abrami A, Arfelli F, Bregant P, Casarin K, Chenda V, Cova MA, Longo R, Menk R H, Quai E, Quaia E, Rigon L, Rokvik T, Sanabor D, Tonutti M, Tromba E-Cabrera J and Brandan M-E 2015 Performance evaluation of a digital mammography unit using a contrast-detail phantom *Journal of Physics* Conference Series **582** 012036

Dreossi D, Abrami A, Arfelli F, Bregant P, Casarin K, Chenda V, Cova MA, Longo R, Menk R H, Quai E, Quaia E, Rigon L, Rokvik T, Sanabor D, Tonutti M, Tromba G, Vascotto A, Zanconati F and Castelli E The mammography project at the SYRMEP beamline *Eur. J. Radiol.* **68S** S58-S62

European Commission 1996 *European protocol on dosimetry in mammography EUR 16263* (Luxembourg: European Commission)

European Commission 2001 *The European protocol for the quality control of the physical and technical aspects of mammography screening* 3rd edn (Luxembourg: European Commission)

European Commission 2006 *European guidelines for quality assurance in breast cancer screening and diagnosis* 4th edn (Luxembourg: European Commission)

Falcone P M, Baiano A, Zanini F, Mancini L, Tromba G, Dreossi D, Montanari F, Scuor N and Nobile M A D 2005 Three-dimensional quantitative analysis of bread crumb by x-ray microtomography *Journal of Food Science* **70** E265–E272

Faulkner K, Law J and Cranley K 1995 Technical note: Perspex blocks for estimation of dose to a standard breast-effect of variation in block thickness *Br.J.Radiol*. **68** 194-196

Fausto A M F, Lopes M C, Sousa M C de, Furquim T A C, Mol A W and Velasco F G 2017 Optimization of image quality and dose in digital mammography *J. Digit. Imaging* **30** 185-196

Feig S A and Yaffe M J 1998 Digital mammography *RadioGraphics* **18** 893–901

Ferlay J et al 2015 Cancer incidence and mortality worldwide: sources, methods and major patterns in GLOBOCAN 2012 *Int. J. Cancer***136** E359–86

Ferlay J, Shin H R, Bray F, Forman D, Mathers C and Parkin D M 2010 Estimates of worldwide burden of cancer in 2008: GLOBOCAN 2008 *Int. J. Cancer* **127** 2893–17

Ferreira T and Rasband W S 2010-2012 ImageJ *User Guide-IJ 1.46* www.imagej.nih.gov/ij/docs/guide (Accessed: 5 April 2015)

Figl M, Semturs F, Kaar M, Hoffmann R, F-Westerdijk M, van der Burght R, Homolka P and Hummel J 2015 On the dose sensitivity of a new CDMAM phantom *Phys. Med. Biol*. **60** N177-N185

Fitousi N T, Delis H and Panayiotakis G 2012 Monte Carlo simulation of breast imaging using synchrotron radiation *Med. Phys.* **39** 2069

Gotzsche P C and Olsen O 2000 Is screening for breast cancer with mammography justifiable? *Lancet* **355** 129–134

Green M and Raina V 2008 Epidemiology, screening and diagnosis of breast cancer in the Asia–pacific region: Current perspectives and important considerations *Asia–PacificJournal of Clinical Oncology* **4** S5–S13

Grosenick D, Rinneberg H, Cubeddu R and Taroni P 2016 Review of optical breast imaging and spectroscopy *J Biomed Opt* **21** 091311

Guigay J P, Langer M, Boistel R and Cloetens P 2007 Mixed transfer function and transport of intensity approach for phase retrieval in the Fresnel region *Opt. Lett.* **32** 1617

Gureyev T E and Nugent K A 1996 Phase retrieval with the transport-of-intensity equation II. Orthogonal series solution for nonuniform illumination *J. Opt. Soc. Am. A* **13**1670-82

Gureyev T E, Nesterets Y I, Stevenson A W, Miller P R, Pogany A and Wilkins S W 2008 Some simple rules for contrast, signal-to-noise and resolution in in-line x-ray phase-contrast imaging *Opt. Express* **16** 3223–41

Hartley L D, Cobb B J and Hutchinson DE 1999 Estimating mean glandular dose using proprietary mammography phantoms *Appl. Radiat. Isot.* **50** 205-213

Hendrick R E and Ikeda D M 2018 https://clinicalgate.com/mammography (Accessed: 5 August 2018)

Henrot P, Leroux A, Barlier C and Genin P 2014 Breast microcalcifications: The lesions in anatomical pathology *Diagn. Interv. Imaging* **95** 141-152

Hooley R J, Durand M A and Philpotts L E 2017Advances in digital breast tomosynthesis *AJR* **208** 256–266

Huda W, Sajewicz A M, Ogden K M and Dance D R 2003 Experimental investigation of the dose and image quality characteristics of a digital mammography imaging system *Med. Phys.* **30** 442-8

Ingal V N, Beliaevskaya E A, Brianskaya A P and Merkurieva R D 1998 Phase mammography-a new technique for breast investigation *Phys. Med. Biol.* **43** 2555-67

International Atomic Energy Agency (IAEA) 2005 Optimization of the radiological protection of patients: image quality and dose in mammography *TECDOC-1447* IAEA, Vienna

International Atomic Energy Agency (IAEA) 2009 Quality assurance programme for screen film mammography (*Human Health Series*) *number 2* (Vienna: IAEA)

Jackson D F and Hawkes D J 1981 X-ray attenuation coefficients of elements and mixtures *Physics Reports* **70** 169–233

Jacobson D R 1998 Mammography radiation dose and image quality *Radiat. Prot. Dosim*. **80** 295-97

Johns Hopkins University 2018 *Breast* https:// pathology.jhu.edu (Accessed: 11 June 2018)

Kasap S O 2000 X-ray sensitivity of photoconductors: application to stabilize a-Se J. *Phys. D: Appl. Phys.* **33** 2853–65

Kelkar S, Boushey CJ and Okos M A 2015 Method to determine the density of foods using x-ray imaging *J. Food Eng.* **159** 36–41

Kennedy D A, Lee T and Seely D 2009 A comparative review of thermography as a breast cancer screening technique *Integr. Cancer Ther*. **8** 9-16

Khalkhali I, Mena I and Diggles L 1994 Review of imaging techniques for the diagnosis of breast cancer: a new role of prone scintimammography using technetium-99m sestamibi *Eur J Nucl Med.* **21** 357-62.

Kimme-Smith C, Rothschild P A, Bassett L W, Gold R H and Moler C 1989 Mammographic film-processor temperature, development time, and chemistry: effect on dose, contrast and noise *Am. J. Roentgenol*. **302** 35-40

Kimme-Smith C, Sun H, Bassett LW and Gold R H 1992. Effect of poor control of film processors on mammographic image quality *Radiographics* **12** 1137-1146

Konstantinidis A C Cdmam_Fit_3: A Graphical user interface for mammographic contrast – detail analysis *e-Journal of Science and Technology* (e-JST) (available at http://e-jst.teiath.gr)

Lahiri B B, Bagavathiappan S, Jayakumar T and Philip J 2012 Medical applications of infrared thermography: A review *Infrared Physics & Technology* **55** 221-235

Lanca L and Silva A 2009 Digital radiography detectors—a technical overview: Part 1. *Radiography* **15** 58–62

Lanca L and Silva A 2009 Digital radiography detectors—a technical overview: Part 2 *Radiography* **15** 134–138

Langer M, Cloetens P, Guigay J P, Valton S and Peyrin F 2007 Quantitative evaluation of phase retrieval algorithms in propagation based phase tomography *IEEE International Symposium on Biomedical Imaging (ISBI)* (Arlington, USA) pp 552-555

Laya M B, Larson E B, Taplin S H and White E 1996 Effect of estrogen replacement therapy on the specificity and sensitivity of screening mammography *J. Natl. Cancer Inst.* **88** 643–49

Liberman M, Sampalis F, Mulder D S and Sampalis J S 2003 Breast cancer diagnosis by scintimammography: a meta-analysis and review of the literature. *Breast Cancer Res. Treat* **80** 115–126.

Longo R 2016 Current studies and future perspectives of synchrotron radiation imaging trials in human patients *Nucl. Instrum. Methods Phys. Res. A* **809** 13-22

Mahadevappa M 2004 Digital Mammography: An Overview *Radiographics* **24** 1747–60

Marco A G R, Sofia G V M, Luis A M H and Roque A O R 2017 Supportive noninvasive tool for the diagnosis of breast cancer using a thermographic camera as sensor *Sensors* **17** 497

Markus K, Christof H W, Stefan W, Klaus-Jurgen P, Maximilian F R and Marcus T 2007 Advances in digital radiography: Physical principles and system overview *RadioGraphics* **27** 675–86

Marshall N W 2007 Early experience in the use of quantitative image quality measurements for the quality assurance of full field digital mammography x-ray systems *Phys. Med. Biol.* **52** 5545-68

Masakazu T, Yasuo O, Adeline S, Takuya M, Gary T, Hironobu S, Byeong W P, Louis WC, Adriano V L, Cheng H Y, Ei U, Hiroshi I and Hiroko B 2010 The breast cancer working group presentation was divided into three sections: the epidemiology, pathology and treatment of breast cancer *Jpn. J. Clin. Oncol.* **40** i13-i18

Matsuo S, Katafuchi T, Tohyama K, Morishita J, Yamada K and Fujita H 2005 Evaluation of edge effect due to phase contrast imaging for mammography *Med. Phys.* **32** 2690-97

Miao H, Gomella A A, Harmon K J, Bennett E E, Chedid N, Znati S, Panna A, Foster B A, Bhandarkar P and Wen H 2015 Enhancing tabletop x-ray phase contrast imaging with nanofabrication *Sci. Rep*. **5** 13581

Mittone A, Baldacci F, Bravin A, Brun E, Delaire F, Ferrero C, Gasilov S, Freud N, Letang J M, Sarrut D, Smekens F and Coan P 2013 An efficient numerical tool for dose deposition prediction applied to synchrotron medical imaging and radiation therapy *J. Synchrotron Rad.* **20** 785-792

Moeckli R, Verdun R F, Fiedler S, Pachoud M, Schnyder P and Valley F J 2000 Objective comparison of image quality and dose between conventional and synchrotron radiation mammography *Phys. Med. Biol.* **45** 3509-23

Munro P R T, Konstantin I, Robert D S and Alessandro O 2010 Design of a novel phase contrast x-ray imaging system for mammography *Phys. Med. Biol.* **55** 4169-85

Murray J G, Dowsett D J, Laird O and Ennis J T 1992 Assessment of mammographic film processor performance in a hospital and mobile screening unit *Br. J. Radiol.* **66** 1097-01

Nassivera E, and Nardin L 1996 Daily quality control programme in mammography *Br. J. Radiol.* **69** 148-152

National Breast Cancer Foundation 2018 *Braest anatomy and how cancer starts* https://nbcf.org.au (Accessed: 20 June 2018)

National Cancer Registry Programme 2016 Three-Year Report of Population Based Cancer Registries: 2012-2014. *Report of 27 PBCRs in India* (Indian Council of Medical Research, Bengaluru)

National Institute of Health 2018 *Types of breast cancers* https://training.seer.cancer.gov/breast (Accessed: 15 August 2018)

NCRP (National Council on Radiation Protection and Measurements) 2004 A guide to mammography and other breast imaging procedures *NCRP Report 149*, NCRP Bethesda, MD

NCS 6 1993 Netherlands commission on radiation dosimetry task group mammography *Dosemetric aspects of mammography* (The Netherlands)

Nesterets Y I, Gureyev T E, Mayo S C, Stevenson A W, Thompson D, Brown J M C, Kitchen M J, Pavlov K M, Lockie D, Brun F and Tromba G 2015 A feasibility study of x-ray phase contrast mammographic tomography at the imaging and medical beamline of the Australian Synchrotron *J. Synchrotron Rad.* **22** 1509-23

Nesterets Y I, Wilkins S W, Gureyev T E, Pogany A and Stevenson A W 2005 On the optimization of experimental parameters for x-ray in-line phase-contrast imaging *Rev. Sci. Instrum.* **76** 1–16

Ng E Y and Kee E C 2008 Advanced integrated technique in breast cancer thermography *J. Med. Eng. Technol.* **32** 103-14

Olivo A 2005 Towards the exploitation of phase effects in clinical synchrotron radiation radiology *Nucl. Instruments Methods Phys. Res. Sect. A Accel. Spectrometers, Detect. Assoc. Equip* **548** 194–199

Olivo A and Speller R 2006 Experimental validation of a simple model capable of predicting the phase contrast imaging capabilities of any x-ray imaging system *Phys. Med. Biol.* **51** 3015–30

Padgett R and Kotre C J 2005 Development and application of programs to measure modulation transfer function, noise power spectrum and detective quantum efficiency *Radiat. Prot. Dosim.* **117** 283-287

Paganin D M 2006 *Coherent X-Ray Optics* (New York: Oxford University press Inc.) Parkin D M, Bray F, Ferlay J and Pisani P 2005 Global cancer statistics,2002 *CA Cancer J. Clin.* **55** 74–108.

Pelka J B 2008 Synchrotron radiation in biology and medicine *Acta. Phys. Pol. A.* 114 Perry N, Broeders M, de Wolf C, Tornberg S, Holland R and von Karsa L 2006 *European guidelines for quality assurance in breast cancer screening and diagnosis* 4th edn (Luxembourg: European Commission)

Peppard H R, Nicholson B E, Rochman C M, Merchant J K, Mayo R C and Harvey J A 2015 Digital breast tomosynthesis in the diagnostic setting: indications and clinical applications *RadioGraphics* **35** 975–990

Phillips D H and Lannutti J J 1997 Measuring physical density with X-ray computed tomography *NDT & E International* **30** 339–350.

Pisano E D 2000 Current status of full-field digital mammography *Radiology* **214** 26–28

Pisano E D et al 2000 Current status of full-field digital mammography 2000 *Acad. Radiol*. **7** 266–280

Pogany A, Gao D and Wilkins S W 1997 Contrast and resolution in imaging with a microfocus x-ray source *Rev. Sci. Instrum*. **68** 2774–82

Porter P 2008 "Westernizing" women's risks? Breast cancer in lower-income countries N. *Engl. J. Med.* **358** 213–16

Porter P L 2009 Global trends in breast cancer incidence and mortality *Salud Pu´blica de Mexico* 51 s141–s46

Ramnath T, Deenu N and Nandakumar A 2010 Projections of number of cancer Cases in India (2010-2020) by cancer groups *Asian Pac. J. Cancer Prev.* **11** 1045-1049

Ranger N T, Samei E, Dobbins J T 3rd, and Ravin C E 2005 Measurement of the detective quantum efficiency in digital detectors consistent with the IEC 62220-1 standard: Practical considerations regarding the choice of filter material *Med. Phys*. **32** 2305-11

Rasband W S 2012 *ImageJ* www. imagej.nih.gov/ij (Accessed: 15 March 2016)

Raven C, Snigirev A, Snigireva I, Spanne P, Souvorov A and Kohn V 1996 *Appl. Phy. Let.* **69** 1826-28

Rivetti S, Lanconelli N, Campanini R, Bertolini M, Borasi G, Nitrosi A, Danielli C, Angelini L and Maggi S 2006 Comparison of different commercial FFDM units by means of physical characterization and contrast-detail-analysis *Med. Phys*. **33** 4198-4209

Rojas L J, Fausto A M F, Mol A W, Velasco F G, Abreu P O S, Henriques G and Furquim T A C 2017 Optimization of the exposure parameters in digital mammography using contrast-detail metrics *Phys. Med.* **42** 13-18

Rothenberg L N and Haus A G 1995 Physicists in mammography–a historical perspective *Med. Phys.* **22** 1923-34

Säbel M and Aichinger H 1996 Recent developments in breast imaging *Phys. Med. Biol.* **41** 315-68

Salvagnini E, Bosmans H, Struelens L and Marshall N W 2013 Effective detective quantum efficiency for two mammography systems: Measurement and comparison against established metrics *Med. Phys.* **40** 101916-16

Samei E and Flynn M J 2003 An experimental comparison of detector performance for direct and indirect digital radiography systems *Med. Phys.* **30** 608-22

Samei E, Dobbins J T, Lo J Y and Tornai M P 2005 A framework for optimizing the radiographic technique in digital X-ray imaging *Radiat. Prot. Dosim.* **114** 220–229

Samei E, Flynn M J 2002 An experimental comparison of detector performance for computed radiography systems *Med. Phys.* **29** 447–459

Sartorius O 1986 *Physical examination* (Maryland: Aspen Publishers Inc.) pp 3-13

Saunders Jr R S, Samei E and Hoeschen C 2004 Impact of resolution and noise characteristics of digital radiographic detectors on the detectability of lung nodules *Med. Phys.* **31** 1603-13

Schleede S, Bech M, Achterhold K, Potdevin G, Gifford M, Loewen R, Limborg C, Ruth, R and Pfeiffer F 2012 Multimodal hard x-ray imaging of a mammography phantom at a compact synchrotron light source *J. Synchrotron Rad*. **19** 525-529

Shahid H, Wiedenhoefer J F, Dornbluth C, Otto P and Kist K A 2016 *An overview of breast MRI* www.appliedradiology.com (Accessed: 15 August 2018)

Sharma R and Sharma S D 2012 A quality control programme for medical x-ray films in India *Radiat. Prot. Dosim*. **148** 51-57

Sharma R, Sharma S D, Mayya Y S and Chourasiya G 2012 Mammography dosimetry using an in-house developed PMMA phantom *Radiat. Prot. Dosim*. **51** 379-385

Shreshtha M, Sarangadhara A B, Uma S D and Sunita S 2017. Epidemiology of breast cancer in Indian women *Asia-Pacific Journal of Clinical Oncology* **13** 289–95

Sickles E A 1991 Periodic mammographic follow-up of probably benign lesions: results in 3,184 consecutive cases *Radiology* **179** 463–68

Sickles E A 2000 Breast imaging: From 1965 to the present Radiology **215** 1e16

Siebert J A 2009 *Digital radiography: The bottom line comparison of CR and DR technology* www.appliedradiology.com (Accessed: 15 August 2018)

Siewerdsen J H, Cunningham I A and Jaffray D A 2002 A framework for noise-power spectrum analysis of multidimensional images *Med. Phys.* **29** 2655-71

Skaane P 2010 Digital Mammography in European population based screening programs *Digital Mammography* ed U Bick U and F Diekmann (Berlin: Springer) pp 155-173

Smith A P, Hall P A and Marcello D M 2004 Emerging technologies in breast cancer detection *Radiol. Manage.* **26** 16-24

Srinath R K, Shah B, Varghese C and Ramadoss A 2005 Responding to the threat of chronic diseases in India *Lancet* **366** 1744–49

Suryanarayanan S, Karellas A, Vedantham S, Sechopoulos I and D'Orsi C J 2007 Detection of simulated microcalcifications in a phantom with digital mammography: Effect of pixel size *Radiology* **244** 130-137

Tabar L 2012 *Imaging of the Breast: Technical Aspects and Clinical Implication* http://www.intechopen.com/bppks/imaging-of-the-breast-technical-aspects and clinical-implication (Accessed: 15 July 2016)

Taibi A, Fabbri S, Baldelli P, di Maggio C, Gennaro G, Marziani1 M, Tuffanelli A and Gambaccini M 2003 Dual-energy imaging in full-field digital mammography: a phantom study *Phys. Med. Biol*. **48** 1945–1956

Taillefer R 1999 The role of 99mTc-sestamibi and other conventional radiopharmaceuticals in breast cancer diagnosis *Semin. Nucl. Med*. **29** 16–40

The Mammography Quality Standards Act (MQSA) 2002 (USA: Food and Drug Administration)

Thilander-Klang A 1997 Diagnostic quality and absorbed doses in mammography: Influence of x-ray spectra and breast anatomy *PhD Thesis* University of Goteborg

Thomas A, Chakrabartim K, Kaczmarek R and Romanyukha A 2005 Contrast-detail phantom scoring methodology *Med. Phys*. **32** 807-814

Tsalafoutas A, Dimakopoulou A D, Koulentianos E D, Serefoglou A N, and Yakoumakis E N 2004 Variation of the sensitometric characteristics of seven mammographic films with processing conditions *Br. J. Radiol.* **77** 666-671

Tung C J, Lin M T, Hsu F Y, Lee J H, Chu C H and Tsai H Y2010 Half value layer determination using thermoluminescent dosimeters for digital mammography *Radiat. Meas.* **45** 729-732

van derBurght R, Thijssen M and Bijkerk R 2010 *Manual Contrast-detail Phantom CDMAM 3.4 & CDMAM Analyzer software* V 1.2 By, Version 7, Artinis Medical Systems BV (The Netherlands)

van Engen R, Young K, Bosmans, H and Thijssen M 2006 *European Guidelines for Quality Assurance in Breast Cancer Screening and Diagnosis* 4 th edn (Luxembourg: European Commission)

Vedantham S and Karellas A 2013 X-ray phase contrast imaging of the breast: Analysis of tissue simulating materials *Med. Phys.* **40** 041906-8

Warren L M, Mackenzie A, Dance D R and Young K C2013 Comparison of the x-ray attenuation properties of breast calcifications, aluminium, hydroxyapatite and calcium oxalate *Phys. Med. Biol.* **58** N103-N113

Weinberg I N 2006 Applications for positron emission mammography *Phys. Med.* **21** 132–137.

Weon B M, Je J H, Hwu Y and Margaritondo G 2006 Phase contrast x-ray imaging Int. *J. Nanotechnology* **3** 280-297

West M S and Spelic D C 2000 Using light sensitometry to evaluate mammography film performance *Med. Phys*. **27** 854-60

Wild J J 1950 *Surgery* **27** 183-188

Williams M B and Fajardo L L 1996 Digital mammography: performance considerations and current detector designs *Acad. Radiol*. **3** 429–437

Williams M B, Krupinski E A, Strauss K J, Breeden W K, Rzeszotarski M S, Applegate K, Wyatt M, Bjork S and Siebert J A 2007 Digital Radiography Image Quality: Image Acquisition *J. Am. Coll. Radiol.* **4** 371-388

Williams M B, Mangiafico P A and Simoni P U 1999 Noise power spectra of images from digital mammography detectors *Med. Phys*. **26** 1279-92

Williams M B, Raghunathan P and More M J 2008 Optimization of exposure parameters in full field digital mammography *Med. Phys.* **35** 2414-23

Wong D M, Wu X and Liu H 2014 Image quality and dose efficiency of high energy phase sensitive x-ray imaging: Phantom studies *J. Xray Sci. Technol* **22** 321-334

Wu X, Barnes G T and Tucker D M 1991 Spectral dependence of glandular tissue dose in screen film mammography *Radiology* **179** 143-148

Yaffe M J 2010 Detectors for digital mammography *Digital Mammography* ed U Bick and F Diekmann (Berlin: Springer) pp 13-31

Yaffe M J and Rowlands J A 1997 X-ray detectors for digital radiography *Phys. Med. Biol.* **42** 1-39

Yaffe M J, Bunch P C, Desponds L, Jong R A, Nishikawa R M, Tapiovaara M J and Young K C 2009 Report 82, *Journal of the International Commission on Radiation Units and Measurements* 9

Yamazaki A, Ichikawa K and Kodera Y 2007 Evaluation of physical image characteristics of phase contrast mammography *Proc. SPIE* **6510** 65103A

Youe R K, Hun S K and Hye-Won K 2015 Are irregular hypoechoic breast masses on ultrasound always malignancies? A pictorial essay *Korean J. Radiol.* **16** 1266–1275.

Young K C, Alsager A and Oduko J M 2008 Evaluation of software for reading images of the CDMAM test objects to assess digital mammography systems. *Proc. SPIE* **6913** 69131C

Young K C, Engen RV, Bosmans H, Jacobs J, Zanga F 2010 Quality control in digital mammography (*Digital Mammography*) eds Bick U and Diekmann F(Berlin: Springer) pp 33-54

Zoetelief J, Dewit N J P and Broerse J J 1989b Technical and dosemetric aspects of quality control in mammography *BIR-Report* **18** 143-146